

IMAGING BY WAVE-EQUATION INVERSION

A DISSERTATION
SUBMITTED TO THE DEPARTMENT OF GEOPHYSICS
AND THE COMMITTEE ON GRADUATE STUDIES
OF STANFORD UNIVERSITY
IN PARTIAL FULFILLMENT OF THE REQUIREMENTS
FOR THE DEGREE OF
DOCTOR OF PHILOSOPHY

Alejandro A. Valenciano

March 2008

© Copyright by Alejandro A. Valenciano 2008
All Rights Reserved

I certify that I have read this dissertation and that, in my opinion, it is fully adequate in scope and quality as a dissertation for the degree of Doctor of Philosophy.

(Biondo L. Biondi) Principal Adviser

I certify that I have read this dissertation and that, in my opinion, it is fully adequate in scope and quality as a dissertation for the degree of Doctor of Philosophy.

(Jon F. Claerbout)

I certify that I have read this dissertation and that, in my opinion, it is fully adequate in scope and quality as a dissertation for the degree of Doctor of Philosophy.

(Gary Mavko)

Approved for the University Committee on Graduate Studies.

Abstract

Wave-equation inversion is a powerful technique able to build clean images with balanced amplitudes in complex subsurface areas relative to migration alone. The main contribution of this thesis is perform wave-equation inversion in image space without making any velocity model or acquisition geometry approximations. The method explicitly computes the least-squares Hessian matrix, defined from the modeling/migration operators, and uses an iterative solver to find the solution of the resulting system of equations. This technique is also 3-D, as it can handle 3-D data in a target-oriented fashion. This allows the method to improve the image where it is more important: in the neighborhood of the reservoir.

The Hessian matrix contains more information than just the amplitude of the diagonal elements; its rows are the point spread functions (PSFs) of the imaging system. In seismic imaging, the PSFs are non-stationary, due to the velocity model complexity, and the limited acquisition geometry. To make wave-equation inversion practical, I optimized the computation of the Hessian by taking advantage of the sparsity and structure of the matrix, the acquisition geometry, and the necessary frequency sampling. As a result, the computational savings can be of five orders of magnitude or greater compared to a direct implementation.

Wave-equation inversion in the presence of a complex overburden leads to an ill-conditioned system of equations that needs to be regularized to obtain a stable numerical solution. Regularization can be implemented in the poststack image-domain (zero subsurface offset), where the options for a regularization operator are limited to a customary damping, or in the prestack image-domain (subsurface offset), where

a physically-inspired regularization operator (differential semblance) can be applied. Though the prestack image-domain inversion is more expensive than the poststack image-domain inversion, it can improve the reflectors continuity into the shadow zones with an enhanced signal-to-noise ratio. I demonstrate the utility of both these methods by improving the subsalt-sediment images of the Sigsbee2B synthetic and a 3-D Gulf of Mexico field data set.

Acknowledgments

Contents

Abstract	v
Acknowledgments	vii
1 Introduction	1
2 Theory of imaging by wave-equation inversion	11
3 Structure and computation of the Hessian	25
4 Wave-equation inversion in practice	55
5 Field data examples	81
6 Conclusions	101
A Angle-domain Hessian	105
B Salt-related multiple removal	109

List of Tables

List of Figures

1.1	Snapshots of a wavefront as it propagates through a salt body. a) $t = 6.7$ s, b) $t = 6.9$ s, c) $t = 7.2$ s, and d) $t = 7.5$ s. The shot location is $x = 37000$ ft. The concave and convex features in the salt produce irregular amplitudes of the wavefront.	2
1.2	Illumination from four different shot positions: a) $x = 30000$ ft, b) $x = 35000$ ft, and c) $x = 37000$ ft, and d) $x = 39000$ ft. Light gray is high illumination, and dark gray is low illumination. The three shots are near one another in the surface but produce highly different illumination of the subsurface.	4
1.3	Cartoon illustrating the concept of the point spread function (PSF). The symbol $*$ means convolution.	6
1.4	a) Migration, b) diagonal of the Hessian (light gray is high and dark gray is low illumination), and c) inversion of the Sigsbee2b data set. The wave-equation inversion balances the amplitudes, and increases the spatial resolution of the image.	7
2.1	Angle gathers (a) well-illuminated zone, and (b) poorly illuminated zone.	19
2.2	Subsurface-offset gathers (a) well-illuminated zone, and (b) poorly-illuminated zone.	20

3.1	Silhouette of the nonzero elements of the Hessian matrix for a constant-velocity model with $v = 1.5$ km/s. The acquisition geometry contains all shots in the survey.	28
3.2	Close-up of the Hessian matrix from Figure 3.1 for a constant-velocity model with $v = 1.5$ km/s. The acquisition geometry contains all shots in the survey.	29
3.3	Silhouette of the nonzero elements of the Hessian matrix for a constant-velocity model with $v = 3$ km/s. The acquisition geometry contains all shots in the survey.	30
3.4	Close-up of the Hessian matrix from Figure 3.3 for a constant-velocity model with $v = 3$ km/s. The acquisition geometry contains all shots in the survey.	31
3.5	Four scatterers distributed around the model space.	31
3.6	Convolution of the Hessian matrix of the constant-velocity model $v = 1.5$ km/s (Figure 3.1) with the four-scatterer model (Figure 3.5). The acquisition geometry contains all shots in the survey.	32
3.7	Convolution of the Hessian matrix of the constant-velocity model $v = 3$ km/s (Figure 3.3) with the four-scatterer model (Figure 3.5). The acquisition geometry contains all shots in the survey. Compare with Figure 3.6, which uses a Hessian computed with a lower velocity.	32
3.8	Spatial Fourier transform of the convolution of the Hessian matrix of the constant-velocity model $v = 1.5$ km/s (Figure 3.6), with the four-scatterer model (Figure 3.5). The acquisition geometry contains all shots in the survey. Note the different spectral coverage in the (k_x, k_z) plane at each scatterer location.	34
3.9	Silhouette of the nonzero elements of the Hessian matrix for the constant-velocity model $v = 1.5$ km/s . The acquisition geometry contains only one shot positioned at $x = 0$ km.	35

3.10	Close-up of the Figure 3.9 Hessian matrix of the constant-velocity model $v = 1.5$ km/s. The acquisition geometry contains only one shot positioned at $x = 0$ km.	36
3.11	Convolution of the Hessian matrix of the constant-velocity model $v = 1.5$ km/s (Figure 3.9), with the four-scatterer model (Figure 3.5). The acquisition geometry contains only one shot positioned at $x = 0$ km. .	36
3.12	Sigsbee2B stratigraphic velocity model; target zone indicated with the “target” box.	38
3.13	Silhouette of the nonzero elements of the Hessian matrix of the Sigsbee2B velocity model (6650-point target).	39
3.14	Close-up of Figure 3.13. Hessian matrix of the Sigsbee2B model. . . .	40
3.15	Diagonal of the Hessian matrix of the Sigsbee2B model.	40
3.16	Convolution of the 32 point scatterers model with the Hessian matrix of the Sigsbee2B model in the target area. The non-stationarity of the PSF is evident.	41
3.17	Envelope of the convolution of the 32 point scatters model with the Hessian matrix of the Sigsbee2B model in the target area. The non-stationarity of the PSF is evident.	42
3.18	Spatial Fourier transform of the convolution of the 32 point scatterers model with the Hessian matrix of the Sigsbee2B model in the target area. Note the relative differences in spectral coverage in the (k_x, k_z) plane at each scatterer location.	43
3.19	Diagonal of the subsurface-offset Hessian matrix of the Sigsbee2B model.	44
3.20	Convolution of the 32-point-scatterer model with the Hessian matrix of the Sigsbee2B model in the subsurface-offset domain. The non-stationarity of the PSF is evident.	44

3.21	Convolution of the 32 point scatters model with the Hessian matrix of the Sigsbee2B model in the reflection-angle domain. The non-stationarity of the PSF is evident.	45
3.22	Sketch of the OBC acquisition, the gray boat shows a boat in one position, the black boat shows the boat in a different position. The rectangle shows where the receiver positions coincide for the two shots.	49
3.23	Sketch of the towed-streamers marine geometry; the gray color correspond to the first shot (top), and the black color corresponds to the shot in the next position (middle). The bottom sketch shows the two shots as they would occur in the the real experiment; the black rectangle shows where the receiver positions coincide for the two shots. .	50
3.24	PSF as a function of frequency sampling (equation 3.1). a) 2.44 Hz, b) 2.19 Hz, c) 1.95 Hz, d) 1.71 Hz, e) 1.46 Hz, f) 1.22 Hz, g) 0.97 Hz, h) 0.49 Hz, and i) 0.24 Hz. As the frequency sampling decreases, the wrap-around artifacts also decrease.	53
4.1	Inversion of the image of the 32 point scatterers after seven iterations of a conjugate-gradient iterative solver with no regularization. Compare with Figure 3.16, and notice how the amplitudes have been balanced, and the PSF size has been reduced.	57
4.2	Envelope of the inversion of the image of the 32 point scatterers after 7 iterations of a conjugate-gradient iterative solver and no regularization. Compare with the migration in Figure 3.17, and notice how the amplitudes have been balanced, and the PSF size has been reduced. .	58
4.3	Norm of the residuals as they change with number of iterations of a conjugate-gradient iterative solver for different regularization parameters ε in the poststack image domain. The parameter choice $\varepsilon = 0.5$ decreases the norm of the residuals, stabilizing the inversion.	59

4.4	Inversion of the image of the 32 point scatterers after 200 iterations of a conjugate-gradient iterative solver with regularization parameter $\varepsilon = 0.5$. Compare with Figures 3.16, notice how the amplitudes have been balanced, and the PSF size has been reduced. Compared with 4.1 the amplitudes in the shadow zone are weaker, but the result is cleaner.	59
4.5	Envelope of the inversion of the image of the 32 point scatterers after 200 iterations of a conjugate-gradient iterative solver with regularization parameter $\varepsilon = 0.5$. Compare with Figures 3.16, notice how the amplitudes have been balanced, and the PSF size has been reduced. Compared with 4.1 the amplitudes in the shadow zone are weaker, but the result is cleaner.	60
4.6	Norm of the residuals as they change with the number of iterations of a conjugate-gradient iterative solver, for different regularization parameters ε in the prestack image domain. The parameter choice $\varepsilon = 3.0$ makes the norm of the residuals decrease, stabilizing the inversion.	61
4.7	Inversion of the image of the 32 point scatterers in the subsurface-offset domain after seven iterations of the conjugate-gradient solver and no regularization. Compare with the migration (Figure 3.20); notice how the amplitudes have been balanced, and the size of the three dimensional PSF has been reduced, but the result is unstable in the shadow zone.	62
4.8	Inversion of the image of the 32 point scatterers in the reflection-angle domain (offset-to-angle transformation), after seven iterations of the conjugate-gradient solver and no regularization. Compare with Figure 3.21; notice how the gaps in the angle coverage has been partially filled by the inversion, the amplitudes have been balanced, and the PSF size has been reduced.	63

4.9	Inversion of the image of the 32 point scatterers in the subsurface-offset domain after 200 iterations of the conjugate-gradient solver and regularization parameter $\varepsilon = 3.0$. Compare with the migration in Figure 3.20 and the inversion without regularization in Figure 4.7; notice how the amplitudes have been balanced, and the size of the three dimensional PSF has been reduced.	64
4.10	Inversion of the image of the 32 point scatterers in the reflection-angle domain (offset-to-angle transformation) after 200 iterations of the conjugate-gradient solver and regularization parameter $\varepsilon = 3.0$. Compare with Figures 3.21 and 4.8; notice that the amplitudes have been balanced, and the PSF size has been reduced. Also, the inversion with regularization equalizes the amplitude in the angle gathers, filling the illumination gaps.	65
4.11	Zero subsurface-offset of the regularized inversion in the prestack image-domain (front panel of Figure 4.9), at the same scale as Figures 3.16, 4.1, and 4.4. Notice how the amplitudes have been balanced and the PSF size has been reduced.	66
4.12	Angle stack of the Sigsbee2B shot-profile migration (Figure 4.14). . .	67
4.13	Reflection coefficients of the Sigsbee2B model.	68
4.14	Sigsbee shot-profile migration (reflection angle) using a cross-correlation imaging condition. The front face corresponds to the image at a 25° reflection angle, and the side face corresponds to the reflection-angle gather at $x = 32300$ ft.	69
4.15	Sigsbee shot-profile migration (subsurface-offset) using cross-correlation imaging condition. The front face corresponds to the image at zero subsurface-offset, and the side face corresponds to the subsurface-offset gather at $x = 32300$ ft.	69

4.16	Angle stack of the Sigsbee2B shot-profile migration after filtering the salt-related multiple reflections (Figure B.7).	70
4.17	Inversion in the poststack image domain with the unfiltered migration as the input (equation 2.10) after seven iterations of a conjugate-gradient iterative solver and no regularization.	71
4.18	Inversion in the poststack image domain with a filtered migration as the input (equation 2.10) with a regularization parameter $\varepsilon = 2.0$	72
4.19	Residuals of the inversion in the poststack image domain with the unfiltered migration as the input (equation 2.10) after seven iterations, with a regularization parameter $\varepsilon = 0.0$	73
4.20	Residuals of the inversion in the poststack image domain with a filtered migration as the input (equation 2.10) after seven iterations, with a regularization parameter $\varepsilon = 0.0$	73
4.21	Sigsbee inversion without regularization in the subsurface-offset domain. The front face corresponds to the image at zero subsurface-offset, and the side face corresponds to the subsurface-offset gather at $x = 32300$ ft.	75
4.22	Sigsbee inversion without regularization in the reflection angle. The front face corresponds to the image at a 25° reflection angle, and the side face corresponds to the reflection-angle gather at $x = 32300$ ft.	75
4.23	Sigsbee regularized inversion in the subsurface-offset domain ($\varepsilon = 4.0$). The front face corresponds to the image at zero subsurface-offset, and the side face corresponds to the subsurface-offset gather at $x = 32300$ ft.	76
4.24	Sigsbee regularized inversion in the reflection angle ($\varepsilon = 4.0$). The front face corresponds to the image at 25° reflection angle, and the side face corresponds to the reflection-angle gather at $x = 32300$ ft.	77

4.25	Angle gathers corresponding to the migration (top row), the inversion without regularization (middle row), and the regularize inversion for $\varepsilon = 4.0$ (bottom row) at three locations. a), b), and g) $x = 32300$ ft; b), e), and h) $x = 33725$ ft; and c), f), and i) $x = 36500$ ft.	78
4.26	Angle stack of the inversion without regularization (the front panel of Figure 4.22 showed the result for just 25° reflection angle).	79
4.27	Angle stack of the regularized inversion with $\varepsilon = 4.0$ (the front panel of Figure 4.24 showed the result for just 25° reflection angle).	79
5.1	Velocity model for the 3-D Gulf of Mexico data; target zone indicated with the “target” box.	82
5.2	Diagonal of the Hessian matrix of the 3-D Gulf of Mexico data at two different locations in the target area. The low-illumination areas are dark gray, and high-illumination areas are light gray	84
5.3	Convolution of the 72-point-scatterer model with the 3-D Hessian matrix at two different locations in the target area. Notice the non-stationarity of the PSF.	85
5.4	Zero subsurface-offset image of the 3-D Gulf of Mexico data: a) 3-D shot profile migration, and b) 3-D inversion in the poststack-image domain with 2-D PSFs. Notice the improved balance and resolution in the inversion image.	87
5.5	Zero subsurface-offset image of the 3-D Gulf of Mexico data: a) 3-D shot profile migration, and b) 3-D inversion in the poststack-image domain with 2-D PSFs. Notice the improved balance and resolution in the inversion image.	88

5.6	3-D inversion in the poststack-image domain of the image in Figure 5.3a, a) with the 2-D PSF ($na_x = 15, na_y = 1, na_z = 30$), and b) with the 3-D PSF ($na_x = 15, na_y = 21, na_z = 30$). Compare with the input image in Figure 5.3a.	90
5.7	Zero subsurface-offset image of the 3-D Gulf of Mexico data: a) 3-D inversion in the poststack-image domain with the 2-D PSFs, b) 3-D inversion in the poststack-image domain with the 3-D PSFs. Notice the instability of the inversion when the 3-D PSFs are used.	92
5.8	Migrated image in the subsurface-offset domain. The figure shows two different offset gathers (side panel) corresponding to a crossline position of the 3-D migration.	94
5.9	Migrated image in the reflection-angle domain after offset-to-angle transformation. The figure shows two different reflection-angle gathers (side panel), and the corresponding angle sections (front panel), at the same crossline position of the 3-D migration as in Figure 5.8.	95
5.10	Inverted image in the subsurface-offset domain with the differential semblance as the regularization operator and $\varepsilon = 0.5$. Compare with Figure 5.8, and notice that the amplitudes have been balanced; the image is also more concentrated around zero subsurface offset.	96
5.11	Inverted image in the subsurface-offset domain, after an offset-to-angle transformation. Compared to the migration in Figure 5.9, note how the inversion plus regularization equalizes the amplitudes in the angle gathers.	97
5.12	Comparison of the angle-stack of a) the migration, with b) the inversion in the subsurface-offset domain, after an offset-to-angle transformation with regularization parameter $\varepsilon = 0.5$	99

5.13	Comparison of the angle-stack of the inversion in the subsurface-offset domain, after an offset-to-angle transformation with regularization parameter a) $\varepsilon = 0.01$, and b) $\varepsilon = 10$	100
B.1	Sigsbee shot-profile migration (reflection angle) using cross-correlation imaging condition. The front face corresponds to the image at 0° reflection angle, and the side face corresponds to the reflection-angle gather at $x = 36800$ ft position.	110
B.2	Sigsbee shot-profile migration (subsurface-offset) using cross-correlation imaging condition. The front face corresponds to the image at zero subsurface-offset, and the side face corresponds to the subsurface-offset gather at $x = 36800$ ft.	111
B.3	Depth slice at $z = 14150$ ft of the migration in the $k_x - k_h$ plane. . .	112
B.4	Primaries after bandpassing the migration (Figure B.3) in the $k_x - k_h$ plane.	112
B.5	The model for the multiples in the $k_x - k_h$ plane, obtained after subtraction of the filtered result (Figure B.4) from the migration (Figure B.3).	113
B.6	Sigsbee shot-profile migration (subsurface-offset) using cross-correlation imaging condition. The front face corresponds to the image at zero subsurface-offset, and the side face corresponds to the subsurface-offset gather at $x = 36800$ ft.	113
B.7	Sigsbee shot-profile migration (reflection angle) using cross-correlation imaging condition. The front face corresponds to the image at 0° reflection angle, and the side face corresponds to the reflection-angle gather at $x = 36800$ ft.	114

Chapter 1

Introduction

MOTIVATION

The seismic reflection method is invaluable for building images of the subsurface. As exploration targets have become more complex, however, conventional approaches have fallen short. This thesis presents a step toward improving the seismic images obtained in complex situations.

Two recent SEG¹ workshops were held to address the problems of imaging where the overburden is complex, as exemplified by the imaging of subsalt targets (Leveille et al., 2005; Sava, 2006). Although salt presence is only one source of complexity, salt bodies control the petroleum system in many basins worldwide (Fox, 1987). Examples of salt-controlled basins include the Gulf of Mexico, the North Sea, the Persian Gulf, offshore Brazil, and West Africa. The salt bodies are often associated with large hydrocarbon deposits because they provide favorable conditions for accumulation and trapping of oil and gas. Unfortunately, salt bodies create complications in the propagation of seismic waves, stretching the limits of applicability of conventional velocity analysis, migration, and multiple-suppression algorithms.

¹Society of Exploration Geophysicists

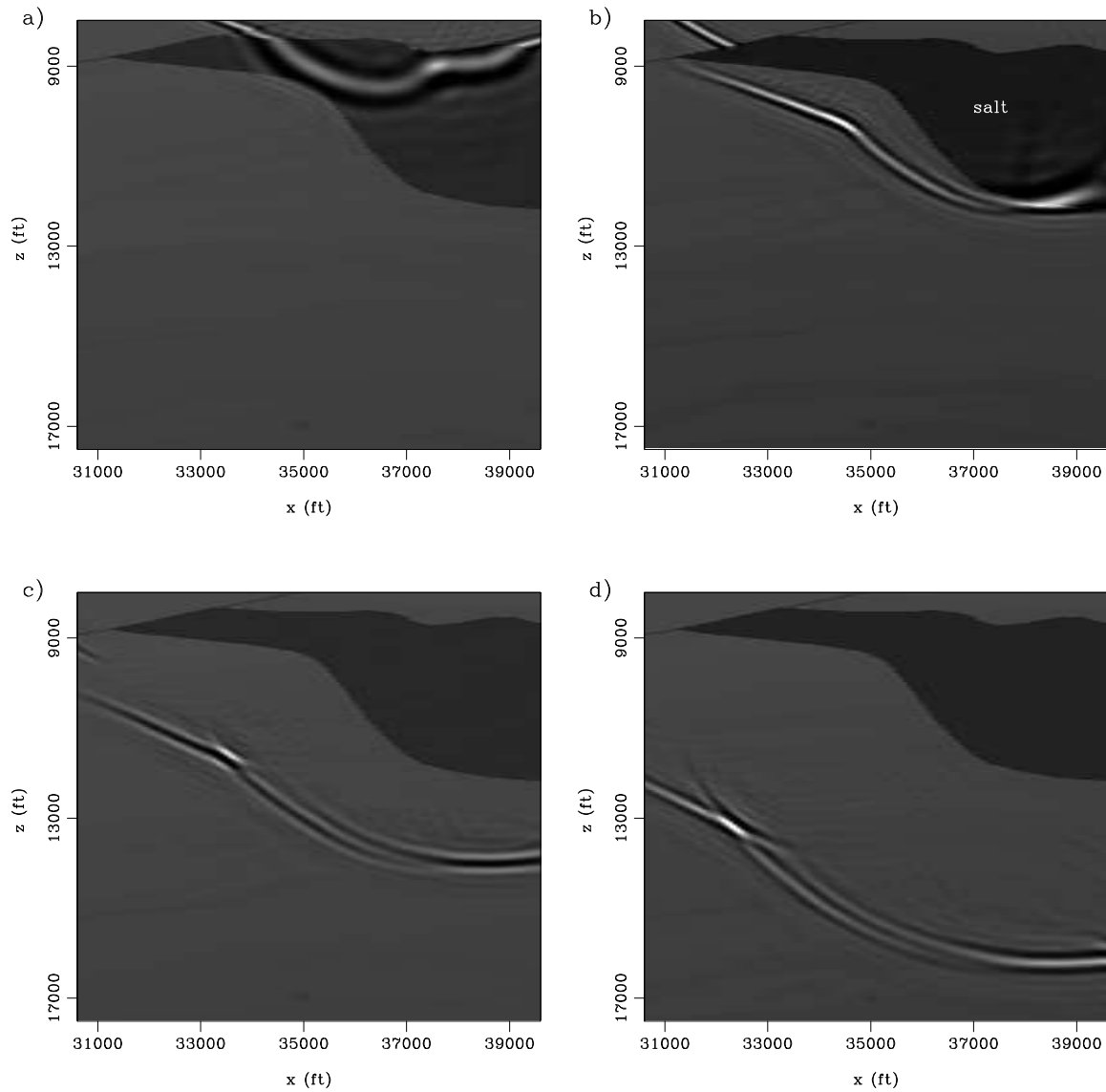


Figure 1.1: Snapshots of a wavefront as it propagates through a salt body. a) $t = 6.7$ s, b) $t = 6.9$ s, c) $t = 7.2$ s, and d) $t = 7.5$ s. The shot location is $x = 37000$ ft. The concave and convex features in the salt produce irregular amplitudes of the wavefront.

Intro/. green

Incomplete and irregular illumination: shadow zones

When all efforts fail to image subsalt targets, poor illumination is usually to blame. The high velocity contrast between the salt and the surrounding sediments reduces the amount of energy that propagates through the salt. That, combined with the focusing and defocusing produced by the rugosity of the top and bottom of the salt, distorts the illumination of the subsurface, as is illustrated by Figure 1.1 and 1.2.

Figure 1.1 shows four snapshots of a wavefront as it propagates through a salt body. Notice how the concave and convex features in the salt relate to amplitudes of the wavefront. The concave shape produces a triplication and consequent increase in amplitude, whereas the convex shape produces a divergence that results in a dimming of amplitude (Figures 1.1b and 1.1c).

I show later (chapter 2), that a measure of the illumination can be obtained by cross-correlating the Green's functions from the source to a point in the subsurface, with the sum of the Green's function from the receivers to the point at the subsurface. Figure 1.2 shows the corresponding illumination from four different source positions: $x = 30000$ ft, $x = 35000$ ft, $x = 37000$ ft, and $x = 39000$ ft, and a receiver array of 26100 ft to the right. Light gray is high illumination, and dark gray is low illumination. The three shots are near one another in the surface but produce highly different illumination of the subsurface, leaving areas with little or no shot coverage (shadow zones).

Improving illumination: processing versus acquisition

Hoping to improve illumination, the industry has started to acquire data with different shot and receiver configurations (Sayers and Herron, 2007). Multi-azimuth (MAZ), wide-azimuth (WAZ), and rich-azimuth (RAZ) methods have been proposed as alternatives to conventional narrow azimuth acquisition in marine environments (Michell et al., 2006; Keggin et al., 2006; Howard and Moldoveanu, 2006). They provide a richer coverage in azimuth, and improve the signal-to-noise ratio. However,

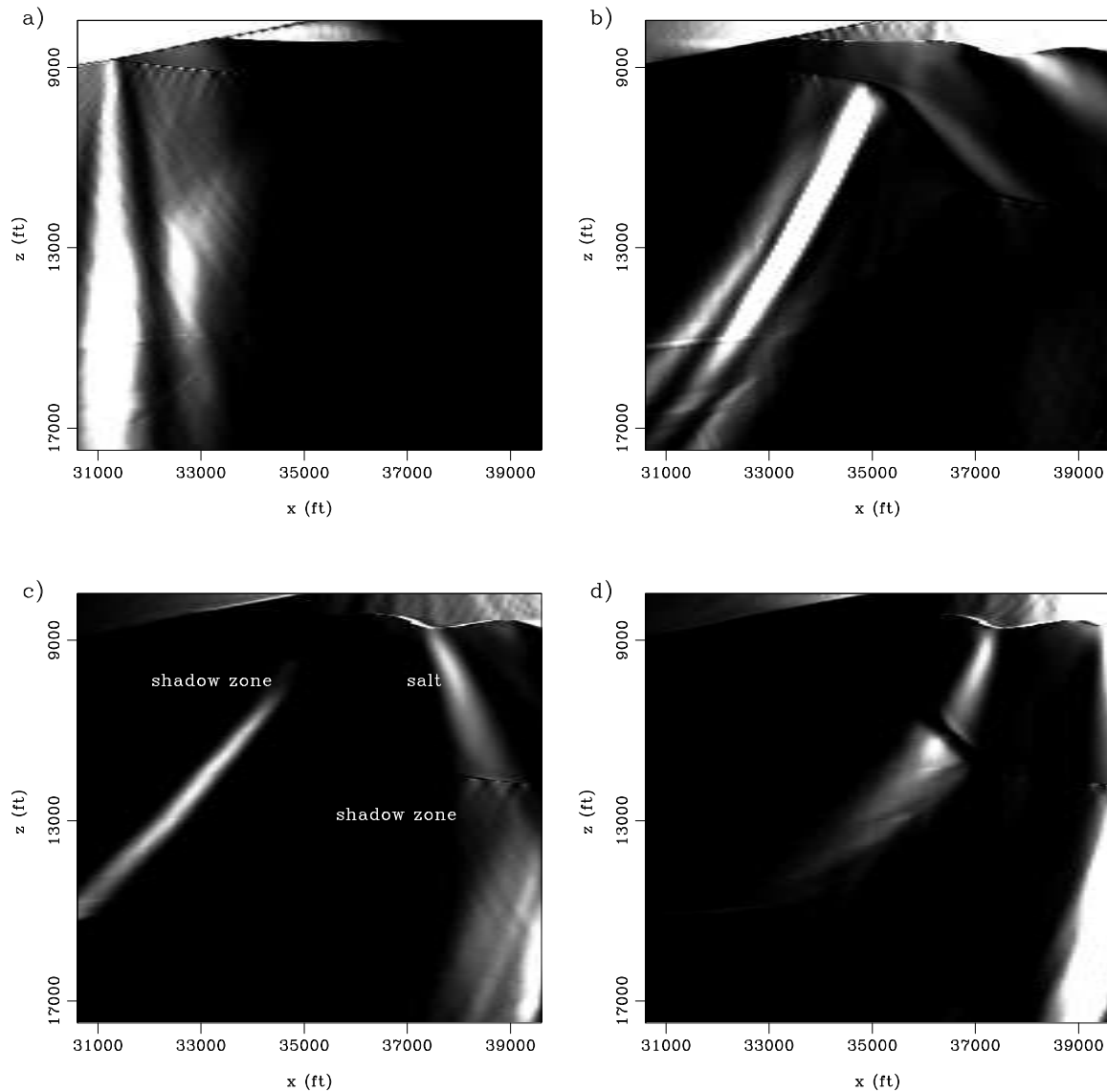


Figure 1.2: Illumination from four different shot positions: a) $x = 30000$ ft, b) $x = 35000$ ft, and c) $x = 37000$ ft, and d) $x = 39000$ ft. Light gray is high illumination, and dark gray is low illumination. The three shots are near one another in the surface but produce highly different illumination of the subsurface. Intro/. kernels

because they use cables with a limited length, and a coarse sampling in the cross-line direction, illumination holes and aliasing may still happen when the overburden is complex.

Much room remains, however, for improvement on the seismic data processing side, since the problem of incomplete illumination is reduced but not fully solved by innovative acquisition geometries. Wave-equation migration methods have become the standard when imaging in complex areas. With the increase of computing power, they can now use sophisticated one-way and two-way propagators. Unfortunately, if little reflections are recorded from an area (shadow zone), the migration algorithms fail to form a clean image, no matter how sophisticated the propagator is.

Balancing of the amplitudes after migration could be an alternative, since there is generally a weak signal obscured by noise in the shadow zones. Conventional methods to perform this task can be based on the statistics of the amplitude of the image like automatic gain control (AGC), or based on approximations of the illumination (Hu et al., 2001; Rickett, 2003; Plessix and Mulder, 2004). Balancing the amplitudes with an approximation of the illumination can work well in areas with good illumination. However, as these methods can not discriminate between noise and signal, they often fail to recover the reflectors in the shadow zones.

Thesis main contribution

In this thesis I propose to mitigate the problem of irregular illumination during data processing by using least-squares wave-equation inversion with a physically-inspired regularization. My main contribution is the development of a methodology to explicitly compute the least-squares Hessian matrix (defined from the modeling/migration operators) and solve the regularized wave-equation inversion in image space. The method does not make any compromises about the complexity of the velocity model or the acquisition geometry. It can be used in a target-oriented fashion, allowing it to handle 3-D data.

Figure 1.4 illustrates how the proposed wave-equation inversion works in a synthetic data set. The problem created by the irregular illumination can be seen in the weak amplitudes beneath the dipping base of the salt in the migrated image (Figure 1.4a). Figure 1.4b shows the diagonal of the least-squares Hessian matrix; note the correlation between the shadow zones (zones with low illumination) and the dimming in the amplitudes of the subsalt reflectors in the migrated image (Figure 1.4a).

In addition to this correlation, more information is available in the Hessian matrix than just the amplitude of the diagonal elements; the off-diagonal terms contain information on the Point Spread Function (PSF) of the seismic imaging system. In general, the PSF describes the impulse response of an imaging system to a point source. In many contexts it can be thought of as the extended blob in an image that represents an unresolved object (Figure 1.3). The degree of spreading (blurring) of the point object is a measure for the quality of an imaging system. In the specific case of the seismic imaging system, the PSF is non-stationary, as a consequence of the complexity of the velocity model and the acquisition geometry.

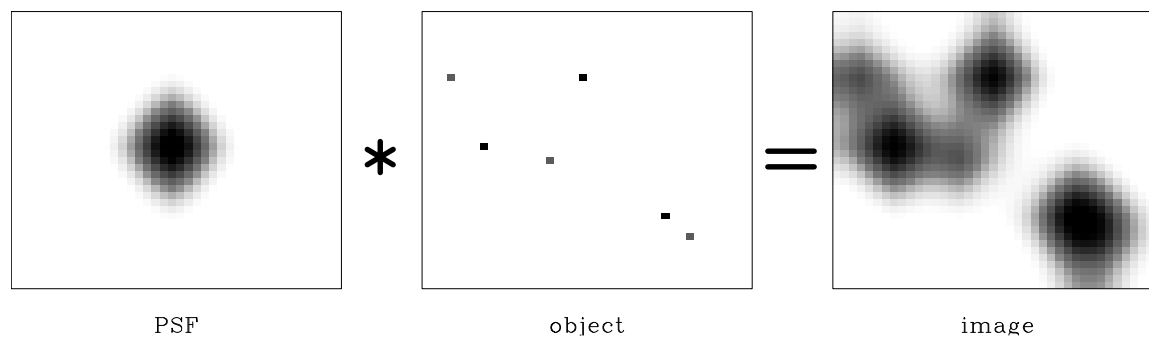


Figure 1.3: Cartoon illustrating the concept of the point spread function (PSF). The symbol $*$ means convolution. [Intro/. psf](#)

Knowing the PSF is particularly useful inside shadow zones, since inversion could reverse the spreading of the energy and recover the amplitudes. After the migration is deblurred by wave-equation inversion, the resulting image (Figure 1.4c) has more balanced amplitudes and better spatial resolution than does the migrated image. Also, the subsalt reflectors can be further interpreted into the shadow zones.

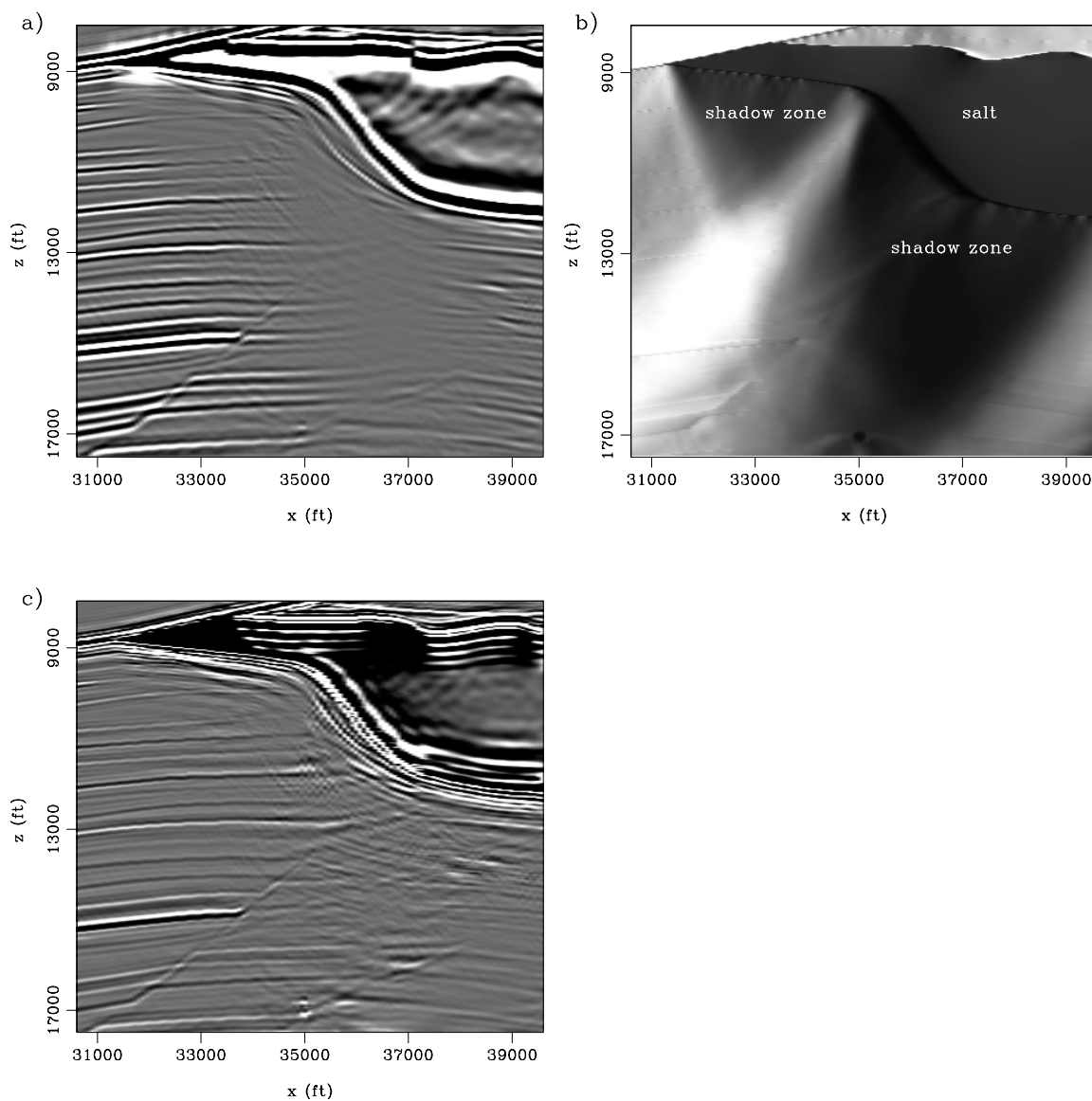


Figure 1.4: a) Migration, b) diagonal of the Hessian (light gray is high and dark gray is low illumination), and c) inversion of the Sigsbee2b data set. The wave-equation inversion balances the amplitudes, and increases the spatial resolution of the image.

Intro/. illu-mig

THESIS OVERVIEW

Chapter 2: Theory of imaging by wave-equation inversion

In chapter 2, I give an introduction and description of previously published work in the area of wave-equation inversion. I also explain why linear least-squares inversion is an ill-posed problem that needs to be regularized to obtain a stable numerical solution.

I pose modeling and migration in a target-oriented fashion, allowing derivation of the Hessian in the poststack image domain. This is one of the most important results of the thesis, since it permits solution of the inversion problem in image space.

Towards the end, I explain that it is necessary to expand the dimensionality of the Hessian to allow a physical regularization that complies with the semblance principle, either in the reflection-angle domain or the subsurface-offset domain. To conclude, I derive the Hessian in the prestack image-domain and explain the different options for regularization of prestack-image domain inversion.

Chapter 3: Structure and computation of the Hessian matrix

Chapter 3 is divided into two main parts. In the first part I give the geophysical interpretation of the Hessian matrix, explaining with a constant-velocity model how the background velocity, depth, and acquisition geometry govern the number of nonzero off-diagonal terms of the Hessian matrix. Next, I use the Sigsbee2B model to illustrate properties of the Hessian in the presence of complex overburden. This is an important section of the thesis since it illustrates why previous approximations to the Hessian matrix fail to capture its spatial variability where overburden is complex.

The second part explains the explicit numerical computation of the Hessian, including the approximations necessary to compute it for a 3D model. Computational savings result from the sparsity and structure of the Hessian, the redundancy in the acquisition geometry, and the frequency sub-sampling. I describe each approximation

and give the pseudo-code that shows the value each has for reduction in computational cost.

Chapter 4: Wave-equation inversion in practice

In chapter 4, I introduce inversion results. I use a 32-scatterer image to illustrate how the inversion works in the case of the Hessian matching the physics used in migration.

Later, I use the Sigsbee2B data to show the influence of irregular illumination on the migration and to illustrate the need to filter events that do not comply with the modeling used to compute the Hessian. Last, I show poststack image-domain inversion results and compare them with those obtained by prestack image-domain inversion. I also test and compare different regularization approaches.

Chapter 5: Field data examples

In chapter 5, I show the 3D Hessian corresponding to a field data from the Gulf of Mexico. I also explain the approximations and the computational resources that allowed its numerical computation.

I apply the inversion described in chapter 4, in the poststack image domain with 2-D and 3-D Point Spread Functions. At the end I show the results of doing the inversion in the prestack image domain.

Chapter 6: Conclusions

Chapter 6 summarizes the main results and conclusions obtained in the thesis. I also briefly discuss possible research directions to improve the method.

Chapter 2

Theory of imaging by wave-equation inversion

INTRODUCTION AND HISTORICAL BACKGROUND

Seismic imaging (modeling/migration) operators are non-unitary (Claerbout, 1992, 1985, 2001), meaning that if \mathbf{L} is a modeling operator, and \mathbf{L}' is its adjoint (migration), their product $\mathbf{L}'\mathbf{L} \neq \mathbf{I}$, where \mathbf{I} is the identity matrix. As a result, images of the subsurface are blurred when produced by a migration operator. Even for a simple subsurface, the bandlimited characteristic of the seismic data in the time and space domain would prevent \mathbf{L} and \mathbf{L}' from being unitary (Claerbout, 1985; Chavent and Plessix, 1999; Plessix and Mulder, 2004). Moreover, where the subsurface is complex, and the seismic acquisition geometry is limited and irregular, the non-unitary characteristic of the imaging operators causes migration to produce images with artifacts and biased amplitudes.

One way to improve on the use of an adjoint operator such as that for migration is to use inversion (Tarantola, 1987). The general inversion framework has been employed in a number of geophysical applications from non-linear elastic waveform-inversion (Mora, 1987) to waveform tomography (Pratt and Worthington, 1988).

The inversion problem can be linearized depending of the choice of parameters to invert. The “relative reflectivity” can be inverted from the seismic data to obtain images that better represent the subsurface properties and geometry than do those from migration (Nemeth et al., 1999; Prucha and Biondi, 2002; Kuhl and Sacchi, 2003; Clapp, 2005). The assumption behind the linearization (as for migration) is that the long-wavelength model (migration velocity) is known.

Solution of the Ill-posed inversion problem

Solving linear systems generally is not difficult, but the high dimensionality and the ill-posedness of the seismic-imaging inverse problem in complex areas, makes its solution challenging. There are two main physical reasons for this. The first is the limited and irregular acquisition geometry of the seismic experiment (Nemeth et al., 1999; Duquet and Marfurt, 1999; Ronen and Liner, 2000). The second is the complexity of the overburden (Rickett, 2003; Guitton, 2004; Clapp, 2005). These two effects combined produce incomplete and irregular illumination of the subsurface. In the worst cases “shadow zones” can be created. These are subsurface regions from which the seismic experiment yields recorded reflections that are too weak to be imaged well in a background of noise and diffractions. Two other contributors to the difficulty of solving the seismic imaging inverse problem are: (1) coherent noise that usually contaminates the seismic data, and (2) the approximations we use to model the propagation of the seismic waves in the earth.

Two main lines of attack to solve the inverse problem have been discussed in the literature, both based on least-squares. The first is to approximate the inverse of the least-squares Hessian ($\mathbf{L}'\mathbf{L}$) to reduce the computational cost. Hu et al. (2001) introduced a horizontally invariant non-diagonal Hessian for $v(z)$ media; Rickett (2003) proposed to compute a diagonal Hessian from reference images; Plessix and Mulder (2004) proposed to compute a diagonal Hessian using analytical approximations for the contribution of the receiver-side Green’s functions; and Guitton (2004) used a bank of non-stationary matching filters to approximate a non-diagonal inverse of

the Hessian. The second type of approach is computationally more challenging but can deliver a better performance. It finds the least-squares solution by means of an iterative solver. Nemeth et al. (1999) first proposed this approach using Kirchhoff operators; more recently, Prucha and Biondi (2002), Kuhl and Sacchi (2003), and Clapp (2005) proposed to use wave-equation operators that seem more suitable for complex areas.

Since accurate imaging of reflectors is most important at the reservoir level, I propose to explicitly compute an approximation of the Hessian in a target-oriented fashion. Computing the Hessian in a region of the model space allows reduction of the Hessian matrix size by a large factor, thereby, allowing reduction in the number of approximations used in its computation. After I compute a non-diagonal Hessian matrix, I use an iterative algorithm to obtain the inverse image.

The discretization of the ill-posed least-squares inversion produces an ill-conditioned system of equations (Hanke, 1995). The conventional approach to that problem is to stabilize it by re-formulating it for numerical treatment, commonly using some form of regularization (Tikhonov and Arsenin, 1977). Regularization also has its statistical interpretation, that of adding prior information on the model covariance, in this case on the properties of the reflectivity. From the results reported by Prucha and Biondi (2002), Kuhl and Sacchi (2003), and Clapp (2005), a regularization in the prestack image domain (reflection-angle) can help to stabilize the inversion.

LINEAR LEAST-SQUARES INVERSION

Wave-equation inversion can be linearized in various ways depending of the choice of the parameters to invert. If the medium velocity is assumed known, the inversion can be formulated as a linear problem, modeling the seismic data from the reflectivity as a function of offset (Nemeth et al., 1999) or as a function of angle (Prucha and Biondi, 2002; Kuhl and Sacchi, 2003; Clapp, 2005).

Linear least-squares inversion provides a theoretical approach to compensating for experimental deficiencies (e.g., limited acquisition geometry), and complexities of the

overburden, while maintaining consistency with the acquired data. For seismic imaging, it can be summarized as follows. Given a linear modeling operator \mathbf{L} , compute synthetic data \mathbf{d} using,

$$\mathbf{d} = \mathbf{L}\mathbf{m}, \quad (2.1)$$

where \mathbf{m} is a reflectivity model.

The quadratic cost function,

$$S(\mathbf{m}) = \|\mathbf{d} - \mathbf{d}_{obs}\|^2 = \|\mathbf{L}\mathbf{m} - \mathbf{d}_{obs}\|^2, \quad (2.2)$$

is formed, where \mathbf{d}_{obs} denotes the recorded data.

Up to this point, no prior information about the covariance of the model (model regularization) has been included in the definition of the cost function. I will ignore the need of regularization here, but in a later subsection, I will show how to add regularization to solve the otherwise ill-posed inversion problem.

The reflectivity model $\hat{\mathbf{m}}$ that minimizes $S(\mathbf{m})$ is given by

$$\hat{\mathbf{m}} = (\mathbf{L}'\mathbf{L})^{-1}\mathbf{L}'\mathbf{d}_{obs} = \mathbf{H}^{-1}\mathbf{m}_{mig}, \quad (2.3)$$

where \mathbf{L}' (the migration operator) is the adjoint of the linear modeling operator \mathbf{L} , \mathbf{m}_{mig} is the migration image, $\mathbf{m}_{mig} = \mathbf{L}'\mathbf{d}_{obs}$, and $\mathbf{H} = \mathbf{L}'\mathbf{L}$ is the Hessian of $S(\mathbf{m})$.

Two possible ways to obtain the inverse image are suggested by equation 2.3. One solves the linear system by iteratively evaluating the forward operator \mathbf{L} and its adjoint \mathbf{L}' (implicit method), and the other solves it by explicitly computing the Hessian matrix.

The choice between the two methods generally depends on the problem. In seismic imaging, the forward operator and its adjoint can be represented by full matrices, making their evaluation a computationally expensive process. Each iteration of the implicit method using a solver such as conjugate gradients involves one evaluation of the forward and one of the adjoint operator. Because, according to theory, the

conjugate-gradient method converges in a number of iterations roughly equal to the size of the model space, iteration until convergence with the implicit method is impossible for today's computer resources (Clapp, 2005). Still, Clapp (2005) proved that after a small number of iterations, the image resulting from the inversion is better than the image resulting from the migration.

The explicit method has a big advantage over the implicit method: after the Hessian matrix is computed, different inversion schemes can be used without having to incur the cost of wavefield propagation. Another advantage is in the parameterization of the inversion. In practice, inversion always requires parameter adjustments, which can be very expensive in the implicit case, since every time an inversion parameter is changed, wavefield propagation will be needed.

But the explicit method also has problems. Since the model space can be large, computing the inverse of the Hessian matrix is a big challenge for most geophysical imaging problems. For this reason, it is often more feasible to compute the inverse image as the solution of the linear system of equations

$$\mathbf{H}\hat{\mathbf{m}} = \mathbf{m}_{mig}, \quad (2.4)$$

by using an iterative inversion algorithm. Again the conjugate-gradient method can be used; however, this time only one matrix-vector multiplication of the Hessian matrix with the model vector is necessary per iteration. Still, explicit computation of the Hessian for the entire model space is too expensive in practice. In the next chapter, I discuss how exploiting the structure of the Hessian matrix and the localization in the model space makes this problem tractable.

The next sections describe the theory for computing the Hessian matrix \mathbf{H} and how to set up the linear system of equations 2.4 in different domains: poststack image, subsurface-offset, and reflection-angle.

TARGET-ORIENTED MODELING AND DERIVATION OF THE HESSIAN IN THE POSTSTACK IMAGE DOMAIN

Definition of the poststack image-domain Hessian

In general, the synthetic data for one frequency, ω , a shot positioned at $\mathbf{x}_s = (0, x_s, y_s)$, and a receiver positioned at $\mathbf{x}_r = (0, x_r, y_r)$, can be given by a linear operator \mathbf{L} acting on the model $\mathbf{m}(\mathbf{x})$, with $\mathbf{x} = (z, x, y)$, as follows:

$$\mathbf{d}(\mathbf{x}_s, \mathbf{x}_r; \omega) = \mathbf{L}\mathbf{m}(\mathbf{x}) = \sum_{\mathbf{x}} \mathbf{G}(\mathbf{x}, \mathbf{x}_s; \omega) \mathbf{G}(\mathbf{x}, \mathbf{x}_r; \omega) \mathbf{m}(\mathbf{x}), \quad (2.5)$$

where $\mathbf{G}(\mathbf{x}, \mathbf{x}_s; \omega)$ and $\mathbf{G}(\mathbf{x}, \mathbf{x}_r; \omega)$ are the Green's functions from the shot position \mathbf{x}_s and from the receiver position \mathbf{x}_r , to a point in the model space \mathbf{x} . Here I use the one-way approximation to the acoustic wave equation.

The quadratic cost function is

$$\begin{aligned} S(\mathbf{m}) &= \frac{1}{2} \sum_{\omega} \sum_{\mathbf{x}_s} \sum_{\mathbf{x}_r} \|\mathbf{d} - \mathbf{d}_{obs}\|^2 \\ &= \frac{1}{2} \sum_{\omega} \sum_{\mathbf{x}_s} \sum_{\mathbf{x}_r} [\mathbf{d}(\mathbf{x}_s, \mathbf{x}_r; \omega) - \mathbf{d}_{obs}]' [\mathbf{d}(\mathbf{x}_s, \mathbf{x}_r; \omega) - \mathbf{d}_{obs}]. \end{aligned} \quad (2.6)$$

its first derivative, with respect to the model parameters $\mathbf{m}(\mathbf{x})$, is a linear function of \mathbf{m} :

$$\begin{aligned} \frac{\partial S(\mathbf{m})}{\partial \mathbf{m}(\mathbf{x})} &= \frac{1}{2} \sum_{\omega} \sum_{\mathbf{x}_s} \sum_{\mathbf{x}_r} \{ \mathbf{G}'(\mathbf{x}, \mathbf{x}_r; \omega) \mathbf{G}'(\mathbf{x}, \mathbf{x}_s; \omega) [\mathbf{d}(\mathbf{x}_s, \mathbf{x}_r; \omega) - \mathbf{d}_{obs}] \\ &\quad + [\mathbf{d}(\mathbf{x}_s, \mathbf{x}_r; \omega) - \mathbf{d}_{obs}]' \mathbf{G}(\mathbf{x}, \mathbf{x}_r; \omega) \mathbf{G}(\mathbf{x}, \mathbf{x}_s; \omega) \}. \end{aligned} \quad (2.7)$$

The second derivative with respect to the model parameters $\mathbf{m}(\mathbf{x})$ and $\mathbf{m}(\mathbf{x}')$ is the

Hessian:

$$\mathbf{H}(\mathbf{x}, \mathbf{x}') = \frac{\partial^2 S(\mathbf{m})}{\partial \mathbf{m}(\mathbf{x}) \partial \mathbf{m}(\mathbf{x}')} = \sum_{\omega} \sum_{\mathbf{x}_s} \mathbf{G}'(\mathbf{x}, \mathbf{x}_s; \omega) \mathbf{G}(\mathbf{x}', \mathbf{x}_s; \omega) + \sum_{\mathbf{x}_r} \mathbf{G}'(\mathbf{x}, \mathbf{x}_r; \omega) \mathbf{G}(\mathbf{x}', \mathbf{x}_r; \omega), \quad (2.8)$$

where $\mathbf{G}'(\mathbf{x}, \mathbf{x}_r; \omega)$ is the adjoint of $\mathbf{G}(\mathbf{x}, \mathbf{x}_r; \omega)$.

Having the Hessian expressed in terms of summations of Green's function multiplications from a point in the subsurface to points in the surface allows us to solve the linear system defined by equation 2.4 in a target-oriented fashion. Notice that computing $\mathbf{H}(\mathbf{x}, \mathbf{x}')$ in equation 2.8 needs only the Green's functions at model points \mathbf{x} to the surface (\mathbf{x}_s and \mathbf{x}_r). Thus, the size of the problem can be considerably reduced by computing the Green's functions only at the target locations \mathbf{x}_T , reducing equation 2.8 to

$$\mathbf{H}(\mathbf{x}_T, \mathbf{x}'_T) = \sum_{\omega} \sum_{\mathbf{x}_s} \mathbf{G}'(\mathbf{x}_T, \mathbf{x}_s; \omega) \mathbf{G}(\mathbf{x}'_T, \mathbf{x}_s; \omega) + \sum_{\mathbf{x}_r} \mathbf{G}'(\mathbf{x}_T, \mathbf{x}_r; \omega) \mathbf{G}(\mathbf{x}'_T, \mathbf{x}_r; \omega), \quad (2.9)$$

where the points \mathbf{x}_T are points \mathbf{x} within the chosen target region.

The cost savings achieved by computing the Hessian via equation 2.9 instead of equation 2.8 depends on the squared ratio of the number of elements in the target model space to that in the original full model space $\left(\frac{n_{x_T} n_{y_T} n_{z_T}}{n_x n_y n_z}\right)^2$ where (n_x, n_y, n_z) are the number of samples in the full model space, and $(n_{x_T} n_{y_T} n_{z_T})$ are the number of samples in the target model space.

Regularization of the inversion in the poststack image domain

The linear system of equations 2.4 is ill-posed when the illumination of the subsurface is highly irregular (shadow zones). The zones with lower illumination are related to the null space of the system (Clapp, 2005). The system needs to be modified for numerical treatment with some form of regularization (Tikhonov and Arsenin, 1977).

Regularization also has a statistical interpretation, which is adding prior information on the model's covariance to the solution of the inverse problem. Clapp (2005) proposed two different regularizations, one *geological* and the other *geophysical*. The first was based on a preconception of the behavior of the seismic reflectors in $\mathbf{x} = (x, y, z)$. That *geological* regularization was implemented by using steering filters (Clapp et al., 2004). The idea of her approach is to favor the dips in the image that agree with a prior interpretation. This helps to fill the areas in the image where the illumination is poor, but has the drawback that it suppresses other dips when multiple dips are present in the image, resulting in a smooth result.

I choose to use a more customary regularization for the inversion in the poststack image domain: to add a damping factor that penalizes an increase of the values of the model. This regularization makes no use of any physical knowledge we might have about the seismic reflectors. It is implemented by adding a small value to the diagonal of $\mathbf{H}(\mathbf{x}, \mathbf{x}')$ in equation 2.4:

$$(\mathbf{H} + \varepsilon\mathbf{I}) \hat{\mathbf{m}} - \mathbf{m}_{mig} = \mathbf{r} \approx 0, \quad (2.10)$$

where \mathbf{I} is the identity operator, \mathbf{r} is the residuals vector, and ε is an scalar parameter that governs the strength of the regularization.

Although the result of solving equation 2.10 with a conjugate-gradient solver is more stable than the equivalent with equation 2.4, in a sense, the two operators in equation 2.10 compete against each other during the minimization process. To obtain a result with noise minimally enhanced, the ε value needs to be sufficiently high. But to the extent that $\mathbf{H} + \varepsilon\mathbf{I}$ differs from \mathbf{H} , we have in essence changed the subsurface model from the one defined by our chosen model parameters, thus obstructing the work of the multidimensional deconvolution by \mathbf{H} in $\mathbf{x} = (z, x, y)$. In chapter 4, I demonstrate with a synthetic dataset the advantages and disadvantages of this approach.

EXPANDING THE DIMENSIONALITY OF THE HESSIAN: INVERSION IN THE PRESTACK IMAGE DOMAIN

If the correct velocity is used during migration, the *semblance principle* will hold (Yilmaz, 1987; Stolk and Symes, 2002). This principle has different meanings depending of the kind of image gathers we are using. For angle image gathers, the events along the reflection-angle dimension would be flat (de Bruin et al., 1990; Prucha et al., 1999). In addition, the reflectivity would vary smoothly (Shuey, 1985; Richter, 1941), and any sudden changes in amplitude with angle (AVA) would be indicative of illumination problems. If subsurface-offset image gathers are used, then the energy should be focused at zero subsurface offset (Claerbout, 1985).

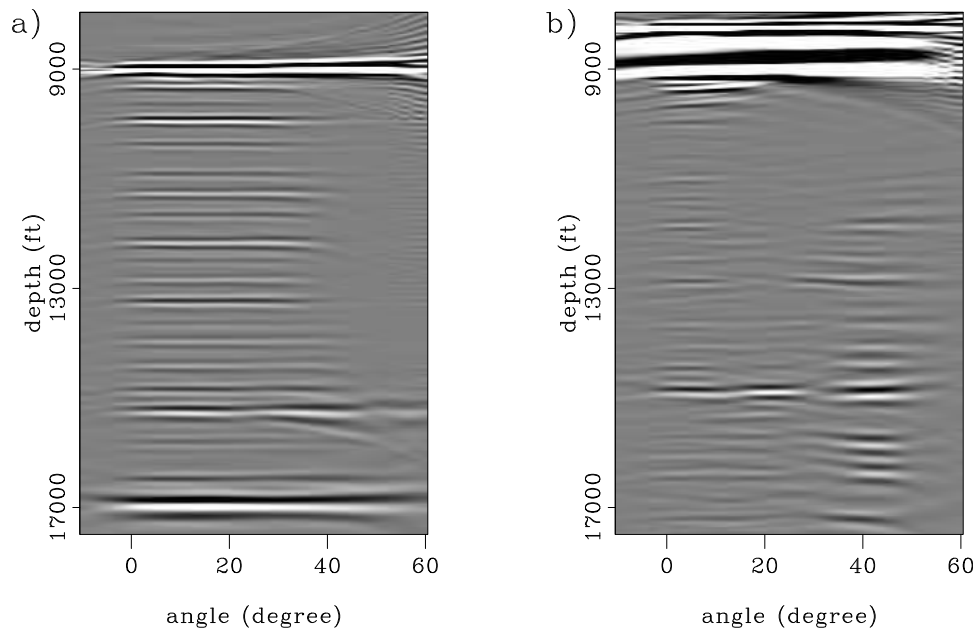


Figure 2.1: Angle gathers (a) well-illuminated zone, and (b) poorly illuminated zone.

Theo-Inversion/. ang-gandb

Figures 2.1 and 2.2 exemplify the semblance principle in two different locations of

the Sigsbee2b model. Figures 2.1a and 2.2a show an angle gather and a subsurface-offset gather corresponding to a well-illuminated zone. The reflectors in the angle gather are flat and smoothly varying, and the energy is mainly concentrated at zero subsurface offset in the subsurface-offset gather. In contrast, figures 2.1b and 2.2b show an angle gather and a subsurface-offset gather corresponding to a poorly-illuminated zone. Notice how the illumination problem alters the image of the reflectors in the different gathers. In this location the reflectors in the angle gather are discontinuous, and the energy is spread away from zero subsurface offset in the subsurface-offset gather.

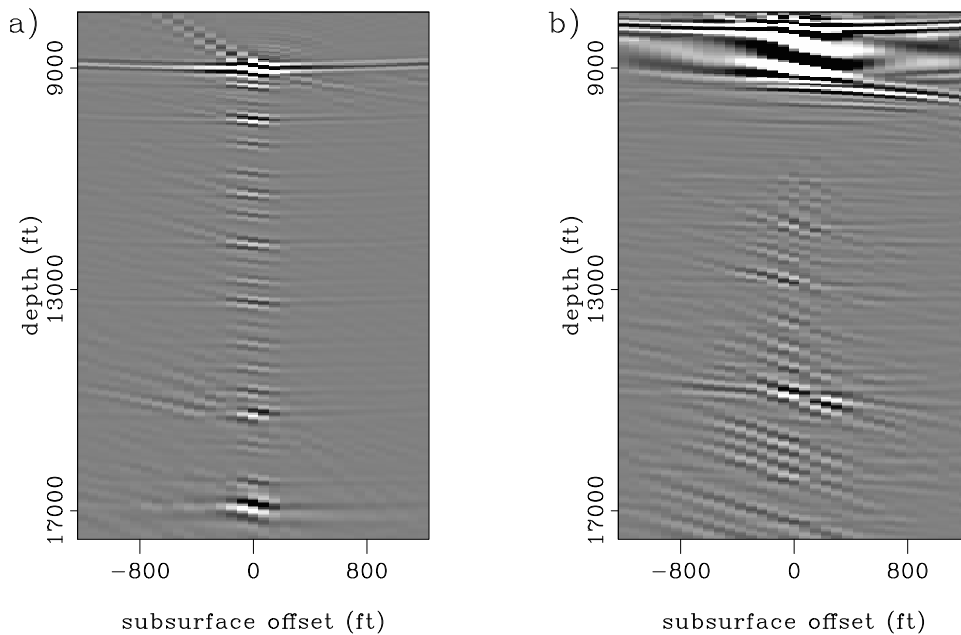


Figure 2.2: Subsurface-offset gathers (a) well-illuminated zone, and (b) poorly-illuminated zone. `Theo-Inversion/. off-gandb`

Taking that into account, the regularization can be designed to add the prior knowledge of the properties of the reflectivity in a well-illuminated zone. In the reflection-angle domain (or offset ray-parameter), this corresponds to applying a derivative operator to impose smoothness of the AVA (Stolk and Symes, 2002; Prucha and Biondi, 2002; Kuhl and Sacchi, 2003; Clapp, 2005). In the subsurface-offset dimension (which is the Fourier dual domain of the offset ray-parameter), it consists of

penalizing the energy in the image that is not focused at zero subsurface offset (Stolk and Symes, 2002; Shen et al., 2003). These two approaches are more physically-justified regularizations than the damping regularization used in equation 2.10, but they imply an expansion of the depth-midpoint model space to include either subsurface offset or reflection angle.

Another benefit of expanding the dimensionality of the model is that it allows us to include the new dimension in the multidimensional deconvolution (equation 2.4). In principle, if the modeling accounts for illumination problems correctly, the multidimensional deconvolution should compensate for illumination problems in the new dimension (subsurface-offset or reflection-angle).

Definition of the subsurface-offset Hessian

The prestack migration image in the subsurface-offset domain (Rickett and Sava, 2000) for a group of shots positioned at $\mathbf{x}_s = (x_s, y_s, 0)$ and a group of receivers positioned at $\mathbf{x}_r = (x_r, y_r, 0)$, is given by the adjoint of a linear operator \mathbf{L} acting on the data $\mathbf{d}(\mathbf{x}_s, \mathbf{x}_r; \omega)$ as

$$\begin{aligned} \mathbf{m}_{mig}(\mathbf{x}, \mathbf{h}) &= \mathbf{L}'\mathbf{d}(\mathbf{x}_s, \mathbf{x}_r; \omega) \\ &= \sum_{\omega} \sum_{\mathbf{x}_s} \sum_{\mathbf{x}_r} \mathbf{D}'(\mathbf{x} - \mathbf{h}, \mathbf{x}_s; \omega) \mathbf{U}(\mathbf{x} + \mathbf{h}, \mathbf{x}_r; \omega) \\ &= \sum_{\omega} \sum_{\mathbf{x}_s} \sum_{\mathbf{x}_r} \mathbf{G}'(\mathbf{x} - \mathbf{h}, \mathbf{x}_s; \omega) \mathbf{G}'(\mathbf{x} + \mathbf{h}, \mathbf{x}_r; \omega) \mathbf{d}(\mathbf{x}_s, \mathbf{x}_r; \omega), \end{aligned} \quad (2.11)$$

where \mathbf{D} and \mathbf{U} are the source and receiver wavefields, $\mathbf{G}(\mathbf{x}, \mathbf{x}_s; \omega)$ and $\mathbf{G}(\mathbf{x}, \mathbf{x}_r; \omega)$ are the Green's functions from shot position \mathbf{x}_s and receiver position \mathbf{x}_r respectively, to a model space point $\mathbf{x} = (x, y, z)$, and $\mathbf{h} = (h_x, h_y, h_z)$ is the subsurface offset.

The synthetic data can be modeled by the adjoint of equation 2.11;

$$\begin{aligned} \mathbf{d}(\mathbf{x}_s, \mathbf{x}_r; \omega) &= \mathbf{L}\mathbf{m}(\mathbf{x}, \mathbf{h}) \\ &= \sum_{\mathbf{x}} \sum_{\mathbf{h}} \mathbf{G}(\mathbf{x} + \mathbf{h}, \mathbf{x}_r; \omega) \mathbf{G}(\mathbf{x} - \mathbf{h}, \mathbf{x}_s; \omega) \mathbf{m}(\mathbf{x}, \mathbf{h}), \end{aligned} \quad (2.12)$$

where the linear operator \mathbf{L} acts on the model $\mathbf{m}(\mathbf{x}, \mathbf{h})$.

After having defined the modeling operator (equation 2.12), we can now compute the prestack image-domain Hessian. The procedure is the same as the one we used for the poststack image domain.

The quadratic cost function is again defined as

$$\begin{aligned} S(\mathbf{m}) &= \frac{1}{2} \sum_{\omega} \sum_{\mathbf{x}_s} \sum_{\mathbf{x}_r} \|\mathbf{d} - \mathbf{d}_{obs}\|^2 \\ &= \frac{1}{2} \sum_{\omega} \sum_{\mathbf{x}_s} \sum_{\mathbf{x}_r} [\mathbf{d}(\mathbf{x}_s, \mathbf{x}_r; \omega) - \mathbf{d}_{obs}]' [\mathbf{d}(\mathbf{x}_s, \mathbf{x}_r; \omega) - \mathbf{d}_{obs}]. \end{aligned} \quad (2.13)$$

Its first derivative with respect to the model parameters $\mathbf{m}(\mathbf{x}, \mathbf{h})$ is

$$\begin{aligned} \frac{\partial S(\mathbf{m})}{\partial \mathbf{m}(\mathbf{x}, \mathbf{h})} &= \frac{1}{2} \sum_{\omega} \sum_{\mathbf{x}_s} \sum_{\mathbf{x}_r} \{ \mathbf{G}'(\mathbf{x} - \mathbf{h}, \mathbf{x}_r; \omega) \mathbf{G}'(\mathbf{x} + \mathbf{h}, \mathbf{x}_s; \omega) [\mathbf{d}(\mathbf{x}_s, \mathbf{x}_r; \omega) - \mathbf{d}_{obs}] \\ &\quad + [\mathbf{d}(\mathbf{x}_s, \mathbf{x}_r; \omega) - \mathbf{d}_{obs}]' \mathbf{G}(\mathbf{x} - \mathbf{h}, \mathbf{x}_r; \omega) \mathbf{G}(\mathbf{x} + \mathbf{h}, \mathbf{x}_s; \omega) \}, \end{aligned} \quad (2.14)$$

and the second derivative with respect to the model parameters $\mathbf{m}(\mathbf{x}, \mathbf{h})$ and $\mathbf{m}(\mathbf{x}', \mathbf{h}')$ of the objective function is the subsurface-offset Hessian:

$$\begin{aligned} \mathbf{H}(\mathbf{x}, \mathbf{h}; \mathbf{x}', \mathbf{h}') &= \frac{\partial^2 S(\mathbf{m})}{\partial \mathbf{m}(\mathbf{x}, \mathbf{h}) \partial \mathbf{m}(\mathbf{x}', \mathbf{h}')} \\ &= \sum_{\omega} \sum_{\mathbf{x}_s} \mathbf{G}'(\mathbf{x} - \mathbf{h}, \mathbf{x}_s; \omega) \mathbf{G}(\mathbf{x}' - \mathbf{h}', \mathbf{x}_s; \omega) \\ &\quad \sum_{\mathbf{x}_r} \mathbf{G}'(\mathbf{x} + \mathbf{h}, \mathbf{x}_r; \omega) \mathbf{G}(\mathbf{x}' + \mathbf{h}', \mathbf{x}_r; \omega). \end{aligned} \quad (2.15)$$

Compared to the result obtained in the previous section (equation 2.8), the model

space now contains the subsurface-offset dimension.

In appendix A, I show how to compute the Hessian in the reflection-angle and azimuth-angle dimensions from subsurface-offset Hessian. It requires application of a slant-stack operator that transforms the image from the subsurface-offset domain to the angle domain (Biondi and Tisserant, 2004).

Regularization in the prestack-image domain

In chapter 4, I show the numerical solution of equation 2.4 in the poststack image domain (zero subsurface offset). The conclusion from that experiment is that a damping regularization in the poststack image domain is not ideal, because it does not allow inclusion of prior information about the model to stabilize the inversion result. Having defined the Hessian in the prestack image domain in the previous subsection, we can generalize equation 2.4 to the prestack image domain.

Two different regularization schemes for wave-equation inversion have been discussed in the literature. First is the use of a weighted identity operator, as in equation 2.10, which is customary in many scientific applications (damping). The second is a *geophysical regularization*, which imposes smooth variation of the image in the offset ray-parameter dimension (which is equivalent to the reflection-angle dimension) (Prucha and Biondi, 2002; Kuhl and Sacchi, 2003; Clapp, 2005).

A third regularization can be designed in analogy to the work of Stolk and Symes (2002), and Shen et al. (2003), in nonlinear wave-equation inversion for velocity estimation. It is a differential semblance operator to penalize the energy in the image not focused at zero subsurface offset.

The prestack image-domain version of equation 2.4 with a general regularization can be stated as

$$(\mathbf{H}(\mathbf{x}, \mathbf{h}; \mathbf{x}', \mathbf{h}') + \varepsilon \mathbf{R}) \hat{\mathbf{m}}(\mathbf{x}, \mathbf{h}) - \mathbf{m}_{mig}(\mathbf{x}, \mathbf{h}) = \mathbf{r} \approx 0, \quad (2.16)$$

where $\mathbf{H}(\mathbf{x}, \mathbf{h}; \mathbf{x}', \mathbf{h}')$ is the subsurface-offset Hessian, \mathbf{R} is a linear regularization operator, $\mathbf{x} = (x, y, z)$ is a point in the image, $\mathbf{h} = (h_x, h_y, h_z)$ is the half subsurface offset, \mathbf{r} is the residuals vector, and ε is a scalar parameter that governs the strength of the regularization.

The first option for the regularization operator is a customary damping, given by

$$\mathbf{R} = \mathbf{I}, \quad (2.17)$$

where \mathbf{I} is the identity operator. However all the extra cost involved in expanding the dimensionality of equation 2.4 is justified when moving beyond damping.

The second option for regularization is a derivative in the reflection-angle (Prucha and Biondi, 2002; Kuhl and Sacchi, 2003; Clapp, 2005). That regularization operator smooths the amplitudes of the image in the reflection-angle dimension. It works by spreading the image from well-illuminated to poorly illuminated reflection angles.

The angle-domain regularization operator can be written as

$$\mathbf{R} = \mathbf{S}_{\Theta \rightarrow \mathbf{h}} \nabla_{\Theta}^2 \mathbf{S}_{\mathbf{h} \rightarrow \Theta}, \quad (2.18)$$

where $\mathbf{S}_{\Theta \rightarrow \mathbf{h}}$ is a slant-stack operator that transforms the image from angle to subsurface-offset domain, and $\mathbf{S}_{\mathbf{h} \rightarrow \Theta}$ is its adjoint that transform the image from the subsurface-offset domain to the angle domain. $\nabla_{\Theta}^2 = \frac{\partial^2}{\partial \gamma^2} + \frac{\partial^2}{\partial \theta^2}$ is a Laplacian operator, and $\Theta = (\gamma, \theta)$, where γ is the reflection angle, and θ is the azimuth angle.

The third regularization option is a differential semblance regularization operator, defined as

$$\mathbf{R} = \mathbf{P}_{\mathbf{h}}^2, \quad (2.19)$$

where $\mathbf{P}_{\mathbf{h}} = |\mathbf{h}|$ is the differential semblance operator (Shen et al., 2003). It penalizes the energy in the image not focused at zero subsurface offset.

Chapter 3

Structure and computation of the Hessian

INTRODUCTION

The main obstacle to doing imaging by inversion using seismic reflection data has been the cost involved in the numerical computation of the Hessian. As described in the previous chapter, several authors have approximated the Hessian as a diagonal matrix (Chavent and Plessix, 1999; Rickett, 2003; Plessix and Mulder, 2004), but as will be shown in chapters 4 and 5, this approximation does not yield an acceptable image when the subsurface is complex. Another approximation proposed by Hu et al. (2001) is to compute a horizontally invariant non-diagonal Hessian for $v(z)$ media. In almost every situation, this assumption also fails because, as I will show later, the Hessian changes with subsurface lateral position due to lateral variations in the velocity model and limitations on the acquisition geometry.

In this chapter I show how to compute a non-diagonal approximation of the Hessian matrix without making compromises about the complexity of the velocity model or the acquisition geometry. Three important properties of the Hessian matrix make this possible. The first is that the most energetic elements of the Hessian matrix are

located on and near the main diagonal. Thus, the time required for numerical computation can be reduced by more than an order of magnitude if only those terms are computed. The number of relevant elements away from the diagonal is related to the complexity of the overburden and the acquisition geometry. The second factor that helps to reduce the computational cost is the redundancy in seismic data acquisition. Sources and receiver positions are usually “revisited” while the data are acquired. Important properties of equation 2.8 can be exploited taking this fact into account. Depending on the acquisition geometry these properties can help to reduce the cost of the Hessian matrix computation by an order of magnitude or more. The third factor exploits the locality in space of the cross-correlations involved in equation 2.8. This property relaxes the required sampling of the frequency axis without wrap-around artifacts contaminating the off-diagonal terms of the Hessian matrix.

GEOPHYSICAL INTERPRETATION OF THE HESSIAN MATRIX

Spreading around the diagonal

The geophysical interpretation of the Hessian matrix can be easily grasped from equation 2.4. A unit-strength single-point reflectivity ($\hat{\mathbf{m}}$) at the scatterer point $\mathbf{x} = (x, y, z)$, when convolved with a row of the Hessian matrix, gives a blurred point centered at \mathbf{x} (\mathbf{m}_{mig}). In the engineering literature, the blur area is defined as the *Point Spread Function* (PSF) of the imaging system, and is directly related to the resolving power of the system.

The PSF of the seismic imaging system is non-stationary, because the amount of spread energy around each subsurface point changes as a consequence of the complexity of the velocity model and the acquisition geometry. Berkhout (1984) and Claerbout (1985, 2001) extensively discuss how the size of the PSF (the resolution) is related to seismic wavelength and the range of the illumination angle at a point diffractor. In the next subsections I illustrate some of these ideas with examples.

Constant-velocity model

Two main parameters control the seismic wavelength ($\lambda = \frac{v}{f}$): the acoustic velocity (v), and the frequency (f). For a given velocity, smaller frequencies have longer vertical wavelengths and thus lower resolution (and vice versa). In contrast, for a given frequency, the wavelength is proportional to the velocity. To illustrate how the wavelength and the range of illumination angles control the spreading of the energy away of the diagonal of the Hessian matrix, I created a series of numerical tests using two models with different but constant background velocity. In these tests the central frequency (5 Hz) and the frequency band (10 Hz) were kept constant. The recording geometry simulates a marine acquisition, where the boat shoots every 25 m from $x = 0.8$ km to $x = -0.8$ km, and pulls a receiver cable 1.6 km long with receiver spacing of 25 m.

Figure 3.1 shows the silhouette (envelope) of the nonzero elements, and Figure 3.2 shows a close-up of the Hessian matrix for a background velocity $v = 1.5$ km/s. Notice the banded nature of the matrix, with most of the energy in the main diagonal. The structure of the Hessian can be understood in terms of a convolution matrix being multiplied by a long vector the size of the model space (in 2-D $n_x \times n_z$). The "pulse-like" appearance of the diagonals is due to the way the model space is arranged. This model space organization is optional; I choose to have the z axis as the fast-changing dimension, in which case the width of the diagonal is the size of the PSF in the z direction. The number of diagonals is the size of the PSF in the x direction (only five are shown in 3.2).

The same acquisition geometry was used to compute the Hessian matrix shown in Figures 3.3 and 3.4 (close-up), but now for a background velocity of $v = 3$ km/s. Comparing Figures 3.1 and 3.3 we see that the spreading is broader in the one with higher background velocity. This result is to be expected since the size of the PSF is directly proportional to the wavelength and the wavelength is directly proportional to the velocity (Berkhout, 1984; Claerbout, 1985, 2001).

The Hessian matrix can be displayed in two different ways; by plotting the values

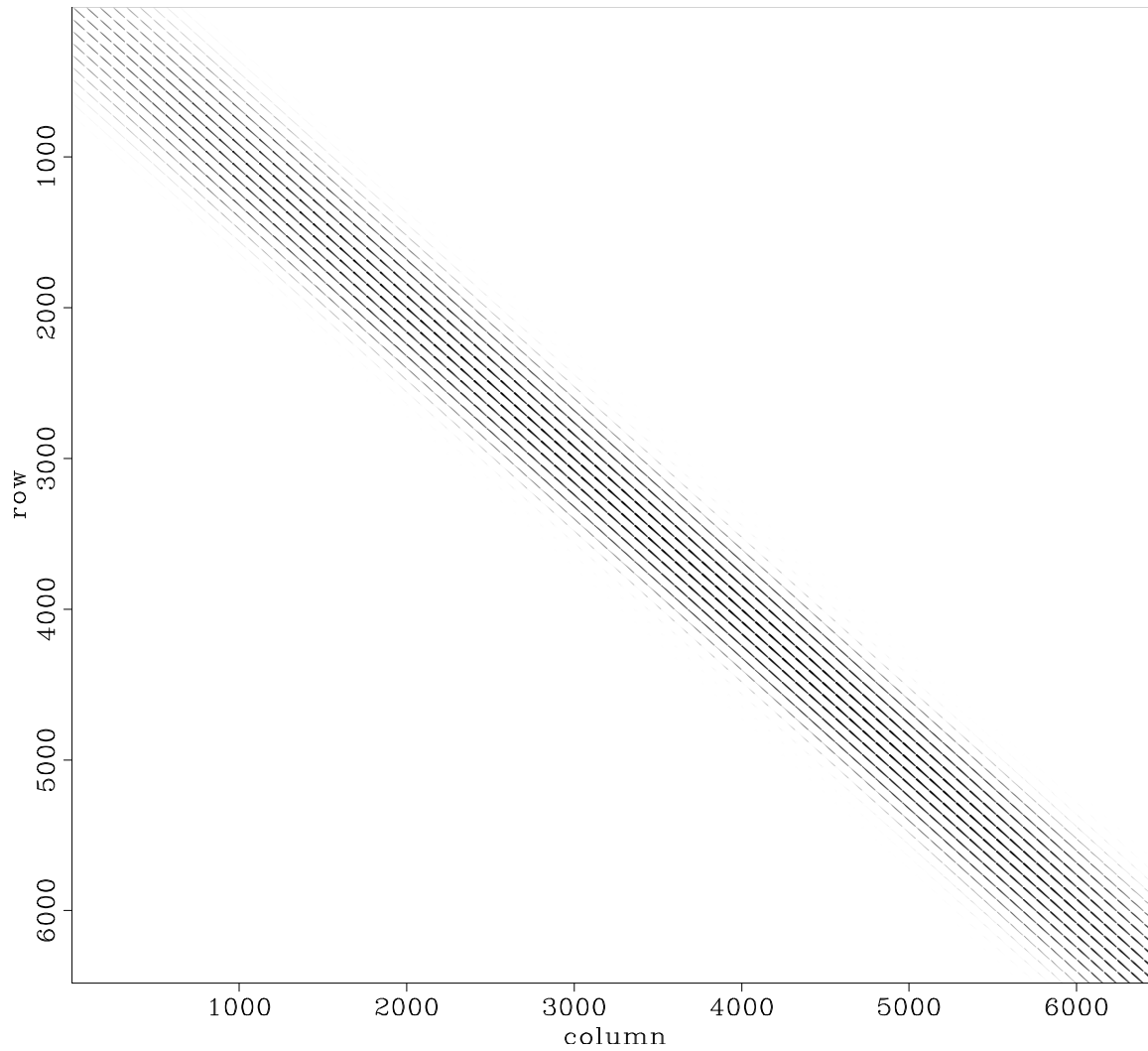


Figure 3.1: Silhouette of the nonzero elements of the Hessian matrix for a constant-velocity model with $v = 1.5$ km/s. The acquisition geometry contains all shots in the survey. `Target-Hessian/. hmatrix-const-new`

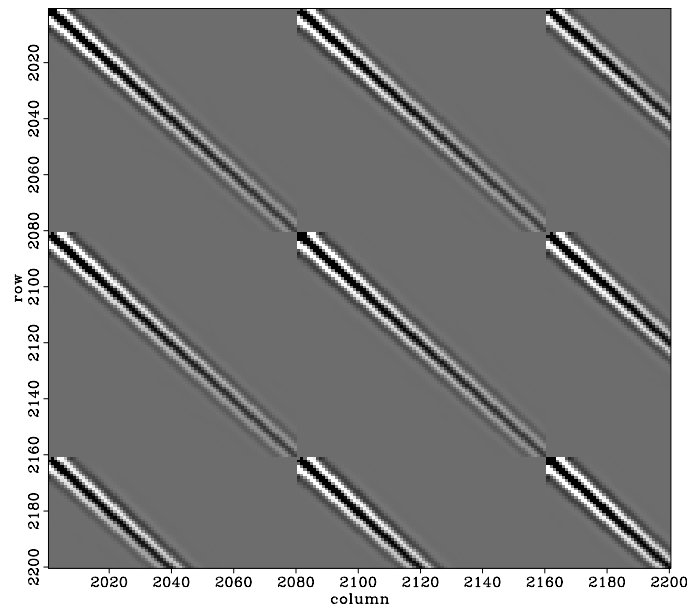


Figure 3.2: Close-up of the Hessian matrix from Figure 3.1 for a constant-velocity model with $v = 1.5$ km/s. The acquisition geometry contains all shots in the survey.

Target-Hessian/. hmatrix-const-new-co

at each row and column in a scatter plot (as in Figure 3.1), or by convolving it with a set of point scatterers in model space $\mathbf{x} = (x, y, z)$ (as in Figure 3.6). The first is good for getting a global idea of the structure of the Hessian matrix, and the second is better for understanding the spreading at each individual point of the model space. In the following, I show the convolution of different Hessian matrices with the four point-scatterers model shown in Figure 3.5.

Figure 3.6 shows the convolution of the Hessian matrix for the constant-velocity model, $v = 1.5$ km/s (Figure 3.1), with the four-scatterer model (Figure 3.5). Figure 3.7 shows the convolution of the Hessian matrix of the constant-velocity model $v = 3$ km/s (Figure 3.3) with the four-scatterer model (Figure 3.5). The spreading is broader in the example with the higher background velocity, as we observed in Figures 3.1 and 3.3.

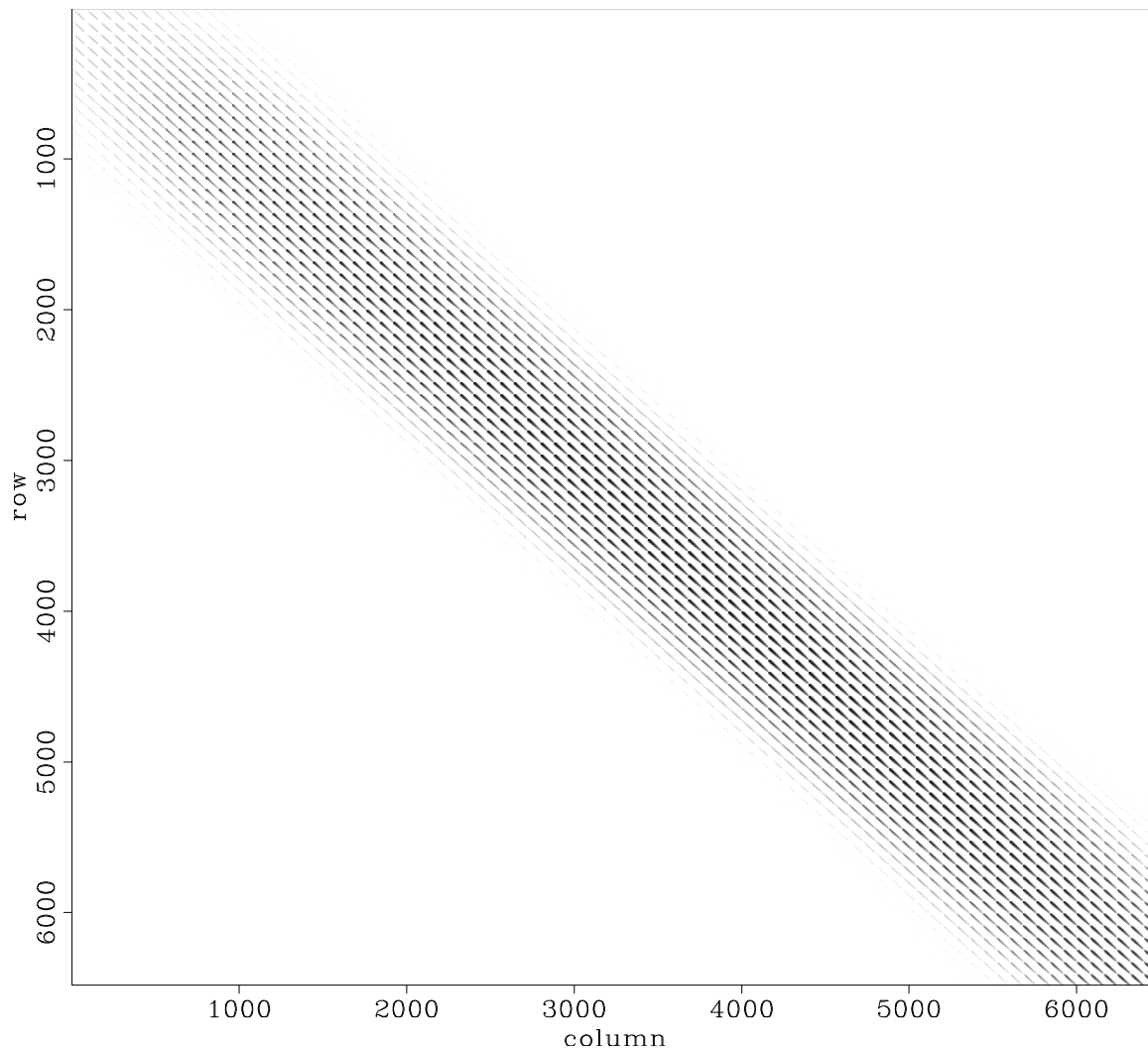


Figure 3.3: Silhouette of the nonzero elements of the Hessian matrix for a constant-velocity model with $v = 3$ km/s. The acquisition geometry contains all shots in the survey. `Target-Hessian/. hmatrix-const1-new`

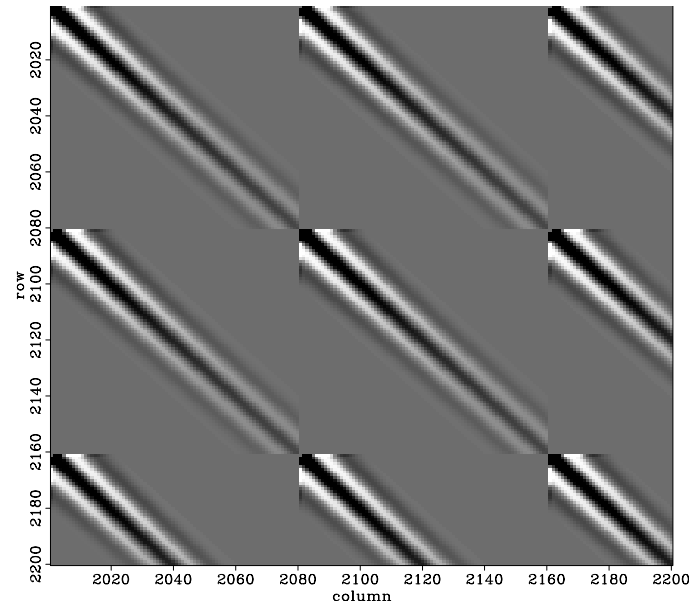


Figure 3.4: Close-up of the Hessian matrix from Figure 3.3 for a constant-velocity model with $v = 3$ km/s. The acquisition geometry contains all shots in the survey.

Target-Hessian/. hmatrix-const1-new-co

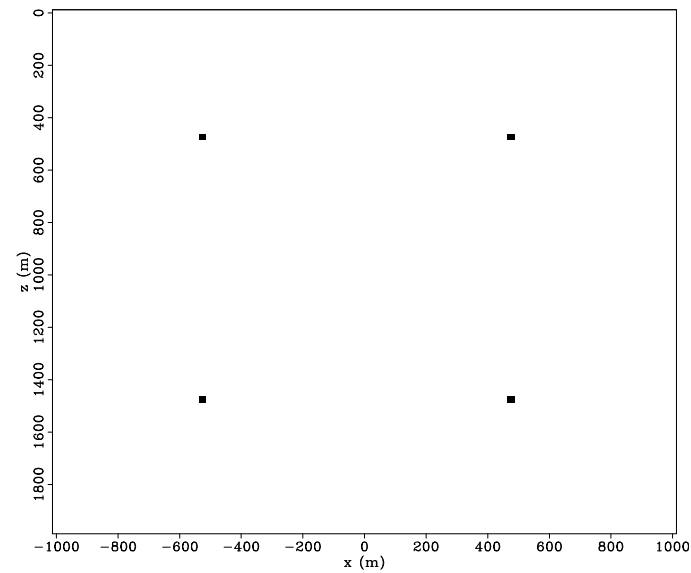


Figure 3.5: Four scatterers distributed around the model space.

Target-Hessian/. scatt

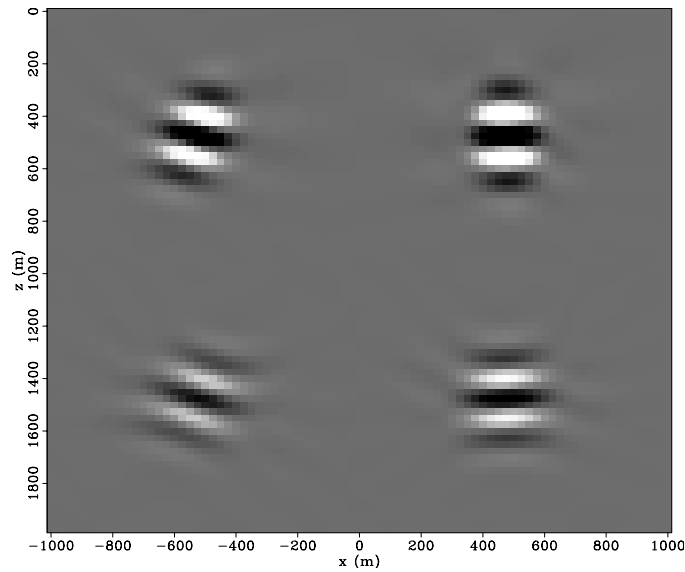


Figure 3.6: Convolution of the Hessian matrix of the constant-velocity model $v = 1.5$ km/s (Figure 3.1) with the four-scatterer model (Figure 3.5). The acquisition geometry contains all shots in the survey. `Target-Hessian/. conv-const`

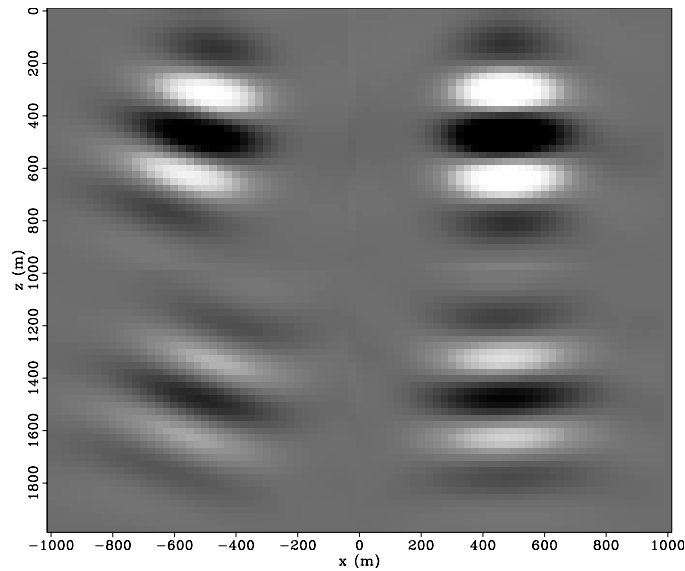


Figure 3.7: Convolution of the Hessian matrix of the constant-velocity model $v = 3$ km/s (Figure 3.3) with the four-scatterer model (Figure 3.5). The acquisition geometry contains all shots in the survey. Compare with Figure 3.6, which uses a Hessian computed with a lower velocity. `Target-Hessian/. conv-const1`

As seen in Figures 3.6 and 3.7, in a constant-velocity model the amount of spreading increases with depth. This is easy to understand in terms of ray theory. As the depth increases, the diffractors are “illuminated” by a smaller range of aperture angles. Rays that reflect at far angles from deeper targets are not recorded, because of the limited offset present in seismic acquisition. The smaller the range of illuminating angles, the broader the PSF (Berkhout, 1984).

After convolution, we see the directional character of the PSF, which has variable spreading depending on the illumination at each point of the model space (Figure 3.6). The direction with maximum spreading is the low-resolution axis, and its perpendicular is the high-resolution axis. Gelius et al. (2002) present a detailed discussion of an alternative way for analyzing the directionality the PSF in the Fourier domain. Figure 3.8 shows the local 2-D Fourier transforms of the PSF of the constant-velocity model $v = 1.5$ km/s (shown in Figure 3.6). The dark regions represent all the wave-numbers that “illuminate” the point scatterer. The size of each region and its dominant scattering direction depends on the frequency content, the background velocity, and the survey geometry. The dominant scattering direction coincides with the high-resolution direction of the PSF.

To further illustrate the influence of illumination and the limited geometry on the Hessian matrix, I computed the Hessian matrix corresponding to a background velocity $v = 1.5$ km/s, but with only one shot located at $x = 0$ km (Figures 3.9, 3.10, and 3.11). Note how much the energy and distribution of the nonzero elements of the matrix change in Figure 3.9 compared to Figure 3.1. Also note the “smiles” in Figure 3.11 that are absent in Figure 3.6, which has a wider aperture of shots. As more shots are included in the computation of the Hessian, the smiles are reduced, as understood in terms of the principle of stationary phase (as is shown Figure 3.6).

In a more realistic subsurface scenario, more factors influence the PSF, since seismic waves can be refracted, diffracted, converted, and attenuated as they travel through the earth. As a rule of thumb, the deeper the target, the broader the PSF, because the combined influences of increasing velocity and attenuation of higher frequencies make the wavelength increase, and the limited acquisition geometry restricts

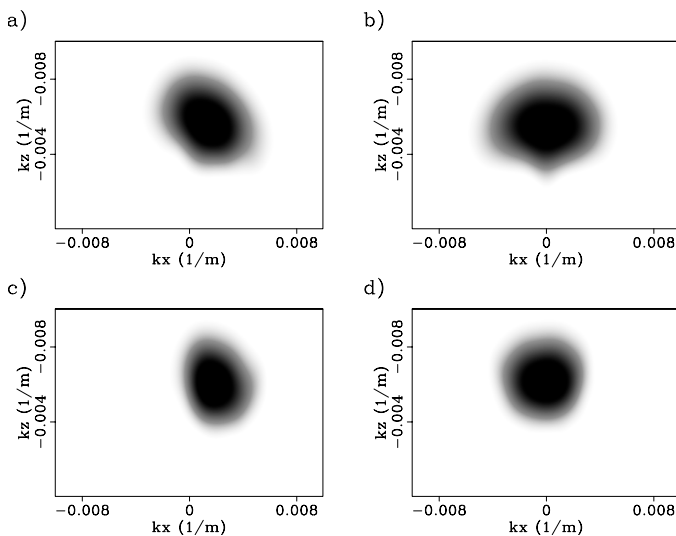


Figure 3.8: Spatial Fourier transform of the convolution of the Hessian matrix of the constant-velocity model $v = 1.5$ km/s (Figure 3.6), with the four-scatterer model (Figure 3.5). The acquisition geometry contains all shots in the survey. Note the different spectral coverage in the (k_x, k_z) plane at each scatterer location.

Target-Hessian/. conv-const-kzkx

the illumination-angle range. Thus the Hessian matrix will be less diagonal dominant.

THE HESSIAN MATRIX IN A COMPLEX AREA

In this section I demonstrate, by using the Sigsbee2B model, the main point of this thesis: that an approximation that does not consider the complexity of wave propagation is insufficient to characterize the PSF of the seismic imaging system in complex areas.

This is not to imply that there are no approximations in my approach, since for efficiency the Green's functions in equations 2.11, 2.5, and 2.8 are computed by means of a one-way wave-equation extrapolator. No upgoing energy is modeled, because the evanescent energy is usually damped (Claerbout, 1985). This makes the one-way propagator act as a dip filter, depending on the velocity model (from the dispersion relation, $\frac{\omega^2}{v^2} < \mathbf{k}^2$). Also, the conventional one-way wave-equation does not model

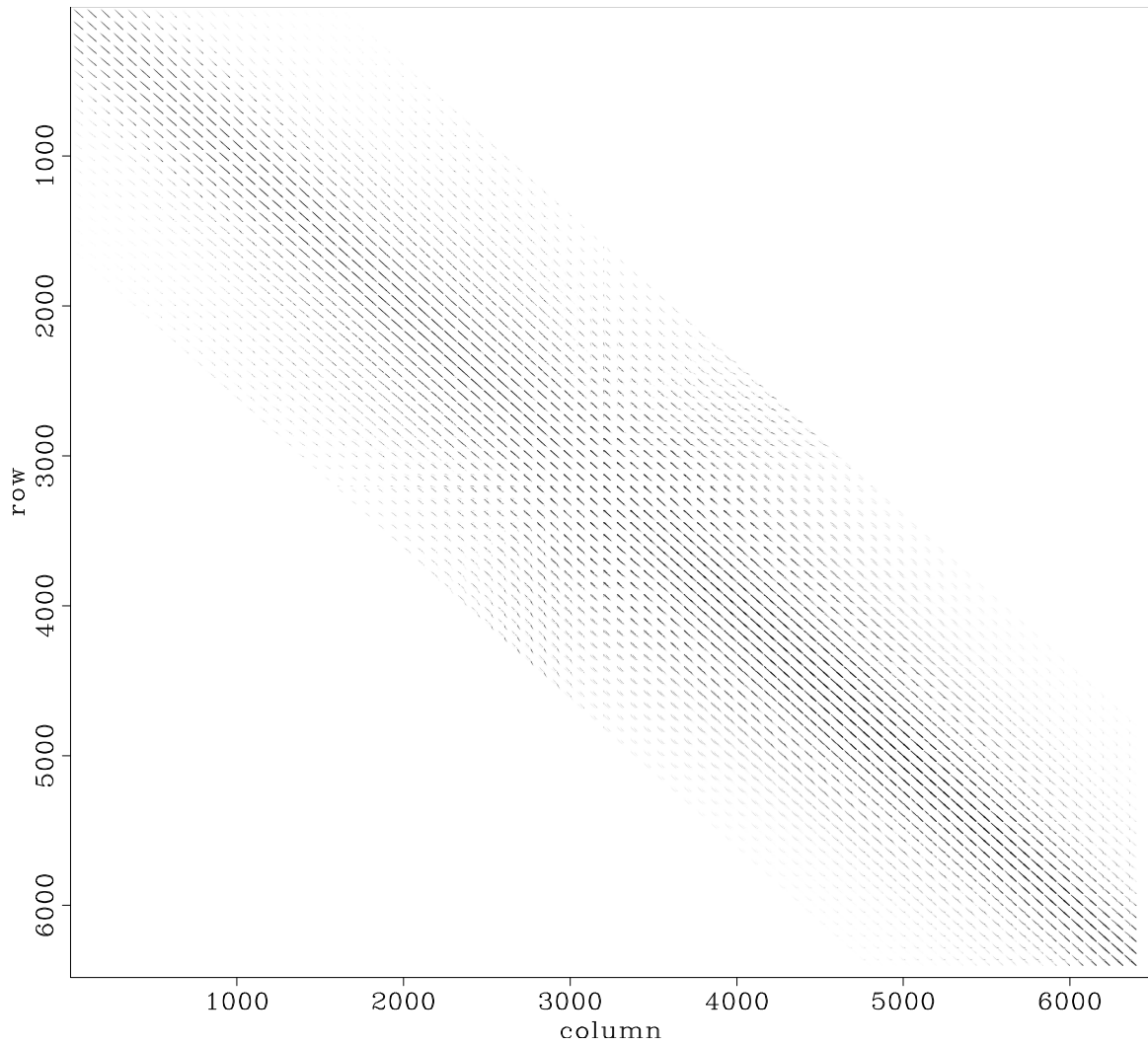


Figure 3.9: Silhouette of the nonzero elements of the Hessian matrix for the constant-velocity model $v = 1.5$ km/s . The acquisition geometry contains only one shot positioned at $x = 0$ km. `Target-Hessian/. hmatrix-const-new-1s`

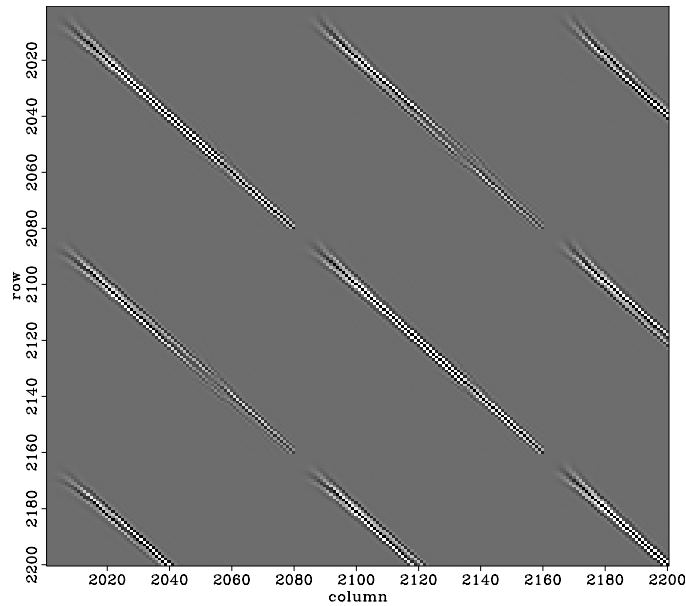


Figure 3.10: Close-up of the Figure 3.9 Hessian matrix of the constant-velocity model $v = 1.5$ km/s. The acquisition geometry contains only one shot positioned at $x = 0$ km. `Target-Hessian/. hmatrix-const-new-co-1s`

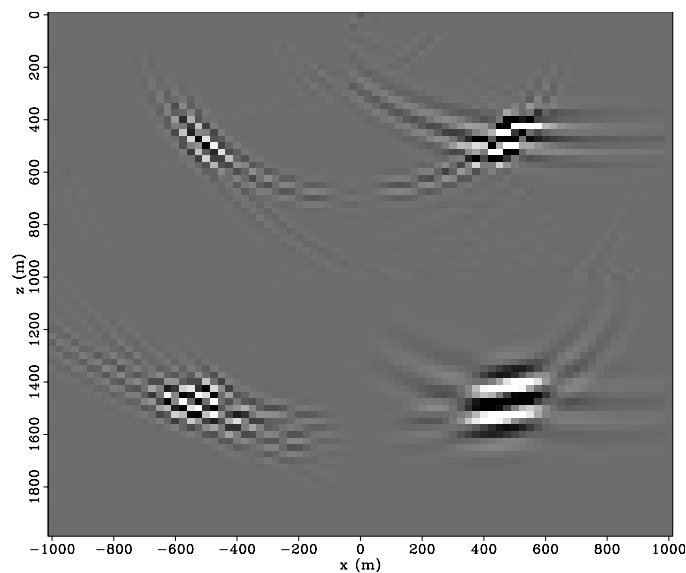


Figure 3.11: Convolution of the Hessian matrix of the constant-velocity model $v = 1.5$ km/s (Figure 3.9), with the four-scatterer model (Figure 3.5). The acquisition geometry contains only one shot positioned at $x = 0$ km. `Target-Hessian/. conv-const-1s-0`

accurately the the amplitude behavior with the angle of propagation (Zhang et al., 2005). Another problem arises when the velocity varies laterally, in which case it is difficult to accurately model energy that propagates close to 90° .

The previous limitations of one-way modeling can be mitigated by a sophisticated implementation of the extrapolator. The dip-filter effect should be reduced by including the Jacobian of the change of variable from ω to k_z (Sava et al., 2001), thus making \mathbf{L} closer to unitary. To properly model the amplitude behavior with the angle of propagation, Zhang et al. (2005) proposed using a modified one-way wave-equation whose solution matches the Kirchhoff inversion. The effect caused by the lateral variation of the velocity can also be mitigated by using better approximations of the square-root operator.

For the examples presented in this thesis, I used the one-way wave equation (Claerbout, 1985). I did not include the Jacobian, and I approximated the square root-operator with split-step Fourier plus interpolation (PSPI).

The Sigsbee2B model

The Sigsbee2B model simulates the geological setting found on the Sigsbee escarpment in the deep-water Gulf of Mexico (Paffenholz et al., 2002). The model exhibits illumination problems because of the complex salt shape, with a rugose salt top (Figure 3.12), found in this area. I choose a target zone (indicated with the “target” box in Figure 3.12) to see the influence of illumination on the Hessian close to the salt.

The target zone contains 50673 model points ($nx = 133$, $nz = 381$), too many to show the scatter plot of the Hessian matrix for the Sigsbee2B model without the display being aliased. To avoid display alias, I choose a smaller target that has 6650 points (only for the purpose of Figure 3.13). Figure 3.13 shows the silhouette (envelope) of the nonzero elements, and Figure 3.14 shows a close-up of the Hessian matrix for the Sigsbee2B model. Note the banded nature of the matrix, with more of the energy confined near the main diagonal. The energy decreases considerably in some areas of the matrix as the result of illumination problems created by the salt

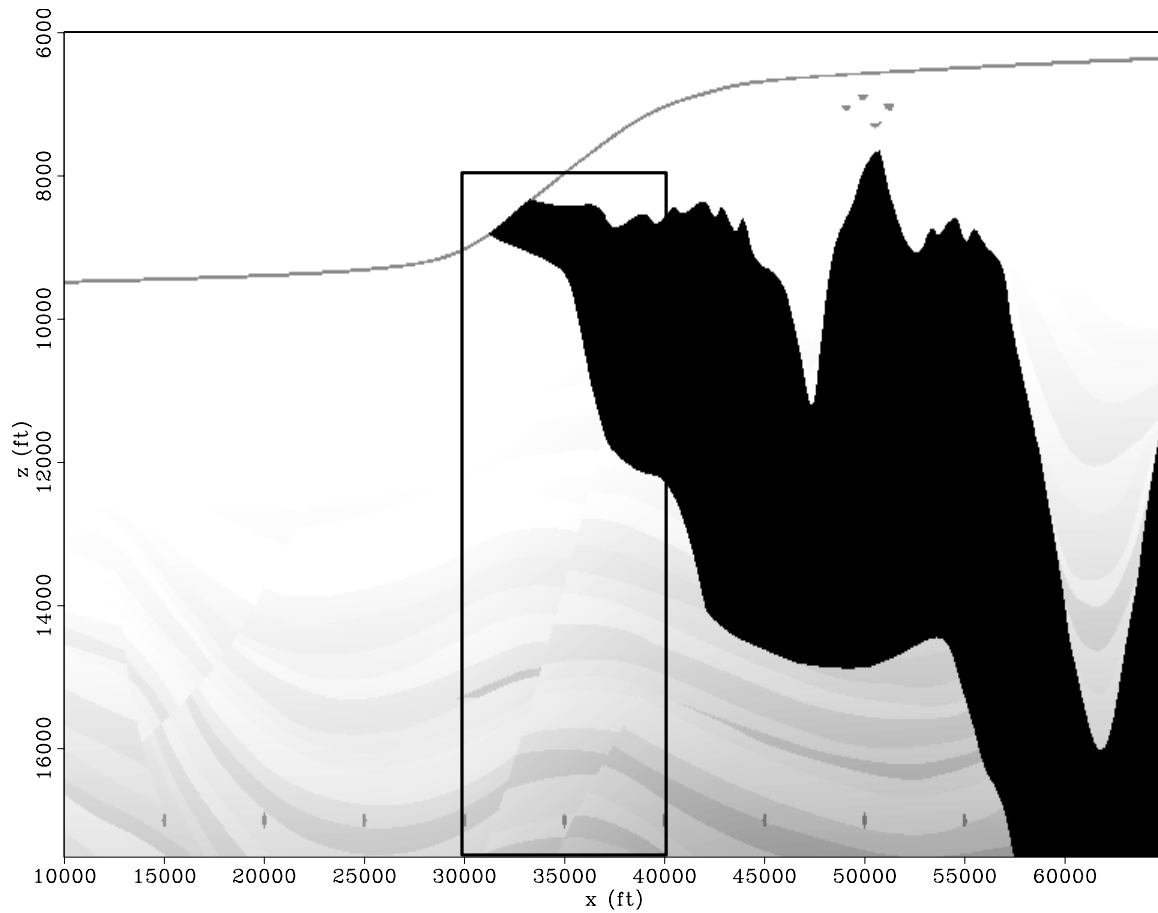


Figure 3.12: Sigsbee2B stratigraphic velocity model; target zone indicated with the “target” box. `Target-Hessian/. Sis-vel`

body.

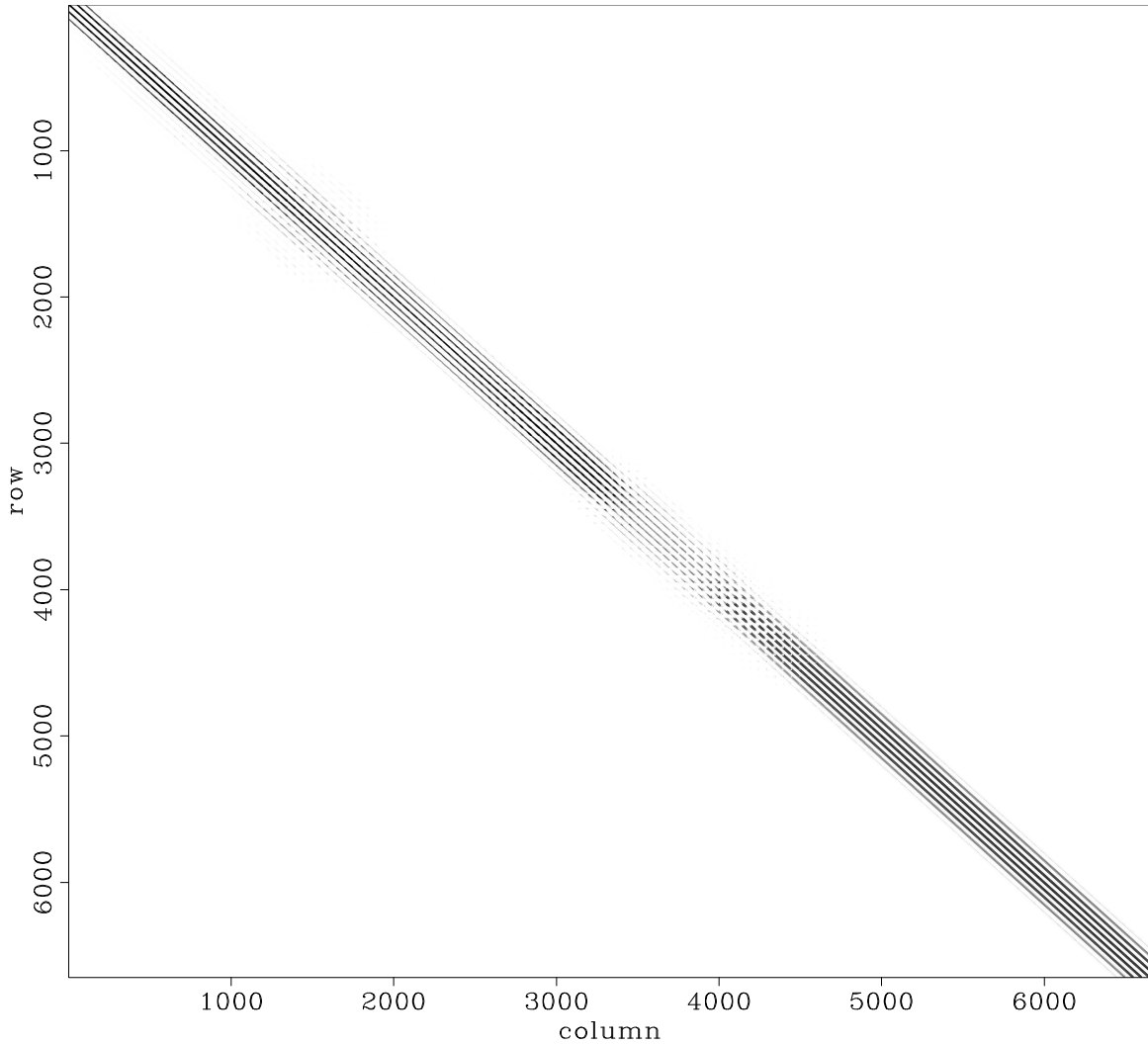


Figure 3.13: Silhouette of the nonzero elements of the Hessian matrix of the Sigsbee2B velocity model (6650-point target). `Target-Hessian/. hmatrix-Sis-new`

A good representation of the complexity of the focusing and defocusing of the seismic energy in this model is given by Figure 3.15, which shows just the main diagonal of the Hessian matrix across the target zone. Light grays correspond to high amplitudes, and dark grays to low amplitudes. Notice how the concave and convex shapes of the base of the salt respectively focus and defocus the seismic energy as waves propagate through the medium.

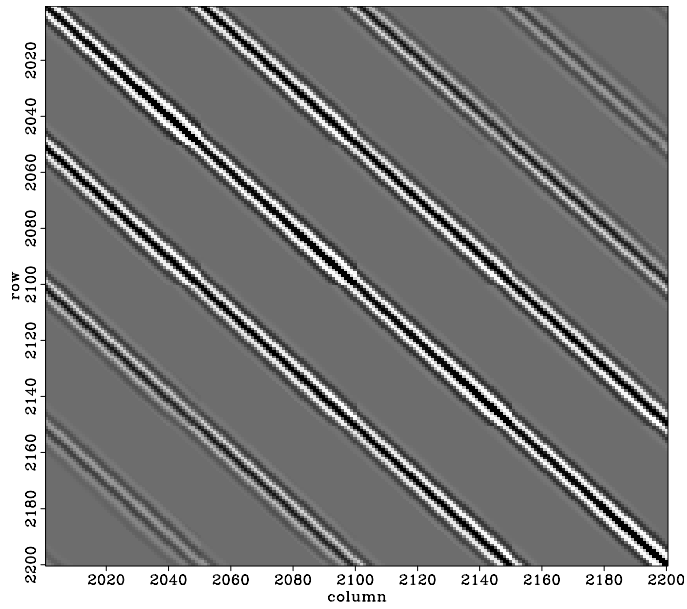


Figure 3.14: Close-up of Figure 3.13. Hessian matrix of the Sigsbee2B model.

`Target-Hessian/. hmatrix-Sis-new-co`

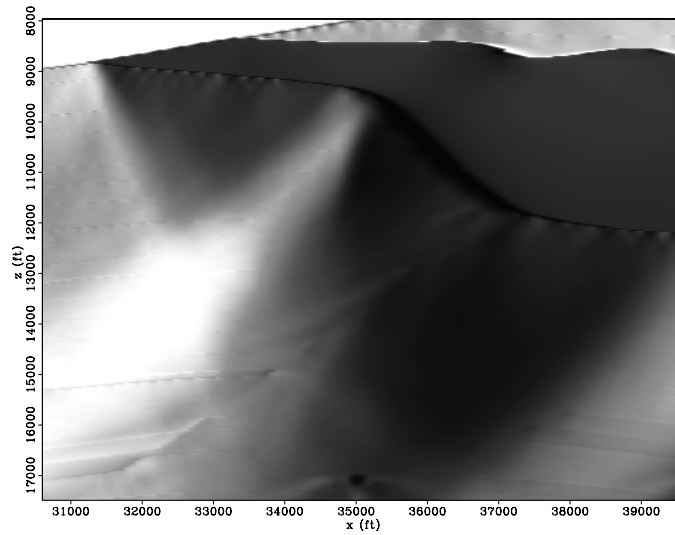


Figure 3.15: Diagonal of the Hessian matrix of the Sigsbee2B model.

`Target-Hessian/. diag-Sis`

I created a model with 32 point scatterers and convolved it with the Hessian matrix for the Sigsbee2B model (50673 model points), to see the influence of the presence of the salt body on the PSF. Figures 3.16 and 3.17 show the PSF and the envelope of the PSF, respectively. The envelope of the PSF (Figure 3.17) shows clearly the non-stationarity of the spread of the energy due to the salt body.

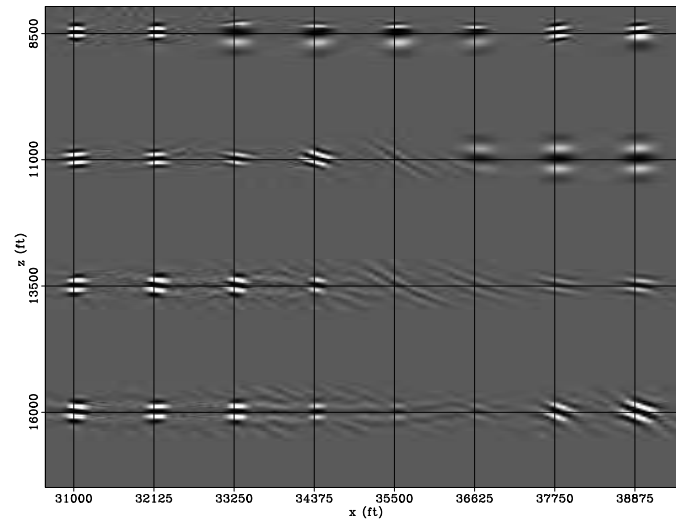


Figure 3.16: Convolution of the 32 point scatterers model with the Hessian matrix of the Sigsbee2B model in the target area. The non-stationarity of the PSF is evident.

Target-Hessian/. conv-Sis-new

In the well-illuminated zones, the PSF is confined to an small area centered on the scatter point, as seen for points located in the sediments to the left of the salt body, such as the point with coordinates $\mathbf{x} = (31000, 8500)$. As the point scatterers enter a shadow zone, the ellipses in the envelope display lose energy and spread away from the center of the position of the scatterers. A diagonal-matrix approximation of the Hessian would not be appropriate to describe this behavior, since there is considerable energy away from the center of the ellipse. The point scatterer with coordinates $\mathbf{x} = (35500, 13500)$ is a good example. As the point scatterer go out of the shadow zone, the PSF gains energy and focuses around the scatterer [$\mathbf{x} = (38875, 13500)$]. Another area of interest is inside the salt [$\mathbf{x} = (38875, 11000)$], where the PSF expands as the result of the salt's higher velocity.

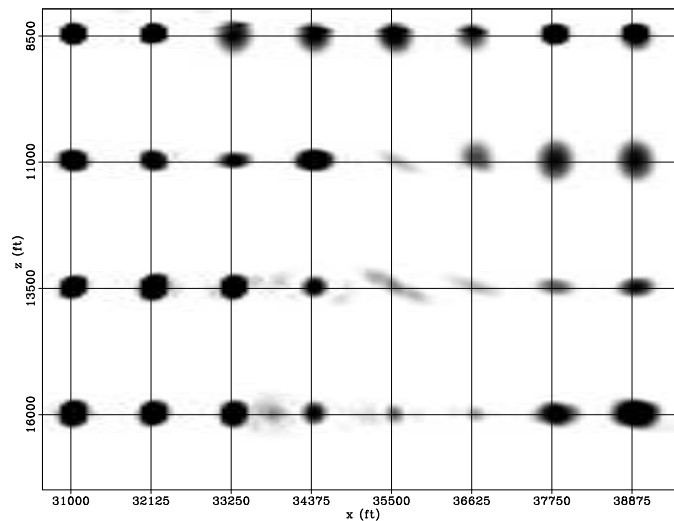


Figure 3.17: Envelope of the convolution of the 32 point scatterers model with the Hessian matrix of the Sigsbee2B model in the target area. The non-stationarity of the PSF is evident. `Target-Hessian/. conv-env-Sis-new`

I computed the local Fourier transform at each point scatterer (Figure 3.18). The relative differences in spectral coverage in the (k_x, k_z) plane are evident. The points located in the sediments with no influence of the salt body present full spectral coverage, as illustrated by the point with coordinates $\mathbf{x} = (31000, 8500)$. In contrast, the point scatterers in the shadow zone have a limited spectral coverage, as illustrated by the point with coordinates $\mathbf{x} = (38875, 13500)$. At this position, the dominant scattering direction is evident. This point is illuminated with a narrow range of angles from the right side of the model with waves propagating through the salt body. Note how the spectral coverage of the points inside the salt [$\mathbf{x} = (38875, 11000)$] reduces with respect to the points outside the salt, as a consequence of the salt's higher velocity.

The subsurface-offset Hessian

Figure 3.19 shows the main diagonal of the subsurface-offset Hessian matrix across the target zone. Light grays correspond to high amplitudes, and dark grays to low

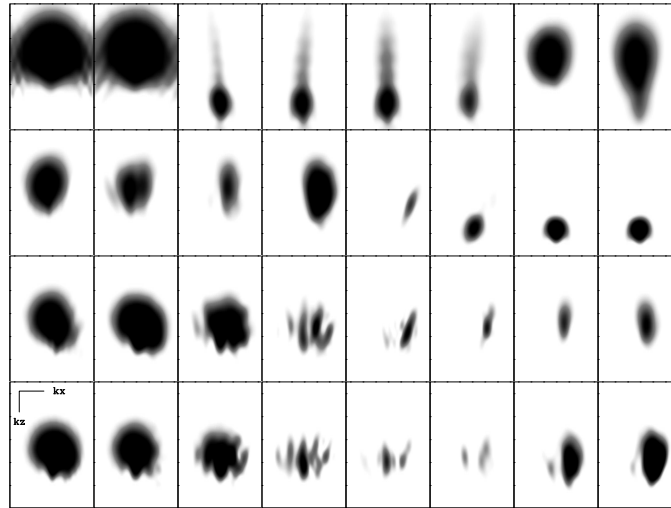


Figure 3.18: Spatial Fourier transform of the convolution of the 32 point scatterers model with the Hessian matrix of the Sigsbee2B model in the target area. Note the relative differences in spectral coverage in the (k_x, k_z) plane at each scatterer location.

Target-Hessian/. conv-Sis-kzkx

amplitudes. The front panel shows the zero-subsurface-offset (same as Figure 3.15), and the side panel shows the subsurface-offset gather at $x = 32300$ ft. The values in the diagonal change smoothly in the subsurface-offset dimension.

The convolution of the subsurface-offset Hessian with the model of the 32 scatterers is shown in Figure 3.20. The front panel shows the zero-subsurface-offset PSF (same as Figure 3.16), and the side panel shows the PSF in the subsurface-offset dimension at $x = 35500$ ft. In the subsurface-offset dimension, the energy spreads in a slanted line close to the horizontal.

The PSF in the subsurface-offset can be transformed into the reflection-angle domain by slant stacking (Sava and Fomel, 2003) (Figure 3.21). The front panel shows a constant-angle section (at 18°), and the side panel shows the reflection-angle gather at $x = 35550$ ft. After the offset-to-angle transformation, the slanted lines in the offset gathers transform into a narrow reflection-angle range. This result is consistent with the one obtained in the Fourier domain (Figure 3.18).

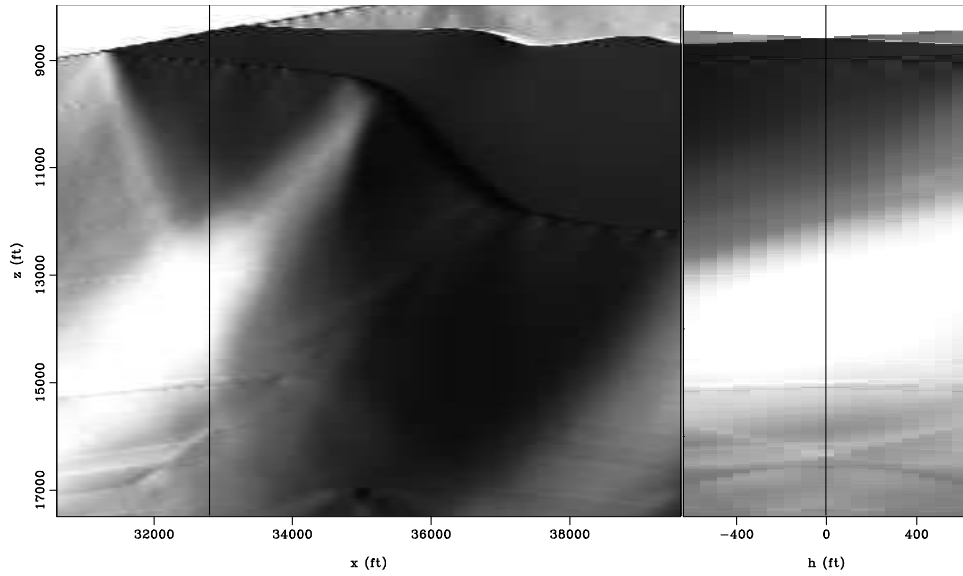


Figure 3.19: Diagonal of the subsurface-offset Hessian matrix of the Sigsbee2B model.
 Target-Hessian/. diag-Sis-off

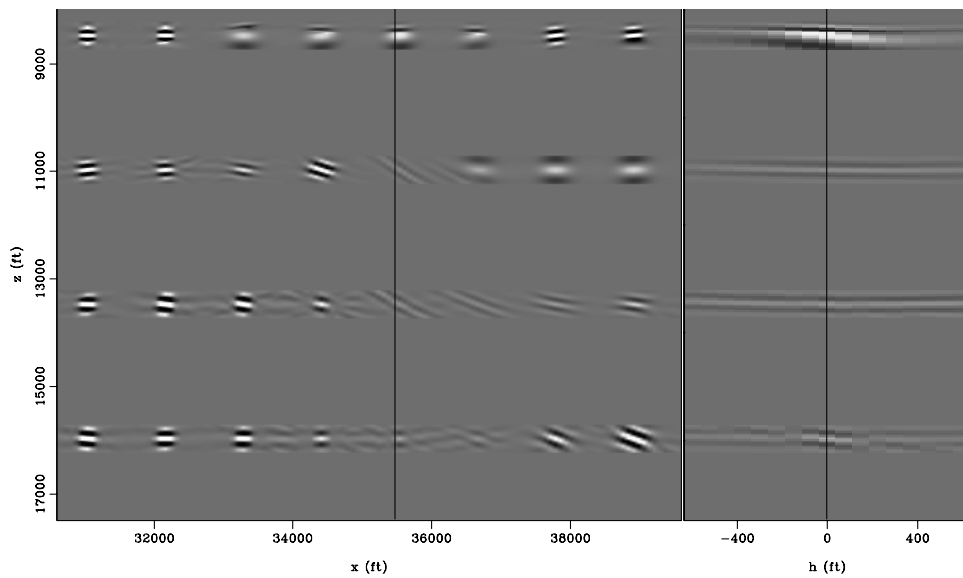


Figure 3.20: Convolution of the 32-point-scatterer model with the Hessian matrix of the Sigsbee2B model in the subsurface-offset domain. The non-stationarity of the PSF is evident.
 Target-Hessian/. conv-Sis-off

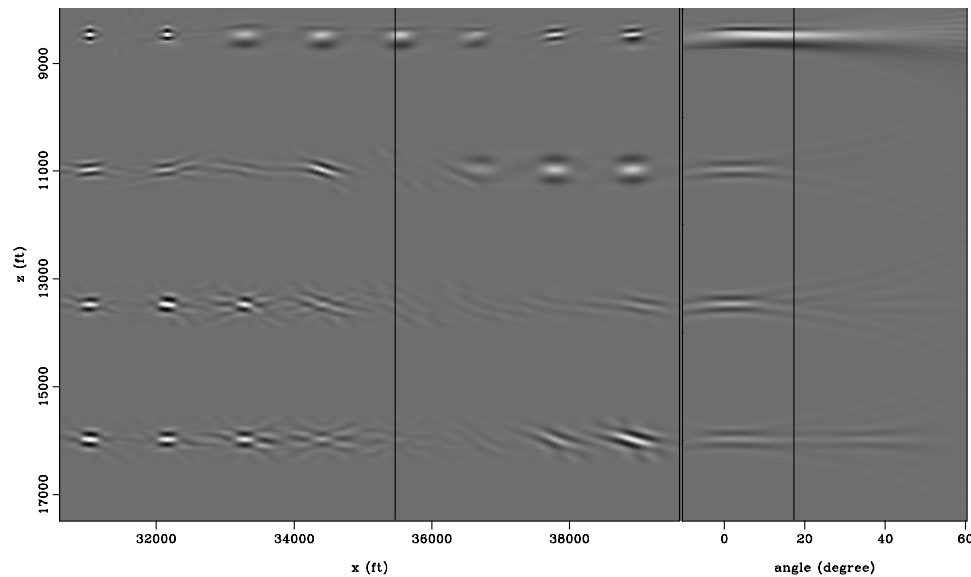


Figure 3.21: Convolution of the 32 point scatters model with the Hessian matrix of the Sigsbee2B model in the reflection-angle domain. The non-stationarity of the PSF is evident. `Target-Hessian/. conv-Sis-ang`

EXPLICIT NUMERICAL COMPUTATION OF THE HESSIAN

A direct numerical implementation of the zero-subsurface-offset Hessian computation (equation 2.8) or of the more general subsurface-offset Hessian (equation 2.15) is too expensive for today's most advanced computers, even for a small target. To "populate" the Hessian matrix in 3-D we would need to use 11 nested do loops for equation 2.8 (six in the model space and five in the data space) or 15 nested do loops for equation 2.15 (ten in the model space and five in the data space).

Algorithm 1 shows a simplified pseudo-code for numerical implementation of equation 2.15, where n_ω is the number of samples in the frequency dimension present in the seismic data, $(n_x, n_y, n_z, n_{hx}, n_{hy})$ is the number of samples in the model space (x, y, z, h_x, h_y) , (n_{sx}, n_{sy}) is the number of shots, and (n_{rx}, n_{ry}) is the number of their corresponding receivers. The indexes ix, iy, iz, ihx, ihy and $ix', iy', iz', ihx', ihy'$ run through the model space, and the indexes isx, isy, irx, iry run through the source and

Algorithm 1 Direct numerical implementation of the computation of the full Hessian in the subsurface-offset domain (equation 2.15).

```

for all frequencies  $n_\omega$  do
  read green
  for all model space  $(n_x, n_y, n_z, n_{hx}, n_{hy})$  do
    for all model space  $(n_x, n_y, n_z, n_{hx}, n_{hy})$  do
      for all shot positions  $(n_{sx}, n_{sy})$  do
        for all receiver positions  $(n_{rx}, n_{ry})$  do
          Sum2(isx,isy)=green(ix,iy,iz,irx,iry)*green(ix',ix',iz',irx,iry)
        end for
        H(ix,iy,iz,ihx,ihy,ix',iy',iz',ihx',ihy')=H(ix,iy,iz,ihx,ihy,ix',iy',iz',ihx',ihy')
        + green(ix,iy,iz,isx,isy)*green(ix',ix',iz',isx,isy)*Sum2(isx,isy)
      end for
    end for
  end for
end for

```

receiver positions. In general each shot has a different corresponding receiver position; that is why the accumulation Sum2 is performed inside the shots loop.

It is also important to take into consideration the memory requirements of the computations in equations 2.8 and 2.15, since the amount of RAM (Random Access Memory) necessary to avoid reading the Green functions from a hard disk could be large. I discuss later how the acquisition geometry might allow simplifications that yield reduced memory requirements.

Savings resulting from the sparsity and structure of the Hessian matrix

The main contributions of the Hessian occur on and near the diagonal (Figures 3.1, 3.3, 3.9, and 3.13), since otherwise the migration would spread energy throughout the model space (Figures 3.6, 3.7, 3.11, and 3.16). This means that instead of evaluating equation 2.8 or equation 2.15 for all \mathbf{x}' and all \mathbf{h}' , we could evaluate them at $\mathbf{x} + \mathbf{a}_x$ and $\mathbf{h} + \mathbf{a}_h$.

from the diagonal is related to the dominant wavelength (velocity, depth, and frequency) and the illumination (acquisition geometry and complexity of the overburden). All these acquisition and model parameters can vary throughout the model space in a way that is not easy to predict, making it difficult to make a prior estimate of the optimal distance from the diagonal. In this thesis, I use trial and error method to estimate the distance to use. Since this number has a direct impact on the cost of the Hessian matrix computation, it should be a subject of future research.

Savings related to the acquisition geometry

The redundancy of the seismic data acquisition allows for further computational cost savings. Depending of the acquisition geometry, source and receiver positions are usually “revisited” while the data is acquired.

A favorable case is the Ocean Bottom Cable (OBC) acquisition geometry, in which a group of receiver cables (patch) is laid down on the ocean bottom. The position of the patch is kept fixed while the boat shoots on the surface. Figure 3.22 shows a sketch of OBC acquisition; the gray color corresponds to a boat in one position, and the black color corresponds to the boat in a different position. The rectangle shows where receiver positions coincide for the two shots. This acquisition geometry makes the second sum in equation 2.8 constant for all the shot positions, allowing the removal of the receiver loop from the shot loop in algorithm 2 (algorithm 3).

A less favorable case is that of towed-streamers marine acquisition, since the geophones occupy different positions as the boat sails. Still, this acquisition allows for computational savings because from one shot to the next most of the receiver positions are revisited, leaving some geophones at the beginning of the cable and some at the end not coincident. Figure 3.23 shows a sketch of the towed-streamers marine geometry; the gray color corresponds to the first shot (top), and the black color corresponds to the shot in the next position (middle). The bottom sketch shows the two shots as they would occur in the the real experiment; the black rectangle shows where the receiver positions coincide for the two shots.

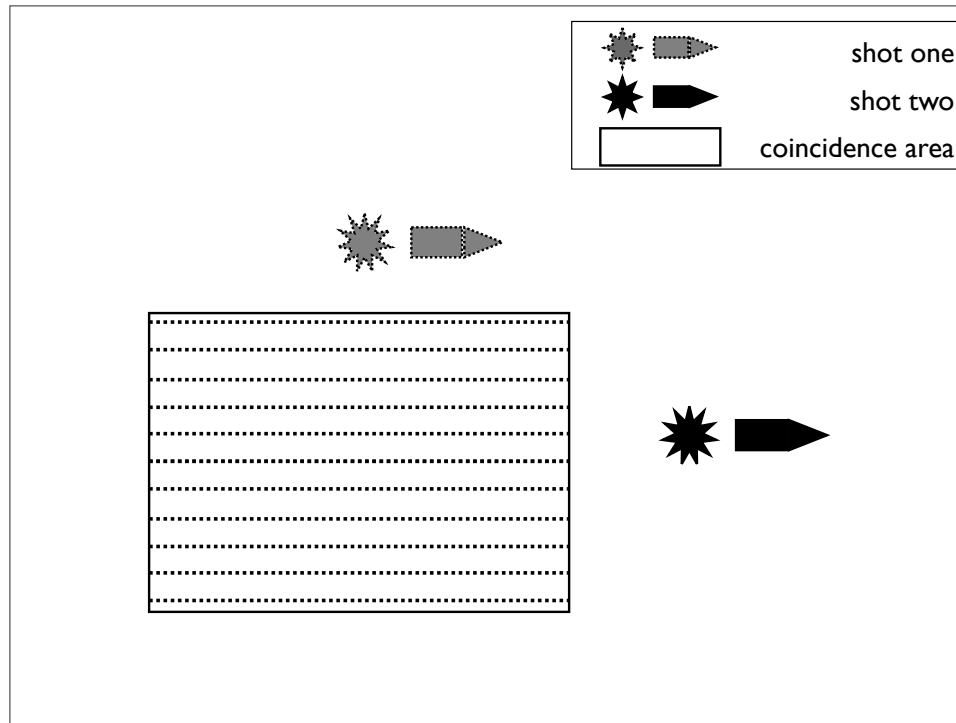


Figure 3.22: Sketch of the OBC acquisition, the gray boat shows a boat in one position, the black boat shows the boat in a different position. The rectangle shows where the receiver positions coincide for the two shots. Target-Hessian/. obc

Algorithm 3 Numerical implementation of the computation of the sparse Hessian in the subsurface-offset domain (equation 3.1) for an OBC-like acquisition. Notice that the receiver loop is outside the shot loops.

```

for all frequencies  $n_\omega$  do
  read green
  for all model space  $(n_x, n_y, n_z, n_{hx}, n_{hy})$  do
    for all model points around  $(x, y, z, h_x, h_y)$   $(na_x, na_y, na_z, na_{hx}, na_{hy})$  do
      for all receiver positions  $(n_{rx}, n_{ry})$  do
        Sum2=Sum2+green(...,irx,iry)*green(...,irx,iry)
      end for
      for all shot positions  $(n_{sx}, n_{sy})$  do
        H(ix,iy,iz,ihx,ihy,iax,iay,iaz,iahx,iahy)=H(ix,iy,iz,ihx,ihy,iax,iay,iaz,iahx,iahy)
        + green(...,isx,isy)*green(...,isx,isy)*Sum2
      end for
    end for
  end for
end for

```

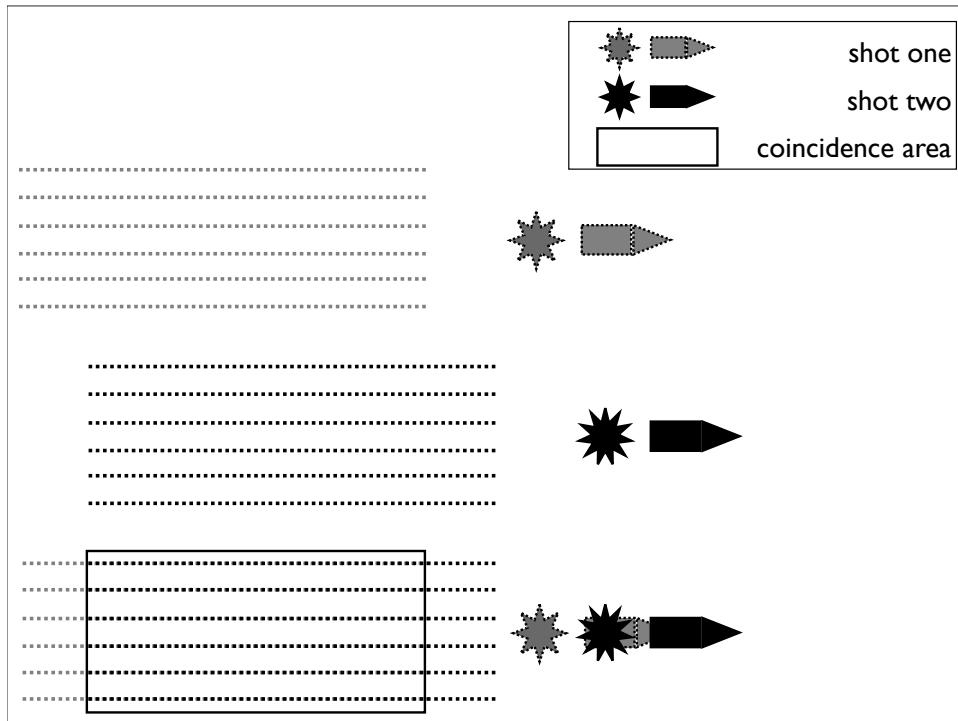


Figure 3.23: Sketch of the towed-streamers marine geometry; the gray color correspond to the first shot (top), and the black color corresponds to the shot in the next position (middle). The bottom sketch shows the two shots as they would occur in the the real experiment; the black rectangle shows where the receiver positions coincide for the two shots. Target-Hessian/. cable

As for algorithm 3, the receiver loop can be taken out of the shot loop. But in algorithm 4 (towed-streamers), more computations are necessary inside the shot loop to account for the receivers that do not coincide at the beginning and at the end of the cables. I used algorithm 4 for all the examples shown in this thesis.

Algorithm 4 Numerical implementation of the computation of the sparse Hessian in the subsurface-offset domain (equation 3.1) for a towed-streamers marine acquisition (boat pulling cables). Notice that the receiver loop is outside the shot loop, but additional computations are required than in algorithm 3.

```

for all frequencies  $n_\omega$  do
  read green
  for all model space  $(n_x, n_y, n_z, n_{hx}, n_{hy})$  do
    for all model points around  $(x, y, z, h_x, h_y)$   $(na_x, na_y, na_z, na_{hx}, na_{hy})$  do
      for all receiver positions  $(n_{rx}, n_{ry})$  do
        Sum2=Sum2+green(...,irx,iry)*green(...,irx,iry)
      end for
      for all shot positions  $(n_{sx}, n_{sy})$  do
        new=green(...,irxn,iryn)*green(...,irxn,iryn)
        old=green(...,irxo,iryo)*green(...,irxo,iryo)
        Sum2=Sum2-old+new
        H(ix,iy,iz,ihx,ihy,iax,iay,iaz,iahx,iahy)=H(ix,iy,iz,ihx,ihy,iax,iay,iaz,iahx,iahy)
        + green(...,isx,isy)*green(...,isx,isy)*Sum2
      end for
    end for
  end for
end for

```

Savings related to frequency sampling

When using frequency-domain wave-equation migration or waveform inversion (Mulder and Plessix, 2004; Sirgue and Pratt, 2004), the frequency axis can be subsampled to reduce the computational cost. This assumes redundancy in the seismic data with respect to the frequencies.

In time-series analysis, the condition to avoid wrap-around or periodic repetition is given by the Nyquist theorem. In prestack depth-migration, a coarse sampling of the frequency axis can produce artifacts resembling wrap-around, although in a more

subtle way. In practice, the sampling can be coarser than the Nyquist prediction; because migration involves the summation of data from multiple shot gathers and multiple offsets after propagation through a variable-velocity model.

Mulder and Plessix (2004) and Sirgue and Pratt (2004) give analytical formulas for determining the optimal frequency sampling for wave-equation migration and frequency-domain waveform inversion, respectively. Their formulas were limited to constant-velocity media however, so although they illustrated their adequacy on complex synthetics, the validity is not yet demonstrated in poorly illuminated areas.

In this thesis I do not demonstrate optimal frequency sampling, but I use the limited extent in the model space of the PSF (equation 3.1). This property relaxes the required sampling of the frequency axis without wrap-around artifacts contaminating the off-diagonal terms of the Hessian matrix. Figure 3.24 illustrates this idea in a constant-velocity model ($v = 1.5$ km/s). The wavelet has a fundamental frequency of 5 Hz and the bandwidth is 10 Hz. From Figure 3.24a to 3.24i, the frequency sampling is progressively more dense in the computation of the PSF.

Since the PSF is computed only in the neighborhood of the point scatterer (in this case 500 m, in the (x, z) plane), the wrap-around artifacts disappear when the frequency sampling is 0.97 Hz (Figure 3.24g). For a smaller PSF computational window, such as 300 m in the (x, z) plane, a frequency sampling of 1.22 Hz would have been enough (Figure 3.24f).

Conclusions

By considering the sparsity and structure of the Hessian matrix, the acquisition geometry, and the frequency sampling, we can achieve computational savings of five orders of magnitude or more compared to direct implementation. Still, the calculation of the 3-D Hessian requires significant computational resources, especially if the subsurface-offset dimension needs to be computed.

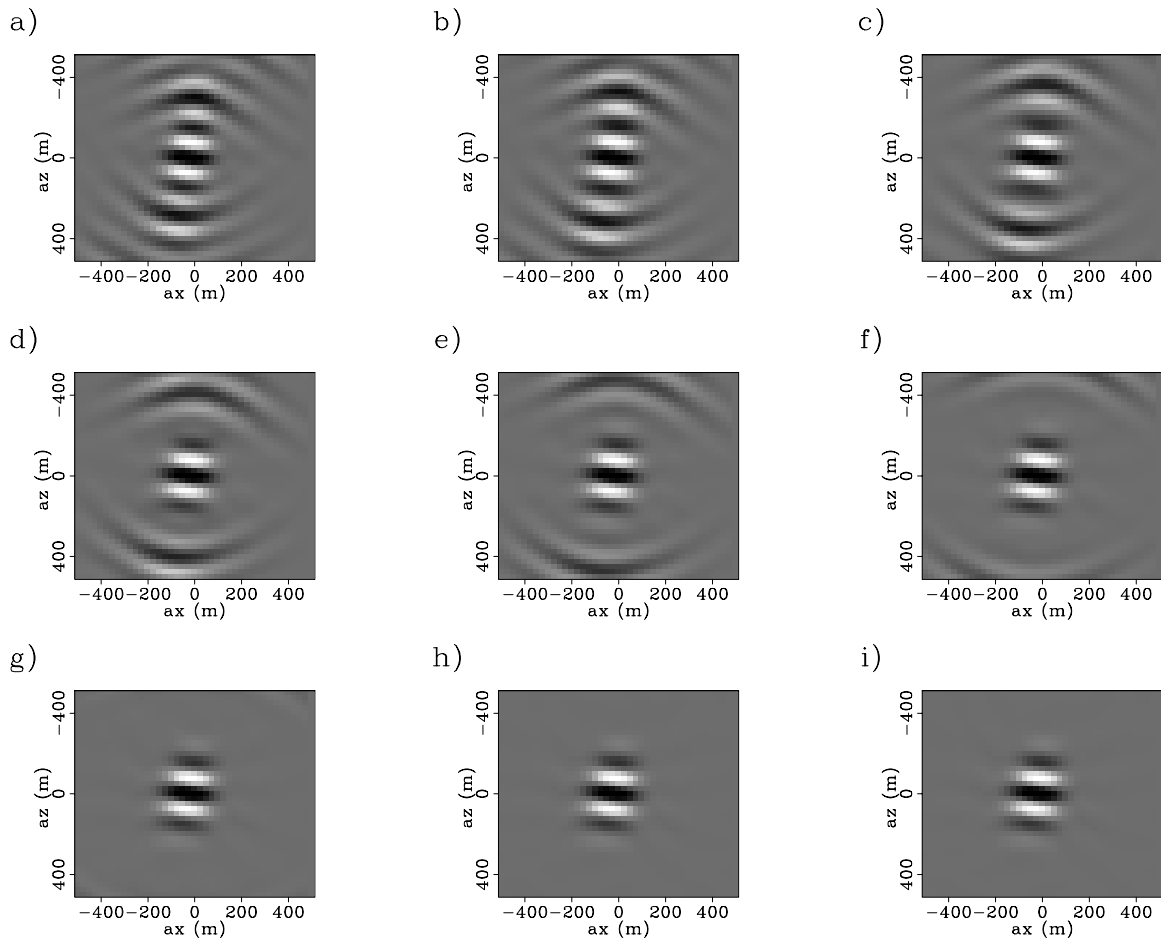


Figure 3.24: PSF as a function of frequency sampling (equation 3.1). a) 2.44 Hz, b) 2.19 Hz, c) 1.95 Hz, d) 1.71 Hz, e) 1.46 Hz, f) 1.22 Hz, g) 0.97 Hz, h) 0.49 Hz, and i) 0.24 Hz. As the frequency sampling decreases, the wrap-around artifacts also decrease. $\boxed{\text{Target-Hessian}/. \text{freq-samp}}$

Chapter 4

Wave-equation inversion in practice

INTRODUCTION

Wave-equation inversion can be done either by explicit computation of the Hessian matrix (chapters 2 and 3) or by an implicit method (Nemeth et al., 1999; Prucha and Biondi, 2002; Kuhl and Sacchi, 2003; Clapp, 2005). The main advantage of the explicit method is that after the Hessian matrix is computed (chapter 3), the regularization, weights, preconditioners, or solvers can be changed without having to recompute Green's functions. For example, regularization always requires parameter adjustment, which can demand several iterations of the inversion process. This can be prohibitively expensive in the implicit method.

In this chapter, I compare two different regularization schemes for the wave-equation inversion in the poststack (equation 2.10), and in the prestack (equations 2.16) image domains. To solve the linear systems in equations 2.10 and 2.16, I use conjugate gradients.

I choose the Sigsbee2B model (Paffenholz et al., 2002) to illustrate the action of the different regularizations. The migration and the Hessian matrix are computed

using the exact (stratigraphic) velocity model (Figure 3.12), so that the migration is as kinematically correct as possible, creating the ideal conditions for the linearized inversion to work.

INVERSION OF THE POINT-SCATTERERS IMAGE

In chapter 3, I created a model with 32 point scatterers and convolved it with the Hessian matrix for the Sigsbee2B model. The resulting image (Figure 3.16) is good for illustrating how the inversion works when the Hessian matches the physics used in migration (one-way wave-equation), and in the absence of noise. Ideally the inversion should recover the scatterers; in practice, the performance of the inversion depends on the condition number of the Hessian matrix. A large condition number both increases the number of iterations required, and limits the accuracy to which the solution can be obtained (Press et al., 1992; Gill et al., 1981).

Wave-equation inversion in the poststack-image domain

In this subsection I illustrate how the wave-equation inversion works when the subsurface offset dimension is not computed. In this situation, the regularization is limited to damping (equation 2.10), and as was shown in chapter 2, no *a priori* knowledge of the properties of the reflectivity can be included besides constraining its size.

Figure 4.1 shows the image of the 32 point scatterers obtained by solving the linear system in equation 2.10 (Figure 4.2 shows the envelope). The result is shown after seven iterations of a conjugate-gradient iterative solver. No regularization was applied. In the well-illuminated areas, the Point Spread Function (PSF) has been reduced in size (compare Figure 4.1 with 3.16 and Figure 4.2 with 3.17). This is the case for all points located in the sediments to the left of the salt body such as the point with coordinates $\mathbf{x} = (31050, 11000)$.

As the point scatters enter a shadow zone, the inversion increases their amplitudes. Compare the point scatterer at position $\mathbf{x} = (34500, 16000)$ in Figures 3.16 and 4.1.

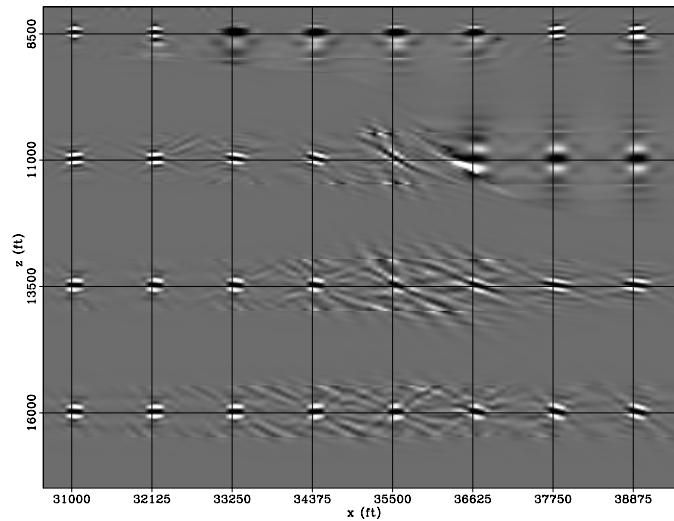


Figure 4.1: Inversion of the image of the 32 point scatterers after seven iterations of a conjugate-gradient iterative solver with no regularization. Compare with Figure 3.16, and notice how the amplitudes have been balanced, and the PSF size has been reduced. Regularization/. conv-Sis-inv

Unfortunately the performance of the inversion degrades most in this area, where we are most interested in recovering the reflectors. This makes clear the need for regularization. The point located at $\mathbf{x} = (35625, 11000)$ is a good example; here the inversion has increased the amplitudes, but the noise has also been increased. As we see later with the Sigsbee2B image, there are almost no primaries in this area of the shadow zone.

Figure 4.3 shows how the norm of the residuals ($\mathbf{r} \cdot \mathbf{r}$) as they change with the number of iterations for different values of regularization parameter ε . The choice of stopping the inversion for $\varepsilon = 0.0$ at iteration seven is not arbitrary, since iterative methods have an inherent regularization property when applied to solve the system of equations (like equation 2.4), and are stopped at the optimal iteration number. Hanke (1995) discuss regularization techniques alternative to Tikhonov regularization. They are based on the *semiconvergence* property of the norm of the residuals –convergence in the beginning of the iteration, divergence eventually. In this thesis I only make use of Tikhonov regularization, but other regularization strategies could be the topic for

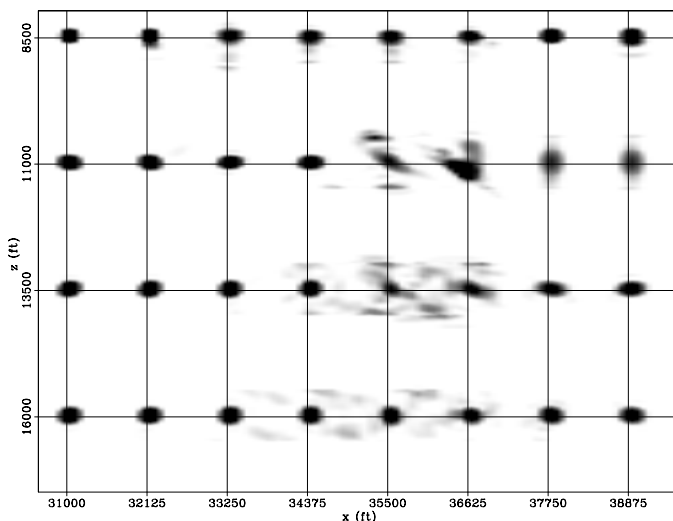


Figure 4.2: Envelope of the inversion of the image of the 32 point scatterers after 7 iterations of a conjugate-gradient iterative solver and no regularization. Compare with the migration in Figure 3.17, and notice how the amplitudes have been balanced, and the PSF size has been reduced. Regularization/. conv-env-Sis-inv

future research.

The convergence of the inversion in the poststack-image domain can be improved by adding a damping factor (equation 2.10). In this case, $\varepsilon = 0.5$ decreases the the norm of the residuals, stabilizing the inversion. The inversion result for the regularization parameter value $\varepsilon = 0.5$ is shown in Figures 4.4 and 4.5. Compared to that in Figures 4.1 and 4.2, this result is more stable in the shadow zones. Adding a “global” regularization, however could degrade the performance of the inversion in the well-illuminated areas. This suggests that the use of a spatially variable regularization parameter that would be applied only in the shadow zones should improve the regularize inversion results.

Wave-equation inversion in the prestack-image domain

As explained in chapter 2, a more sophisticated regularization could be to force the model to fulfill the semblance principle. In the subsurface-offset dimension, this

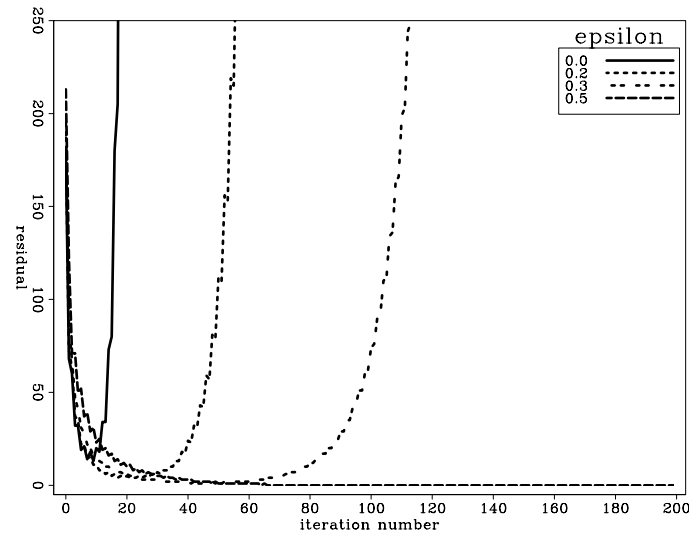


Figure 4.3: Norm of the residuals as they change with number of iterations of a conjugate-gradient iterative solver for different regularization parameters ε in the poststack image domain. The parameter choice $\varepsilon = 0.5$ decreases the norm of the residuals, stabilizing the inversion. Regularization/. res-ir

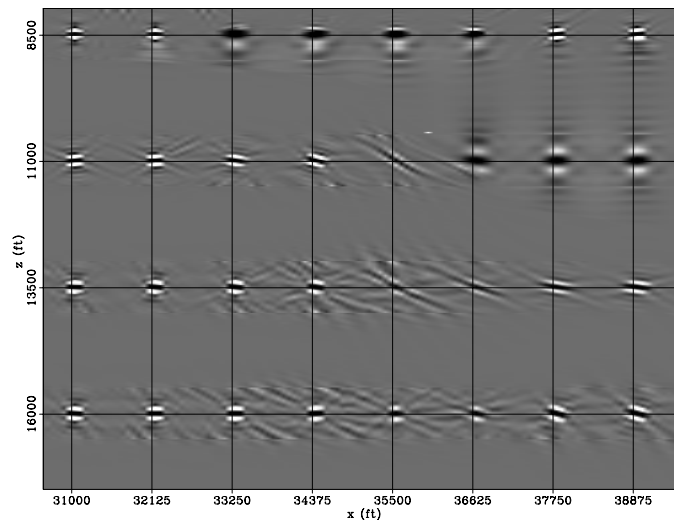


Figure 4.4: Inversion of the image of the 32 point scatterers after 200 iterations of a conjugate-gradient iterative solver with regularization parameter $\varepsilon = 0.5$. Compare with Figures 3.16, notice how the amplitudes have been balanced, and the PSF size has been reduced. Compared with 4.1 the amplitudes in the shadow zone are weaker, but the result is cleaner. Regularization/. conv-Sis-inv05

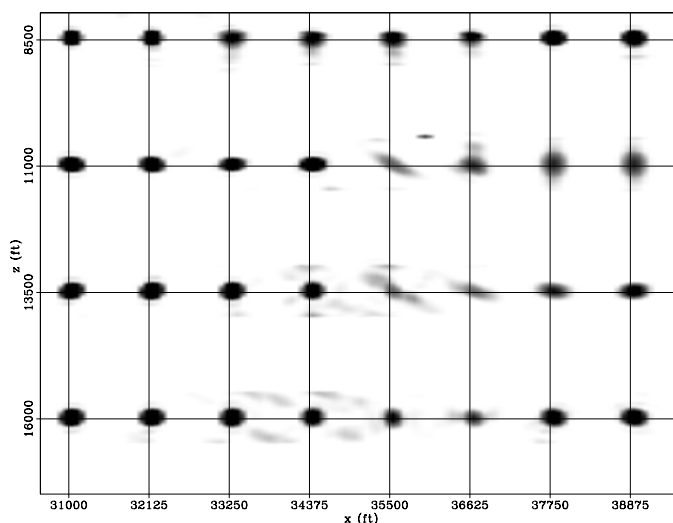


Figure 4.5: Envelope of the inversion of the image of the 32 point scatterers after 200 iterations of a conjugate-gradient iterative solver with regularization parameter $\varepsilon = 0.5$. Compare with Figures 3.16, notice how the amplitudes have been balanced, and the PSF size has been reduced. Compared with 4.1 the amplitudes in the shadow zone are weaker, but the result is cleaner. `Regularization/. conv-env-Sis-inv05`

consists of penalizing the energy in the image that is not focused at zero subsurface offset (equation 2.19). To apply this regularization, the model must be expanded to include the subsurface offset dimension.

Adding the new dimension increases the size and the number of nonzero coefficients of the Hessian matrix, increasing the cost of the inversion by an order of magnitude. The regularization becomes more important now since, as the size of the matrix increases, the inversion becomes more susceptible to numerical errors.

As with inversion in the poststack image domain, the result of the inversion is unstable in the absence of regularization (Figure 4.6). Figure 4.7 shows the image obtained in the subsurface-offset domain by solving the linear system in equation 2.16, using seven iterations of the conjugate-gradients solver with no regularization. The front panel (to the left) shows the zero subsurface offset, and the side panel (to the right) shows the subsurface-offset gather at position $x = 35550$ ft. Compared to Figure 3.20 notice how the amplitudes have been balanced everywhere except in

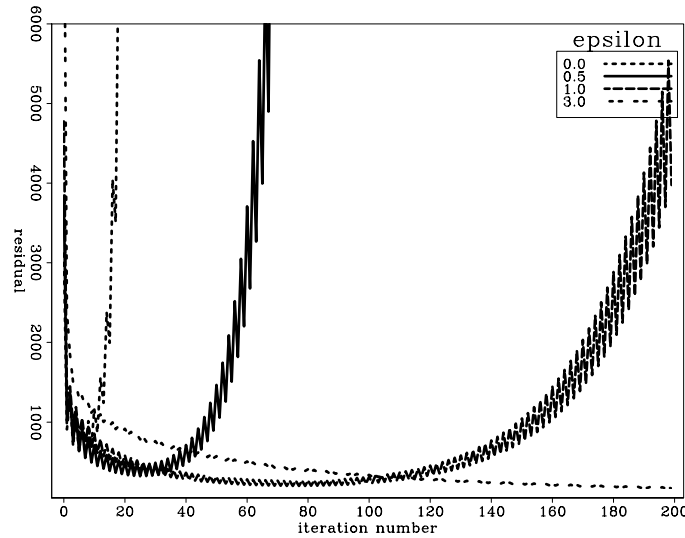


Figure 4.6: Norm of the residuals as they change with the number of iterations of a conjugate-gradient iterative solver, for different regularization parameters ε in the prestack image domain. The parameter choice $\varepsilon = 3.0$ makes the norm of the residuals decrease, stabilizing the inversion. Regularization/. res-ir-off

the shadow zone. Also notice how the size of the three dimensional PSF has been reduced, mainly in the x and z dimensions.

The reduction in the size of the PSF in the subsurface-offset dimension can be better judged after transforming the inverted image to the reflection-angle domain by slant stacking (Sava and Fomel, 2003) (Figure 4.8). The front panel shows a constant-angle section (at 18°), and the side panel shows the reflection-angle gather at position $x = 35550$ ft. Comparing this figure with the migration (Figure 3.21), we see that the gaps in the angle coverage have been partially filled by the inversion. We also see again that the inversion becomes unstable inside the shadow zone.

Adding the regularization in the subsurface offset makes the inversion result stable (from the norm of the residuals in Figure 4.6). Figure 4.9 shows the image of the 32 point scatterers in the subsurface-offset domain, obtained by solving the linear system in equation 2.16 with the differential semblance as the regularization operator and $\varepsilon = 3.0$ (equation 2.19). The front panel shows the zero subsurface-offset image, and

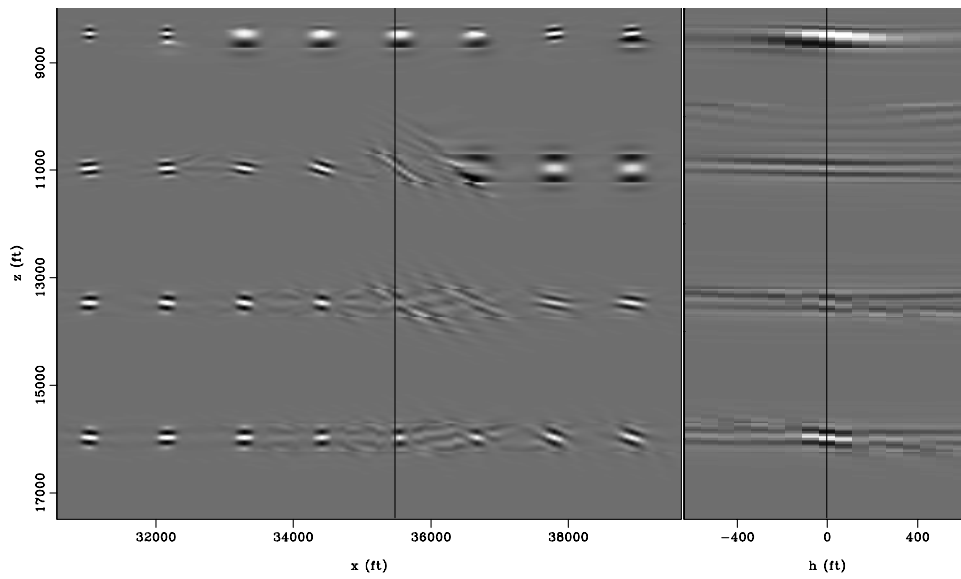


Figure 4.7: Inversion of the image of the 32 point scatterers in the subsurface-offset domain after seven iterations of the conjugate-gradient solver and no regularization. Compare with the migration (Figure 3.20); notice how the amplitudes have been balanced, and the size of the three dimensional PSF has been reduced, but the result is unstable in the shadow zone. `Regularization/. conv-Sis-inv-offzero`

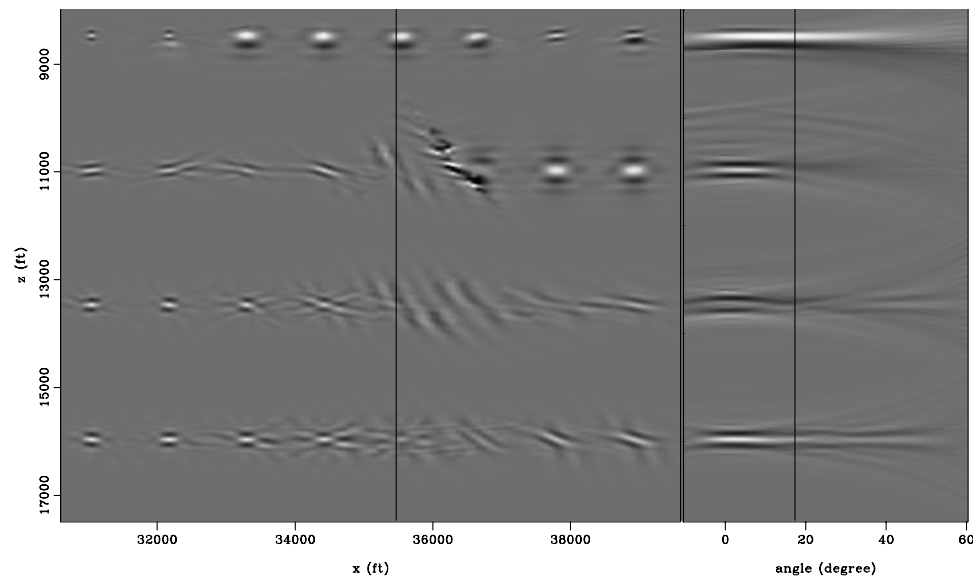


Figure 4.8: Inversion of the image of the 32 point scatterers in the reflection-angle domain (offset-to-angle transformation), after seven iterations of the conjugate-gradient solver and no regularization. Compare with Figure 3.21; notice how the gaps in the angle coverage has been partially filled by the inversion, the amplitudes have been balanced, and the PSF size has been reduced. Regularization/. conv-Sis-inv-angzero

the side panel shows the subsurface-offset gather at position $x = 35550$ ft. Compared to the migration shown in Figure 3.20, besides the usual benefit of balancing the amplitudes, the width of the PSF has been reduced in the all three dimensions. Also, if we compare the inversion results with and without regularization (Figure 4.9 versus 4.7), we can see a reduction of the PSF in the subsurface-offset dimension. This shows that the regularization is working.

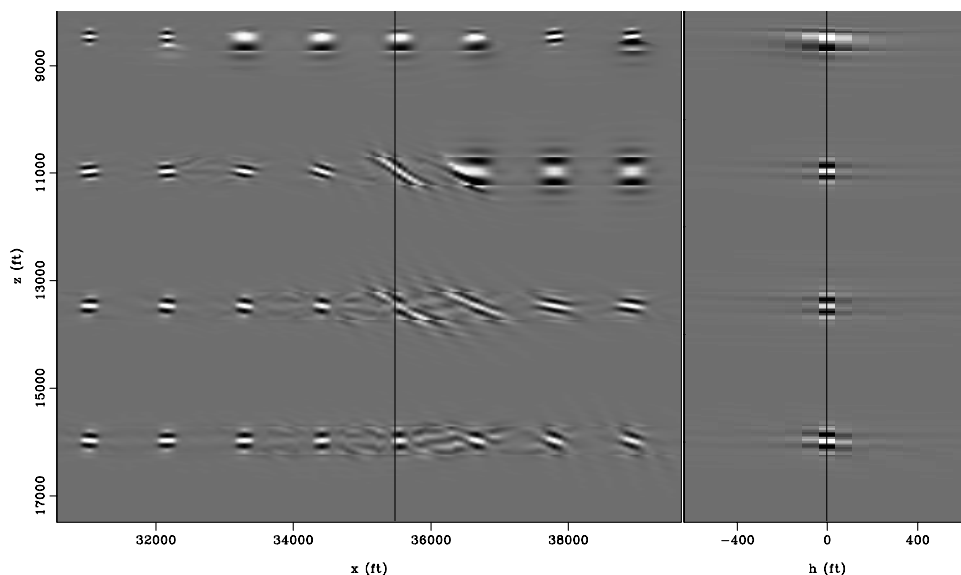


Figure 4.9: Inversion of the image of the 32 point scatterers in the subsurface-offset domain after 200 iterations of the conjugate-gradient solver and regularization parameter $\varepsilon = 3.0$. Compare with the migration in Figure 3.20 and the inversion without regularization in Figure 4.7; notice how the amplitudes have been balanced, and the size of the three dimensional PSF has been reduced. Regularization/. conv-Sis-inv-off

Figure 4.10 shows the inverted image in the reflection-angle domain. Comparing this result with the migration (Figure 3.21) and with the inversion with no regularization (Figure 4.8), we see that the inversion is stable in the shadow zone. Also, the inversion plus regularization equalizes the amplitudes in the angle gathers, filling the illumination gaps.

Another interesting comparison can be made between the regularized inversion in the poststack image-domain and the zero subsurface-offset of the regularized inversion

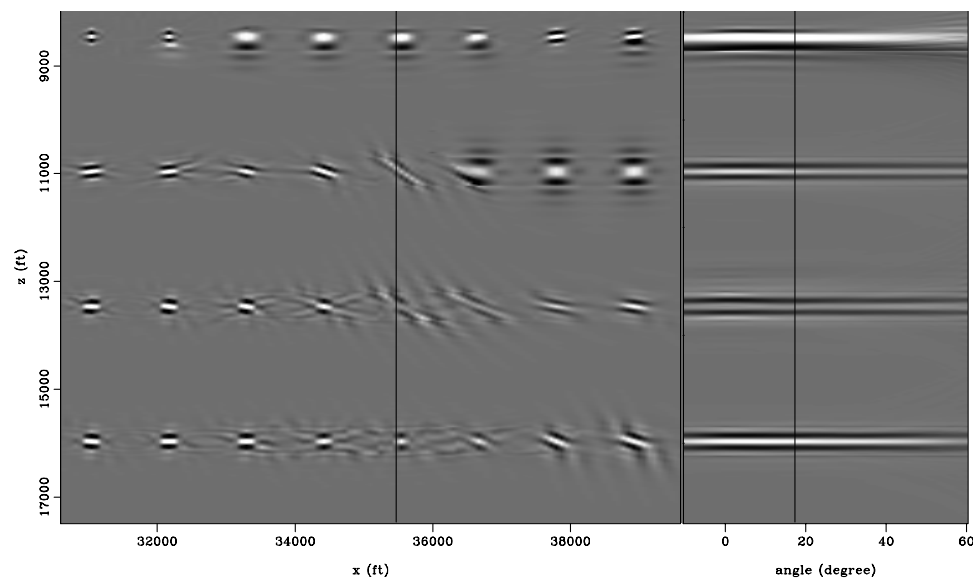


Figure 4.10: Inversion of the image of the 32 point scatterers in the reflection-angle domain (offset-to-angle transformation) after 200 iterations of the conjugate-gradient solver and regularization parameter $\varepsilon = 3.0$. Compare with Figures 3.21 and 4.8; notice that the amplitudes have been balanced, and the PSF size has been reduced. Also, the inversion with regularization equalizes the amplitude in the angle gathers, filling the illumination gaps. Regularization/. conv-Sis-inv-ang

in the prestack image-domain. Figure 4.11 shows the zero subsurface offset (front panel of Figure 4.9) at the same scale as Figure 4.1 (poststack image-domain inversion) to allow direct comparison. The regularized inversion in the prestack image-domain shows the same level of amplitudes inside and outside the shadow zone, whereas the regularized inversion in the poststack-image domain shows lower amplitudes inside the shadow zone than outside. This comparison shows that the considerable cost of adding one dimension to the model space allows a regularization that has the potential of yielding better results.

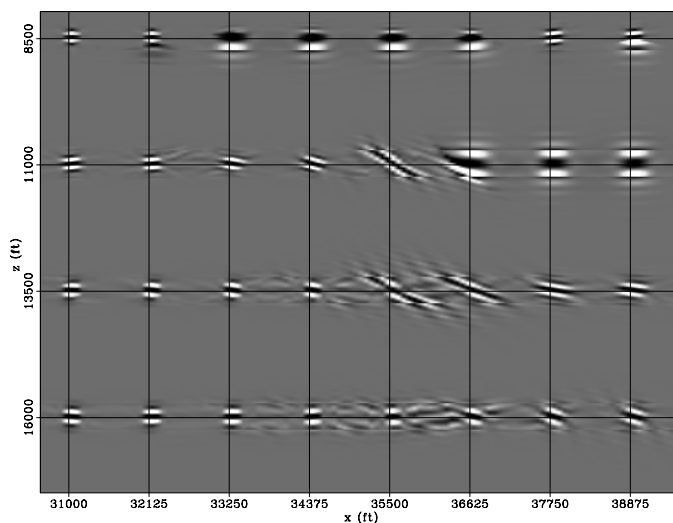


Figure 4.11: Zero subsurface-offset of the regularized inversion in the prestack image-domain (front panel of Figure 4.9), at the same scale as Figures 3.16, 4.1, and 4.4. Notice how the amplitudes have been balanced and the PSF size has been reduced.

Regularization/. conv-Sis-inv-zoff

INVERSION OF THE SIGSBEE2B DATA

The salt body in the Sigsbee2B model produces irregular illumination of the subsurface. Two main shadow zones can be seen by analyzing the diagonal of the Hessian matrix for this model (Figure 3.15). Inside the shadow zones, the primaries are weak and are contaminated with salt-related multiples. This is a problem we often encounter in field data. I address the multiples problem in Appendix B.

Irregular angle illumination

Figure 4.12 shows the angle stack of the shot-profile migration (using a cross-correlation imaging condition) corresponding to the portion of Sigsbee2B model shown inside the target box in Figure 3.12. Note that the shadow zones in Figure 3.15 coincide with the areas where the amplitudes of the reflectors fade in the migration. From the reflection coefficients shown in Figure 4.13, we know that the amplitude of the events should not change as they get closer to the salt. It is this weakening of the amplitude in this region of Figure 4.12 that we would like to address.

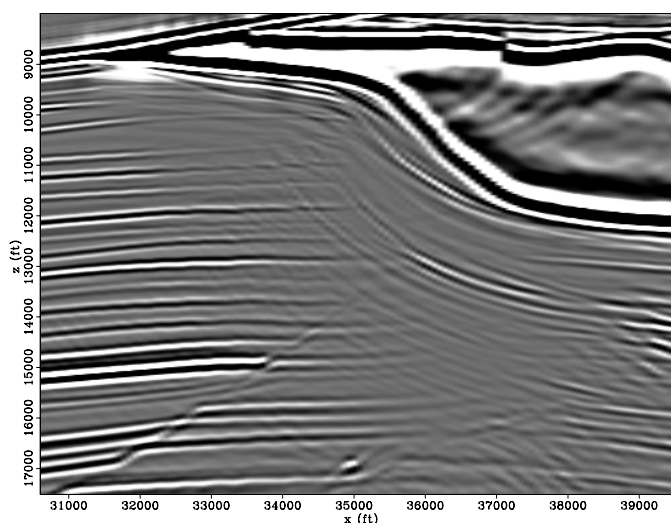


Figure 4.12: Angle stack of the Sigsbee2B shot-profile migration (Figure 4.14).
 Regularization/. mig-stack

The explanation for this discrepancy can be found by analyzing the migration image before stacking. Figure 4.14 shows the migration in the reflection-angle domain. The front face corresponds to the image at a 25° reflection angle, and the side face corresponds to the reflection-angle gather at a position below the tip of the salt ($x = 32300$ ft). Figure 4.15 shows the migration result in the subsurface-offset domain. The front face corresponds to the image at zero subsurface offset, and the side face corresponds to the subsurface-offset gather at position $x = 32300$ ft.

In the shadow zone below the tip of the salt, the reflectors are imaged at a few

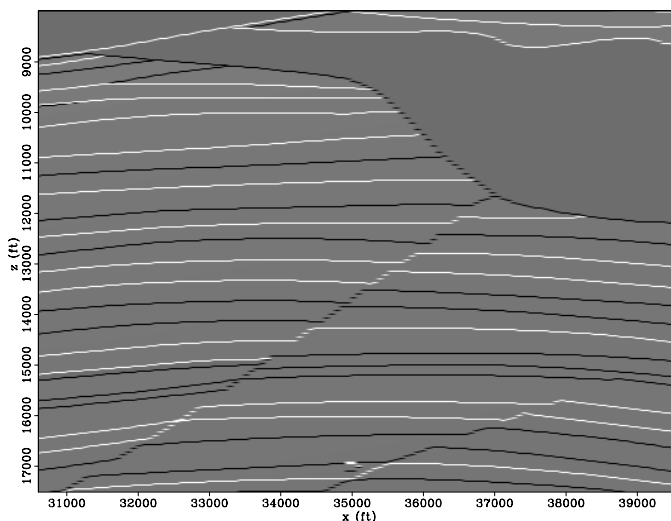


Figure 4.13: Reflection coefficients of the Sigsbee2B model. Regularization/. refle-new

near reflection angles (not focused at zero subsurface-offset), leaving gaps in the angle illumination. The irregular illumination with angle translates into a biased stack image that is difficult to use for interpretation.

Another well-known problem in shadow zones are the “migration smiles” that are created in their proximity. They give the misleading impression that the dip of the reflectors is curving up as they enter the shadow zones. This increases the risk of misinterpreting the geometry of the reservoirs.

Processing before inversion

By comparing the migrated image in Figure 4.12 with the reflection coefficients shown in Figure 4.13 we see events in the migration that do not correspond to the geology. These are well-known artifacts that correspond to multiple reflections inside the salt body that mask the weak primaries signal that we wish to increase by the inversion. The Sigsbee2B model Hessian (Figure 3.13), and the migration (Figure 4.12) were computed using one-way wave-equation propagators. As the result, the multiples were

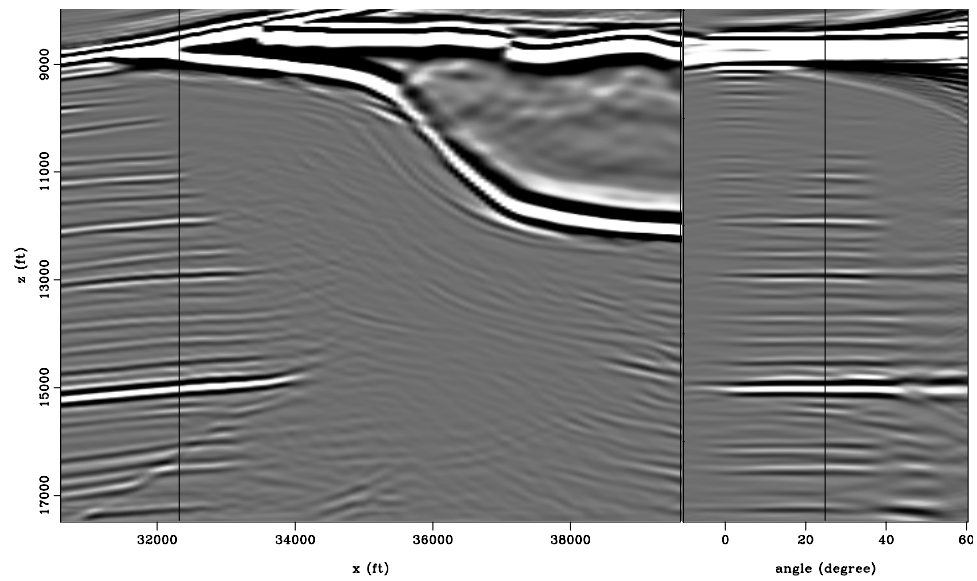


Figure 4.14: Sigsbee shot-profile migration (reflection angle) using a cross-correlation imaging condition. The front face corresponds to the image at a 25° reflection angle, and the side face corresponds to the reflection-angle gather at $x = 32300$ ft.

Regularization/. migang

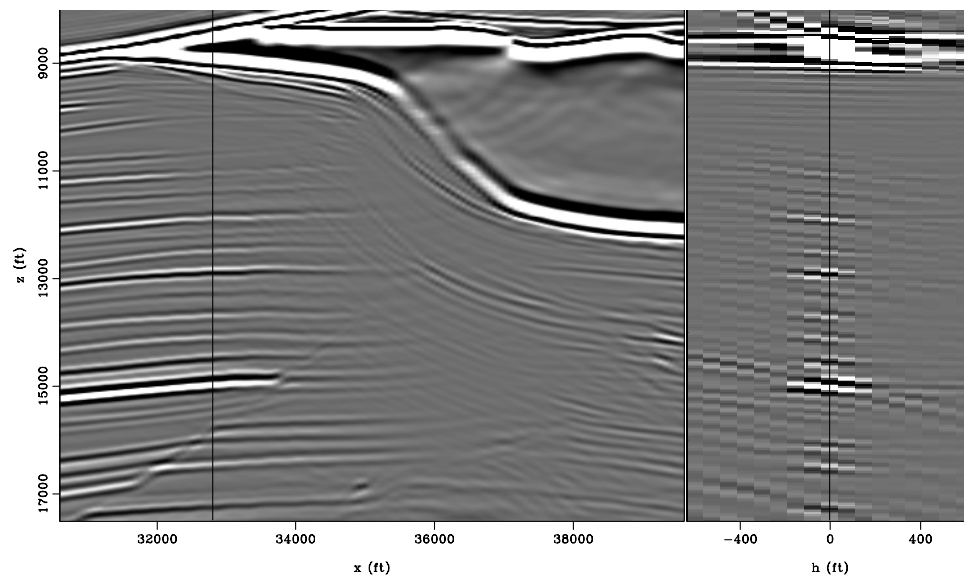


Figure 4.15: Sigsbee shot-profile migration (subsurface-offset) using cross-correlation imaging condition. The front face corresponds to the image at zero subsurface-offset, and the side face corresponds to the subsurface-offset gather at $x = 32300$ ft.

Regularization/. migoff

neither included in the modeling nor propagated with the correct velocity/direction during migration. For this reason, the multiples should be treated as noise for the inversion. Later, I will show how they can make the inversion fail to recover the primaries signal in the shadow zones.

One solution to this problem is to suppress the multiples (events that do not fit the physics of the operator) from the migration. This requires the multiples to be separated from the primaries in such a way, that during removal, the primaries are minimally altered. In Appendix B, I give a detailed explanation of the demultiple processing. The resulting angle-stack of the demultiple migration can be seen in Figure 4.16. Comparing it with the unfiltered stack (Figure 4.12), we see the effectiveness of the process.

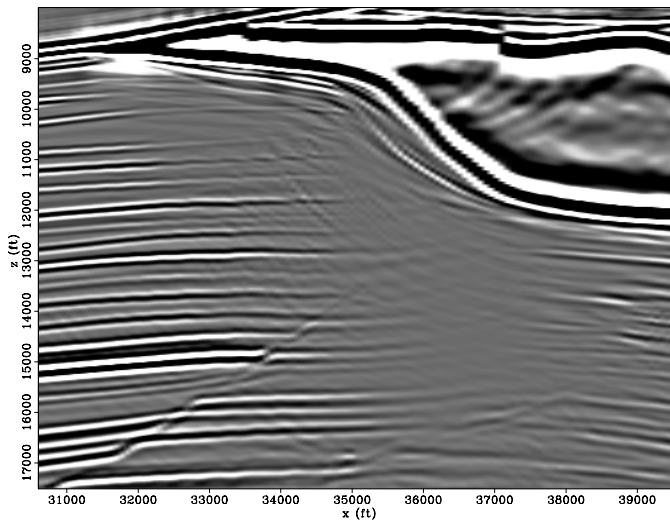


Figure 4.16: Angle stack of the Sigsbee2B shot-profile migration after filtering the salt-related multiple reflections (Figure B.7). `Regularization/. mig-stack-filt`

Inversion in the poststack image-domain

In this subsection, I solve the linear system in equation 2.10 for two different right-hand-side vectors. One is the migrated image at zero subsurface offset without filtering (front panel, Figure B.2), and the other is the migrated image at zero subsurface

offset after filtering (front panel, Figure B.6).

The results of the inversion are shown in Figures 4.17 and 4.18 (unfiltered and filtered input), and should be compared with the migrations shown in Figures 4.12 and 4.16 respectively. The inversion with the unfiltered migration is more unstable, needing a higher value of the regularization parameter, which reduces the effectiveness of the inversion outside the shadow zones. Thus, I choose to limit the number of iterations instead of adding a regularization parameter for this case. The result in Figure 4.17 shows the inversion of the unfiltered migration after seven iterations, without regularization.

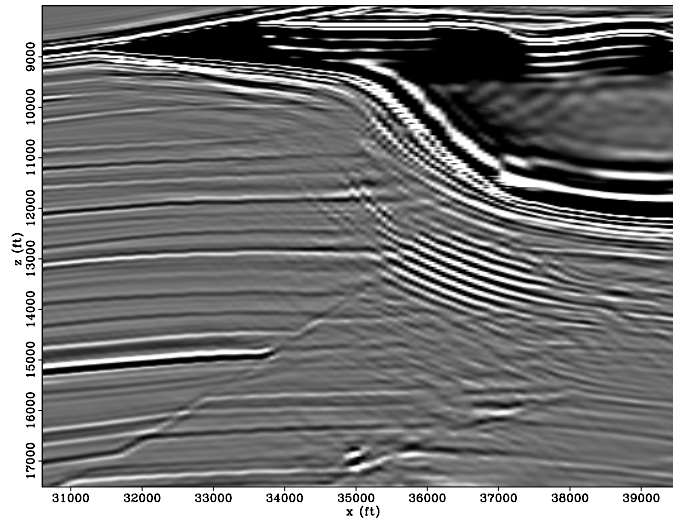


Figure 4.17: Inversion in the poststack image domain with the unfiltered migration as the input (equation 2.10) after seven iterations of a conjugate-gradient iterative solver and no regularization. Regularization/. invz

The inversion of the filtered migration shows a convergence behavior similar to that of the image of the 32 scatterers (Figure 4.3). The choice of regularization parameter, $\varepsilon = 2.0$, decreases the norm of the residuals and stabilizes the inversion.

Overall, the inversion results have more balanced amplitudes, allowing the continuation of the reflector inside the shadow zones with the much-improved kinematics (reducing the migration smiles). The reflectors also gain vertical and horizontal resolution, particularly seen at the two faults present in the reflectivity model (Figure

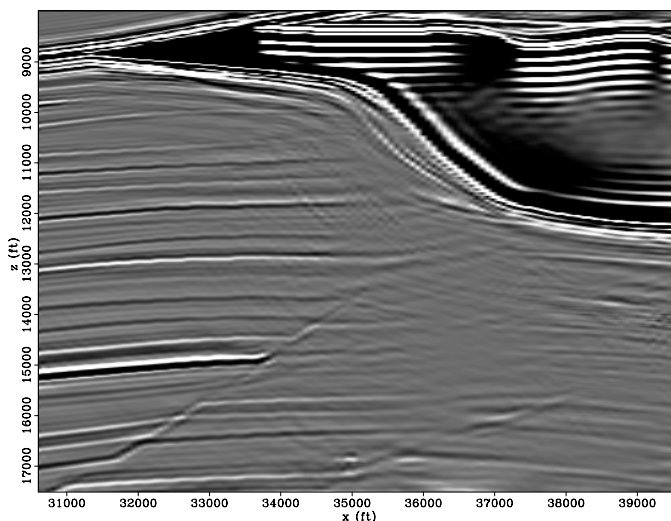


Figure 4.18: Inversion in the poststack image domain with a filtered migration as the input (equation 2.10) with a regularization parameter $\varepsilon = 2.0$.

Regularization/. invz-filt

4.13). They can be better interpreted in the inversion than in the migration.

Figures 4.19, and 4.20 show the residuals of the inversion with the unfiltered migration, and with the filtered migration, after seven iteration of the conjugate-gradient solver. As expected, the residuals in the unfiltered inversion become large in the shadow zone, making the conjugate-gradient solver increase the amplitude of the multiples that were not included in the computation of the Hessian. On the other hand, the filtering of the multiples before inversion allows the inversion process to boost the amplitude of the primaries in the shadow zone. Unfortunately the multiples were not completely removed by filtering, so the inversion procedure also increases their amplitudes.

Inversion in the prestack image domain

When imaging subsalt sediments, it is often desirable to compute prestack image domain gathers. Winbow et al. (2007) show that different angles contribute to different

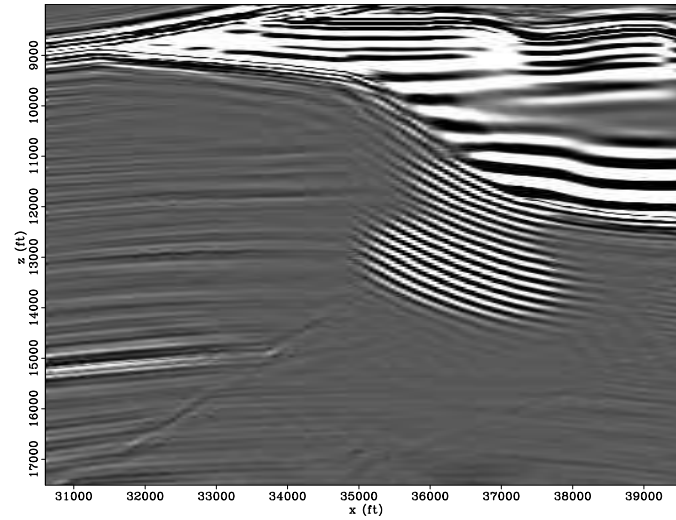


Figure 4.19: Residuals of the inversion in the poststack image domain with the unfiltered migration as the input (equation 2.10) after seven iterations, with a regularization parameter $\varepsilon = 0.0$. `Regularization/.resinvz`

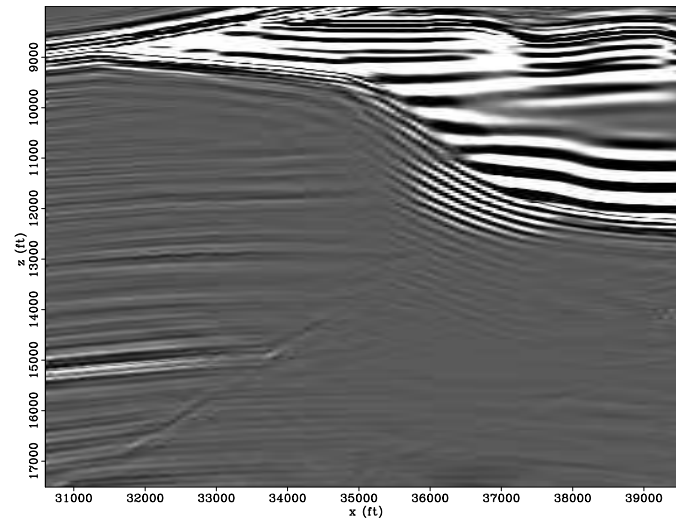


Figure 4.20: Residuals of the inversion in the poststack image domain with a filtered migration as the input (equation 2.10) after seven iterations, with a regularization parameter $\varepsilon = 0.0$. `Regularization/.resinvz-filt`

portions of the image space depending on the geometry of the salt, so that stacking different angle ranges improve interpretation.

To obtain inverted images in the prestack image-domain a more general inversion problem has to be solved as a result of including the subsurface-offset dimension in the model space (equation 2.16). The regularization in the subsurface offset complements the inversion while filling the illumination gaps in the reflection-angle dimension, as was shown with the image of the 32 scatterers (Figure 4.10).

The filtered migrated image (Figure B.6) was chosen as the input to the inversion in order to reduce the detrimental multiples contamination in the shadow zones. The norm of the residuals show a convergence behavior similar to that in the image of the 32 scatterers (Figure 4.6).

Figure 4.21 shows the inversion result in the subsurface-offset domain as the result of solving the linear system in equation 2.16 after 20 iterations of the conjugate-gradients solver with no regularization. The front face corresponds to the image at zero subsurface offset, and the side face corresponds to the subsurface-offset gather at position $x = 32300$ ft. Figure 4.22 shows the result of transforming the image in Figure 4.21 to the reflection-angle domain. The front face corresponds to the image at a 25° reflection angle, and the side face corresponds to the reflection-angle gather at a position below the tip of the salt ($x = 32300$ ft). Comparing it to the migration (Figure 4.14), we see that some of the gaps in the angle coverage have been partially filled by the inversion.

Adding the regularization in the subsurface offset makes the inversion result stable. Figure 4.23 shows the image in the subsurface-offset domain, obtained by solving the linear system in equation 2.16 with differential semblance as the regularization operator and $\varepsilon = 4.0$ (equation 2.19). The front panel shows the zero subsurface offset, and the side panel shows the subsurface-offset gather at position $x = 32300$ ft. Compare with the migration shown in Figure 4.15; besides the usual benefit of balancing the amplitudes, the PSF has been reduced in all three dimensions. Also if we compare the inversion results with and without regularization (Figure 4.21 versus

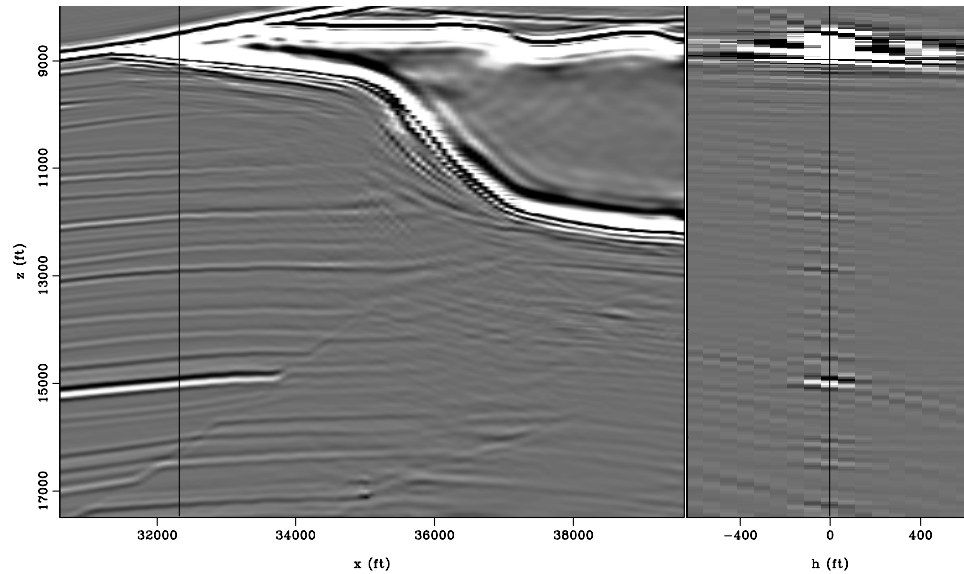


Figure 4.21: Sigsbee inversion without regularization in the subsurface-offset domain. The front face corresponds to the image at zero subsurface-offset, and the side face corresponds to the subsurface-offset gather at $x = 32300$ ft. Regularization/. invoff-zero

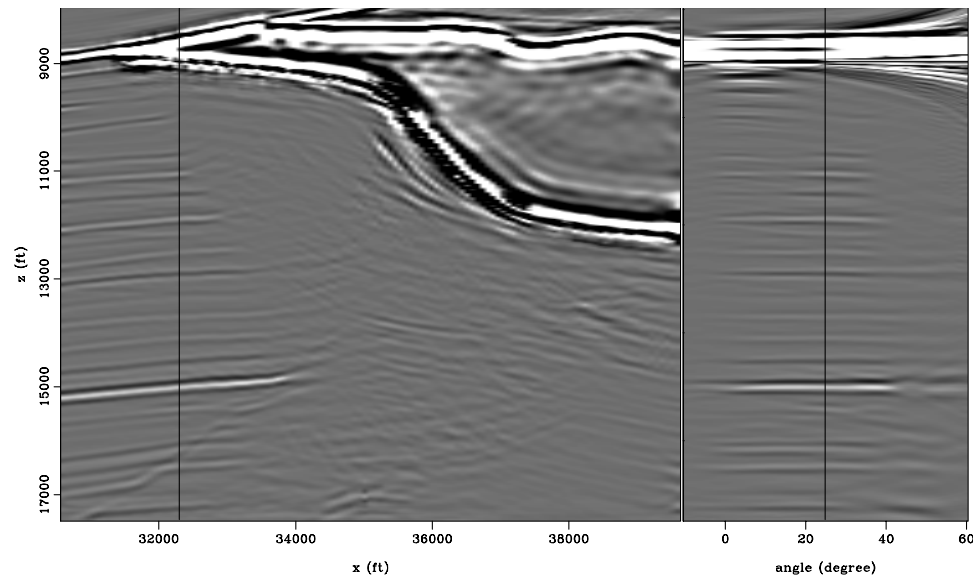


Figure 4.22: Sigsbee inversion without regularization in the reflection angle. The front face corresponds to the image at a 25° reflection angle, and the side face corresponds to the reflection-angle gather at $x = 32300$ ft. Regularization/. invang-zero

4.23), we see a reduction of the image in the subsurface-offset dimension.

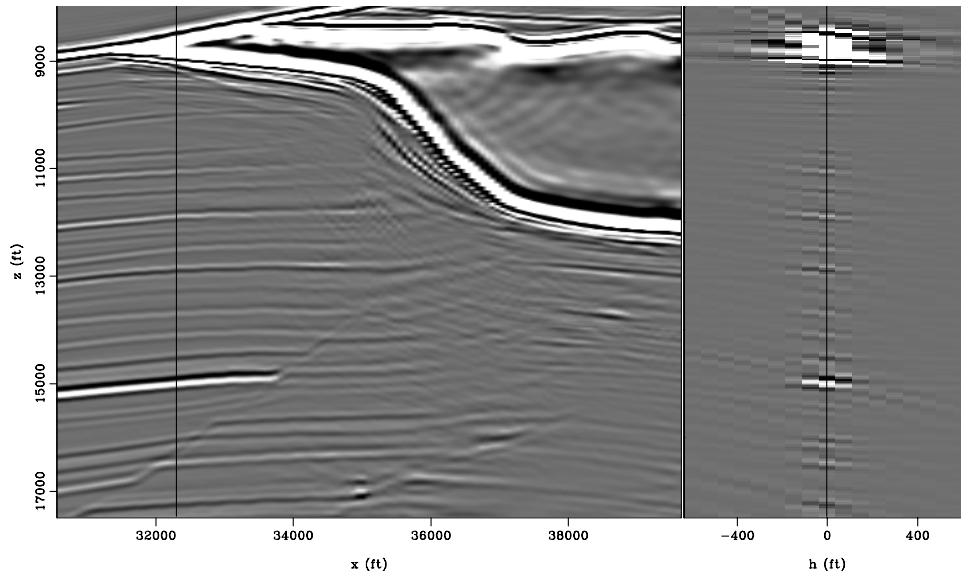


Figure 4.23: Sigsbee regularized inversion in the subsurface-offset domain ($\varepsilon = 4.0$). The front face corresponds to the image at zero subsurface-offset, and the side face corresponds to the subsurface-offset gather at $x = 32300$ ft. Regularization/. invoff4

Figure 4.24 shows the inverted image in the reflection-angle domain. Comparing this result with the migration (Figure 4.14) and with the inversion with no regularization (Figure 4.22), we see that the inversion is stable in the shadow zone. Also, the inversion-plus-regularization equalizes the amplitudes in the angle gathers, filling the illumination gaps. Figure 4.25 shows three angle gathers at three different locations that correspond to: the migration (top row), the inversion without regularization (middle row), and the regularized inversion (bottom row). Note that the illumination is compensated as we move from migration to regularized inversion.

Finally, Figures 4.26 and 4.27 show the angle stack without and with regularization. The regularized inversion give a less noisy result inside the shadow zone, since the regularization attenuates events that are not flat in the angle gathers (such as multiples). By comparing this images with the filtered migration (Figure 4.16), we see that the inversion produces a result with better resolution and more balanced amplitudes. As with inversion in the poststack image-domain, the reflectors can be

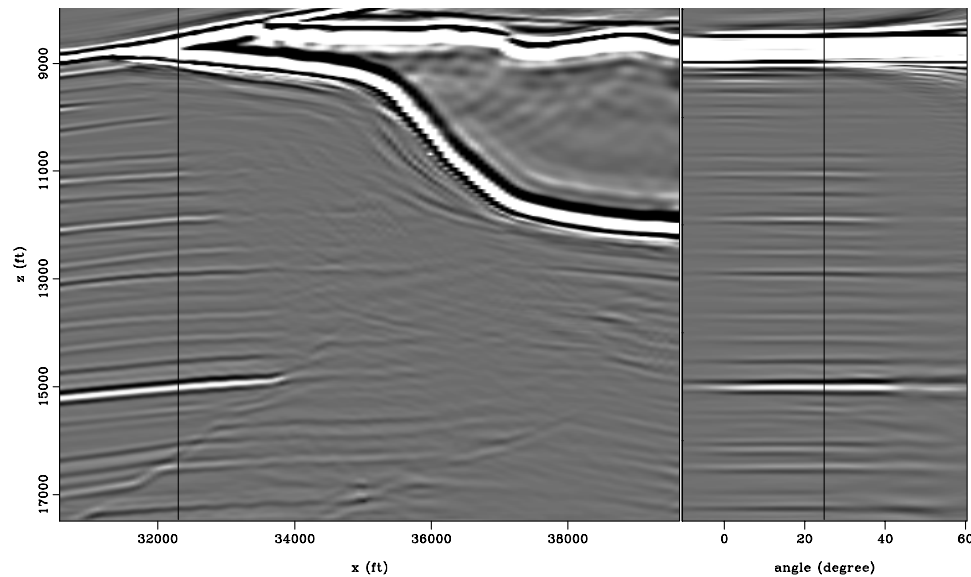


Figure 4.24: Sigsbee regularized inversion in the reflection angle ($\varepsilon = 4.0$). The front face corresponds to the image at 25° reflection angle, and the side face corresponds to the reflection-angle gather at $x = 32300$ ft. `Regularization/. invang4`

better followed into the shadow zones with much-improved kinematics. Compared with the inversion in the poststack image-domain (Figure 4.18), there is a better signal-to-noise ratio in the shadow zones.

CONCLUSIONS

Regularization can be implemented in the zero subsurface offset, where the options for an operator are limited to a customary damping, or in the subsurface offset, where differential semblance can be applied. The differential semblance, although it is more expensive, can improve the continuity of the reflectors into the shadow zones with a higher signal-to-noise ratio than can the damping in the zero subsurface offset.

In different zones of the image, quality of the inversion result can vary depending on the regularization operators or parameters. In my proposed methodology the cost of the computation of the Green functions and the Hessian matrix is higher than

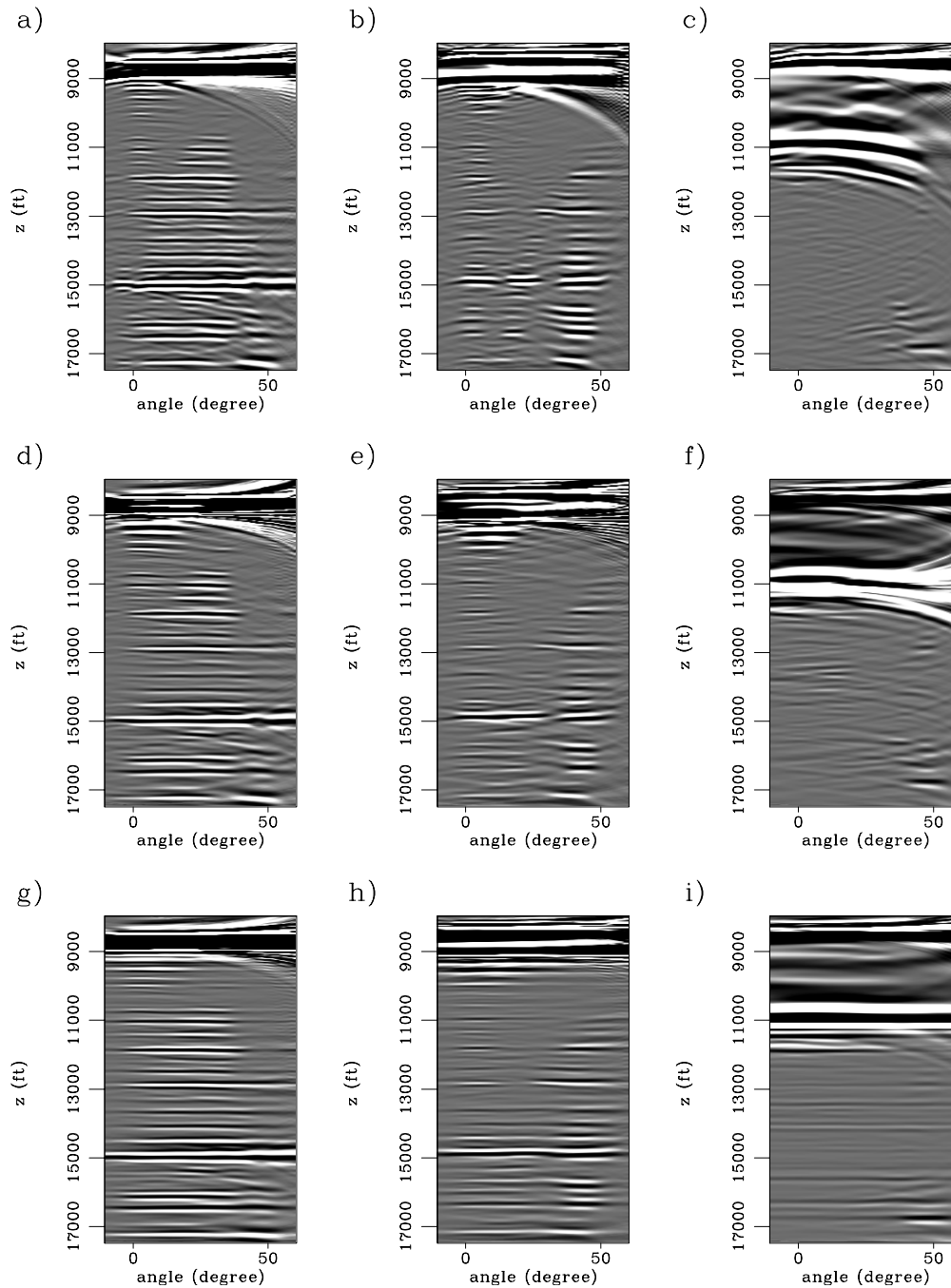


Figure 4.25: Angle gathers corresponding to the migration (top row), the inversion without regularization (middle row), and the regularization inversion for $\varepsilon = 4.0$ (bottom row) at three locations. a), b), and g) $x = 32300$ ft; b), e), and h) $x = 33725$ ft; and c), f), and i) $x = 36500$ ft. Regularization/. comp-ang

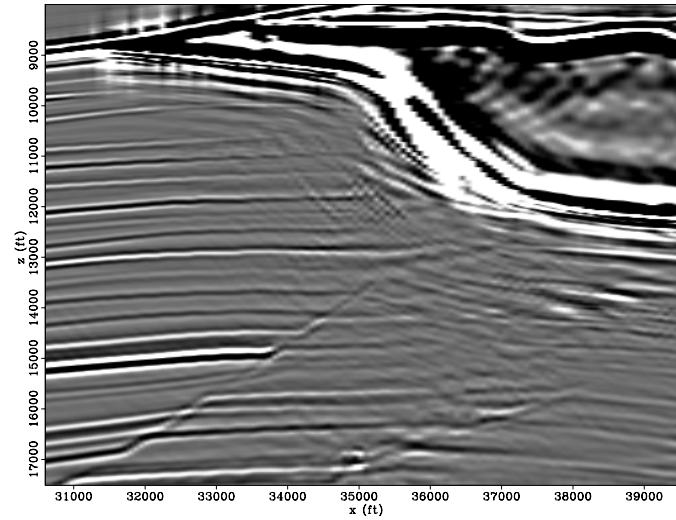


Figure 4.26: Angle stack of the inversion without regularization (the front panel of Figure 4.22 showed the result for just 25° reflection angle).
 Regularization/. inv-stack-filt0

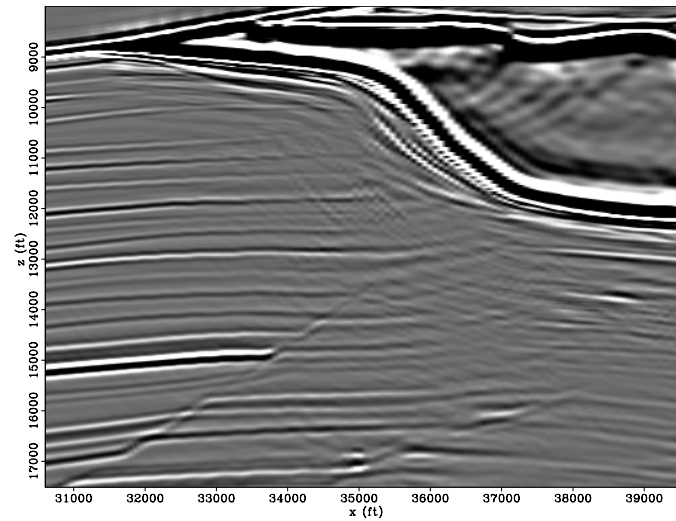


Figure 4.27: Angle stack of the regularized inversion with $\varepsilon = 4.0$ (the front panel of Figure 4.24 showed the result for just 25° reflection angle).
 Regularization/. inv-stack-filt4

the inversion per se. This makes it suitable as an interpretation tool because, after computing the Hessian just once, the regularization parameters or the regularization operator can be changed to produce different inversion results with reasonable efficiency.

Chapter 5

Field data examples

In this chapter, I apply the wave-equation inversion methodology to a subset of a 3-D data set from the Gulf of Mexico provided to SEP by BP and ExxonMobil. The same data was used by Clapp (2005) to demonstrate the validity of implicit regularized inversion approach. The images and velocity model are shown with no axis information at the request of the company who provided the data.

THE 3-D GULF OF MEXICO DATA

The 3-D velocity model corresponding to the subset of the data can be seen in Figure 5.1. The salt body on the right side causes significant shadow zones that can mask potential hydrocarbon reservoirs. The velocity model is believed to be accurate, which is important given the linearity of the operators assumption with respect to the background velocity used to derive the Hessian (Chapter 2). I choose a target zone (indicated with the “target” box in Figure 5.1) to test how the inversion performs in imaging the subsalt sediments. The dimensions of the target volume are 3630 ft in depth, 12303 ft in the x -dimension, and 4101 ft in the y -dimension.

The data that contributed to the migration were small subset of the data provided by BP and ExxonMobil. The reduced data set contained 10000 shots, 200 shot

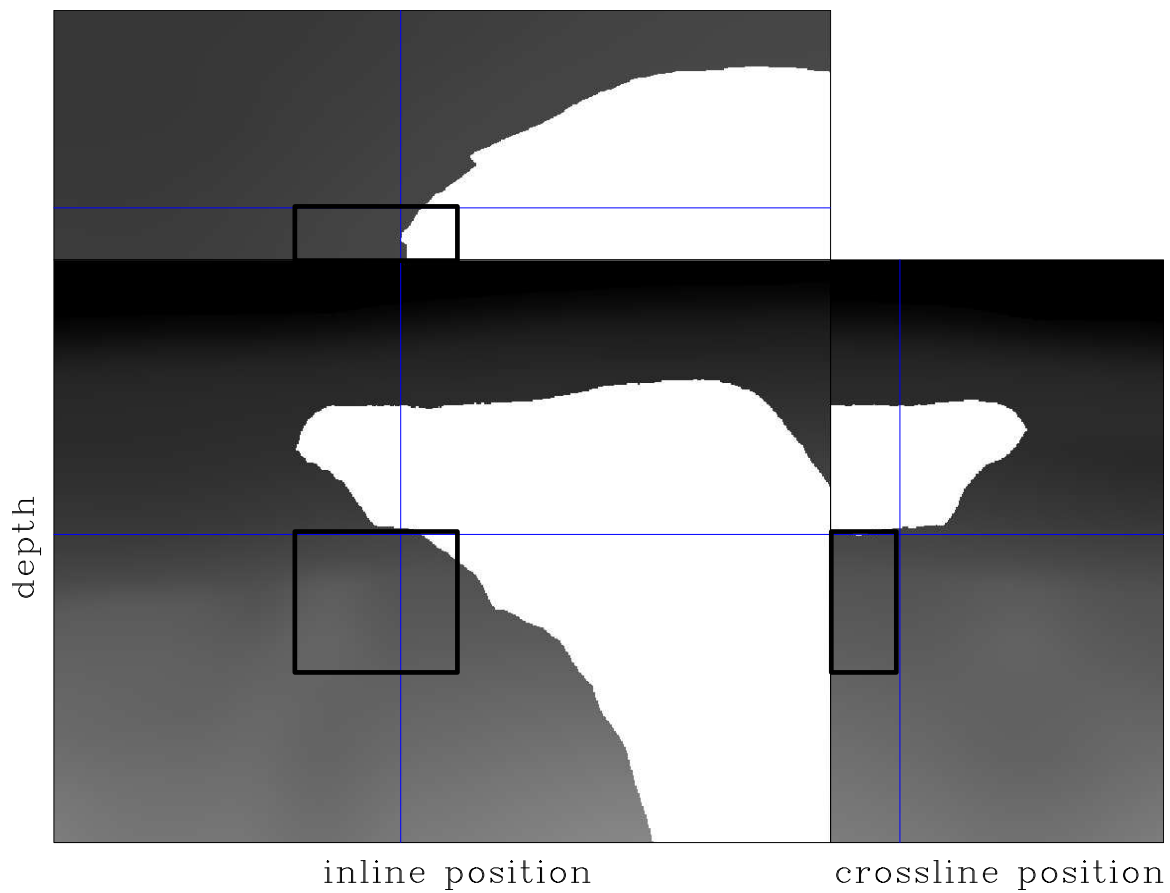


Figure 5.1: Velocity model for the 3-D Gulf of Mexico data; target zone indicated with the “target” box. `Field-data/. velo`

positions in the inline direction (x) and 50 shot positions in the crossline direction (y). The decision to use a reduced data set, particularly in the crossline direction, was based on the computational resources available. The minimum and maximum inline offset are 984 ft, and 30839 ft, respectively. The data do not have crossline offset because they were regularized by using an azimuth moveout (AMO) algorithm (Biondi et al., 1998). The frequency content of the data ranged between 5 Hz and 35 Hz, with 20 Hz being the dominant frequency.

THE 3-D HESSIAN MATRIX

Figure 5.2 shows two different slices through the diagonal of the Hessian matrix for the 3-D target-zone cube. Dark gray represents areas with low values, and light gray represents areas with high values. Note the complexity of the focusing and defocusing of the seismic energy produced by the rugosity of the bottom of the salt. Also notice that the left side has values of the diagonal of the Hessian that are higher than everywhere else in the target area. This is not surprising since the Green's functions that contribute to this part of the image do not propagate through the salt.

I created a model with 72 point scatterers and convolved it with the 3D Hessian matrix to see the 3-D effect of the presence of the salt body on the PSF. Figure 5.3 shows the convolution result for two different views of the 3-D cube. The spread of the energy caused by the 3-D geometry of the salt body is clearly non-stationary. The PSF is 3-D, and as we showed in chapter 3, it contains information about the resolving power of our seismic imaging system. Note that the resolution in the crossline direction is poorer than that in the inline direction (the PSF are more elongated in the crossline than in the inline direction in Figure 5.3). This is a result of the limited data coverage in the crossline direction.

The target zone contains 726000 points ($nx = 120, ny = 50, nz = 121$), and the number of off-diagonal terms computed per row 9450 ($na_x = 15, na_y = 21, na_z = 30$). The Hessian matrix had around seven billion (10^9) elements in total. Because of the large computation effort that would be required, the subsurface-offset dimension

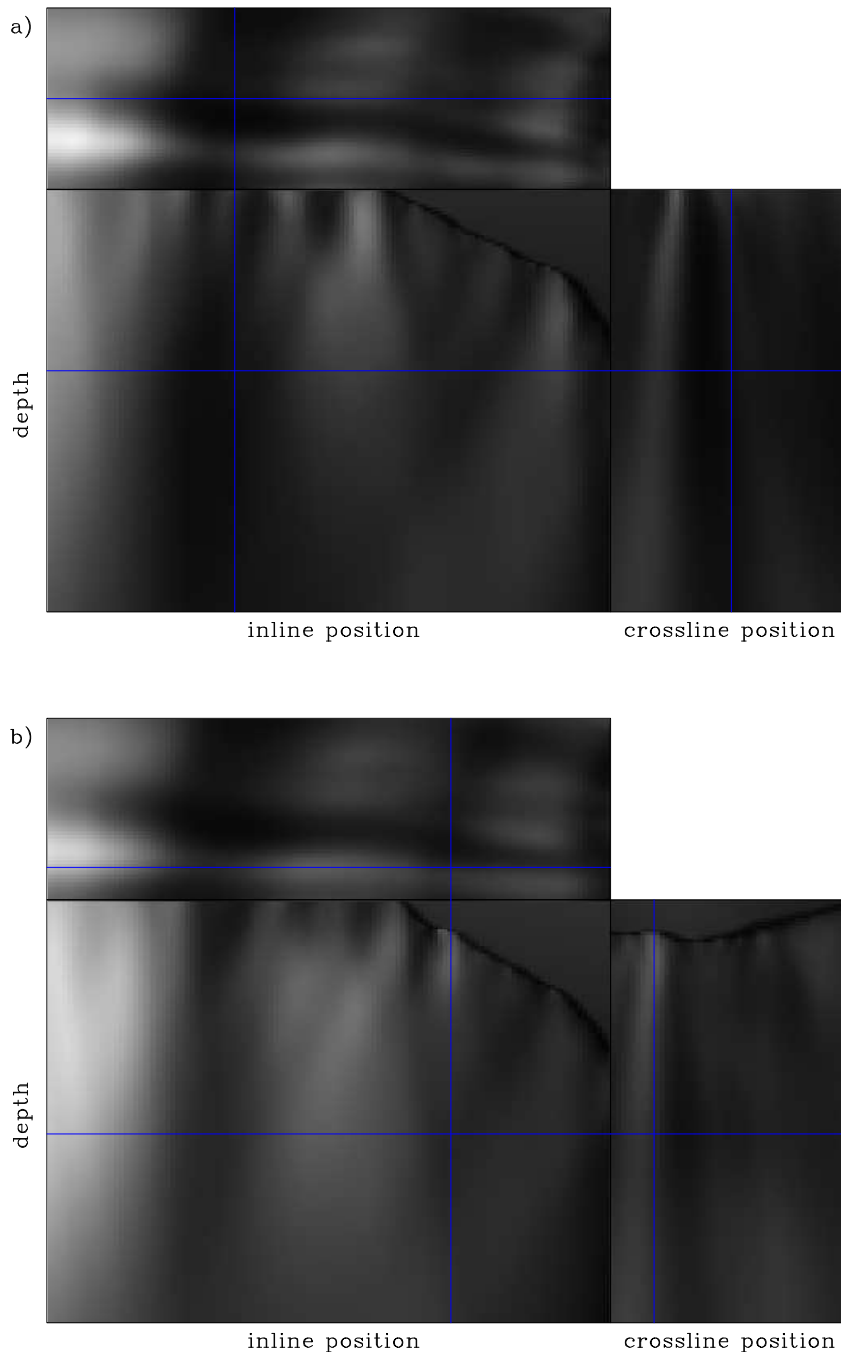


Figure 5.2: Diagonal of the Hessian matrix of the 3-D Gulf of Mexico data at two different locations in the target area. The low-illumination areas are dark gray, and high-illumination areas are light gray `Field-data/. bpgom-LtL-diag`

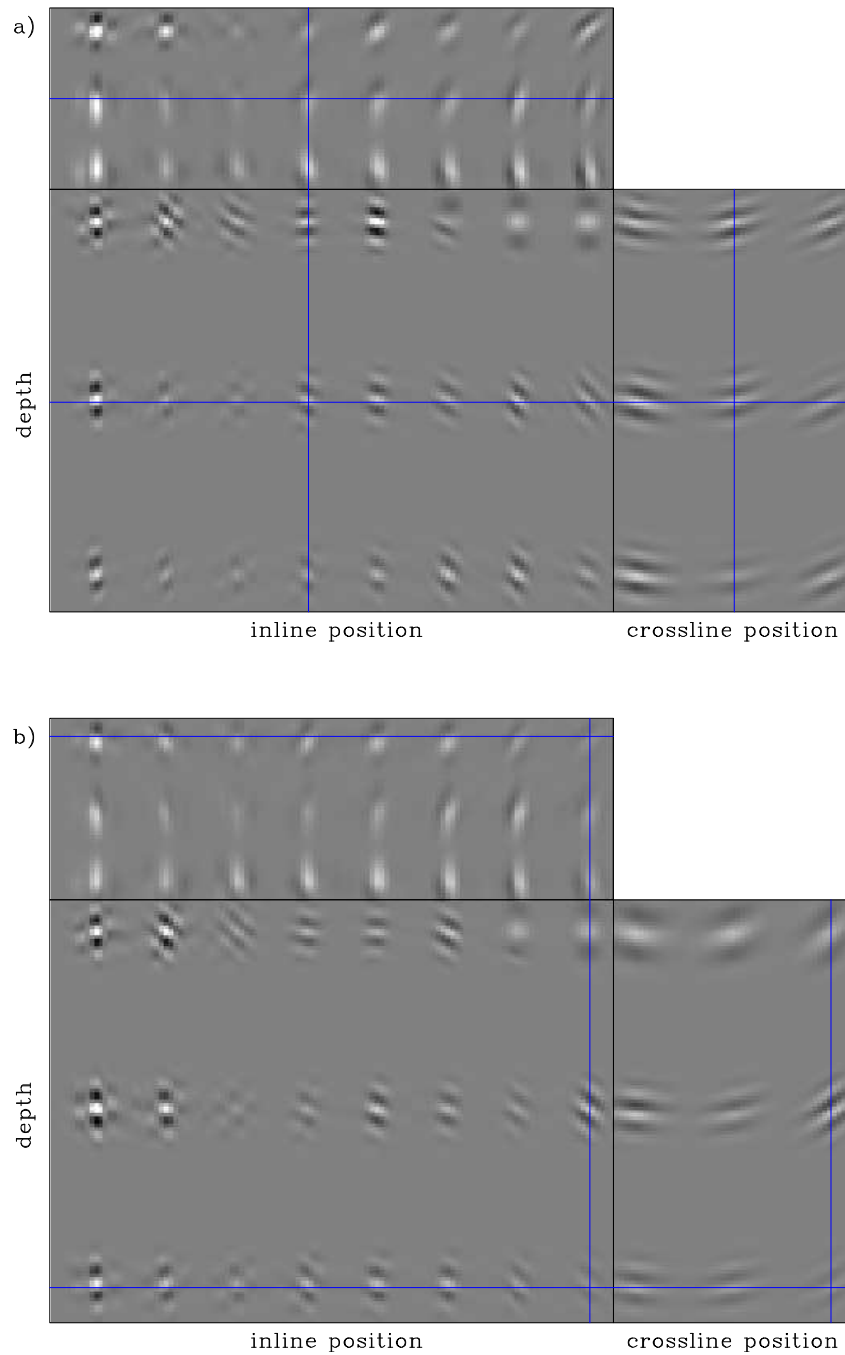


Figure 5.3: Convolution of the 72-point-scatterer model with the 3-D Hessian matrix at two different locations in the target area. Notice the non-stationarity of the PSF.

Field-data/. bpgom-LtL-offdiag-damp

was not included in the computation of the Hessian. I show in a later section that the inversion can still be regularized in the prestack image domain by making two approximations to the Hessian matrix.

The 3-D Hessian was computed by using a 32-nodes Sun cluster with two Opteron CPUs and 8 GB of memory per node. One important approximation that allowed the computation in our academic environment was the subsampling of the frequency axis (chapter 3). I used just 11 frequencies to compute the Green's functions for calculating the 3-D Hessian. The frequency band was chosen between 10 and 31 Hz, with a sampling interval of 2 Hz. The frequency sampling was fine enough to avoid contamination from wrap-around artifacts in the off-diagonal terms of the Hessian matrix (Figure 5.3).

The absence of crossline offset (after the AMO regularization) reduces the computational cost of the 3-D Hessian by removing the crossline receiver-loop in algorithm 4 (chapter 3). It also reduces the memory requirements since there is no need to compute crosscorrelations of sources and receivers Green's functions among crosslines. This makes it possible to calculate the 3-D Hessian with the Green's functions corresponding to just one crossline (in the data space) in memory at a time, which adds to the computational cost savings.

INVERSION IN THE POSTSTACK IMAGE DOMAIN

Inversion with 2-D Point Spread Functions (a_x, a_z)

Here I solve the linear system in equation 2.10 by using the method of conjugate gradients. The right-hand-side vector is the migrated image at zero subsurface offset (Figures 5.4a and 5.5a show two different views of the migration cube). The Hessian matrix contains only 2-D PSFs ($na_x = 15, na_y = 1, na_z = 30$), thus implying there is no correlation between neighboring points in the crossline direction. This assumption decreases the size of the Hessian matrix by an order of magnitude.

Two slices through the results of the inversion with the 2-D PSF ($na_x = 15, na_y =$

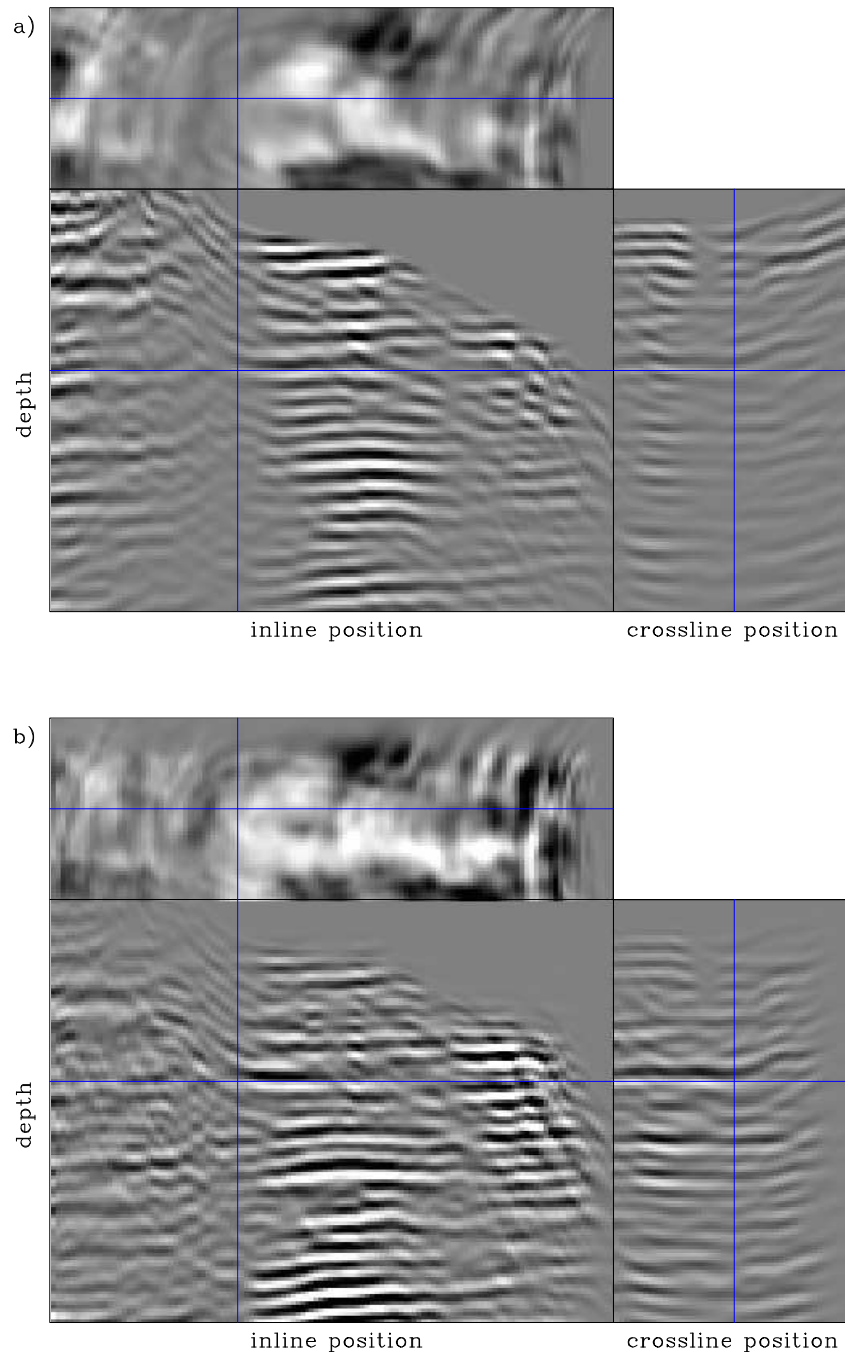


Figure 5.4: Zero subsurface-offset image of the 3-D Gulf of Mexico data: a) 3-D shot profile migration, and b) 3-D inversion in the poststack-image domain with 2-D PSFs. Notice the improved balance and resolution in the inversion image.

Field-data/. bpgom-inv-xz

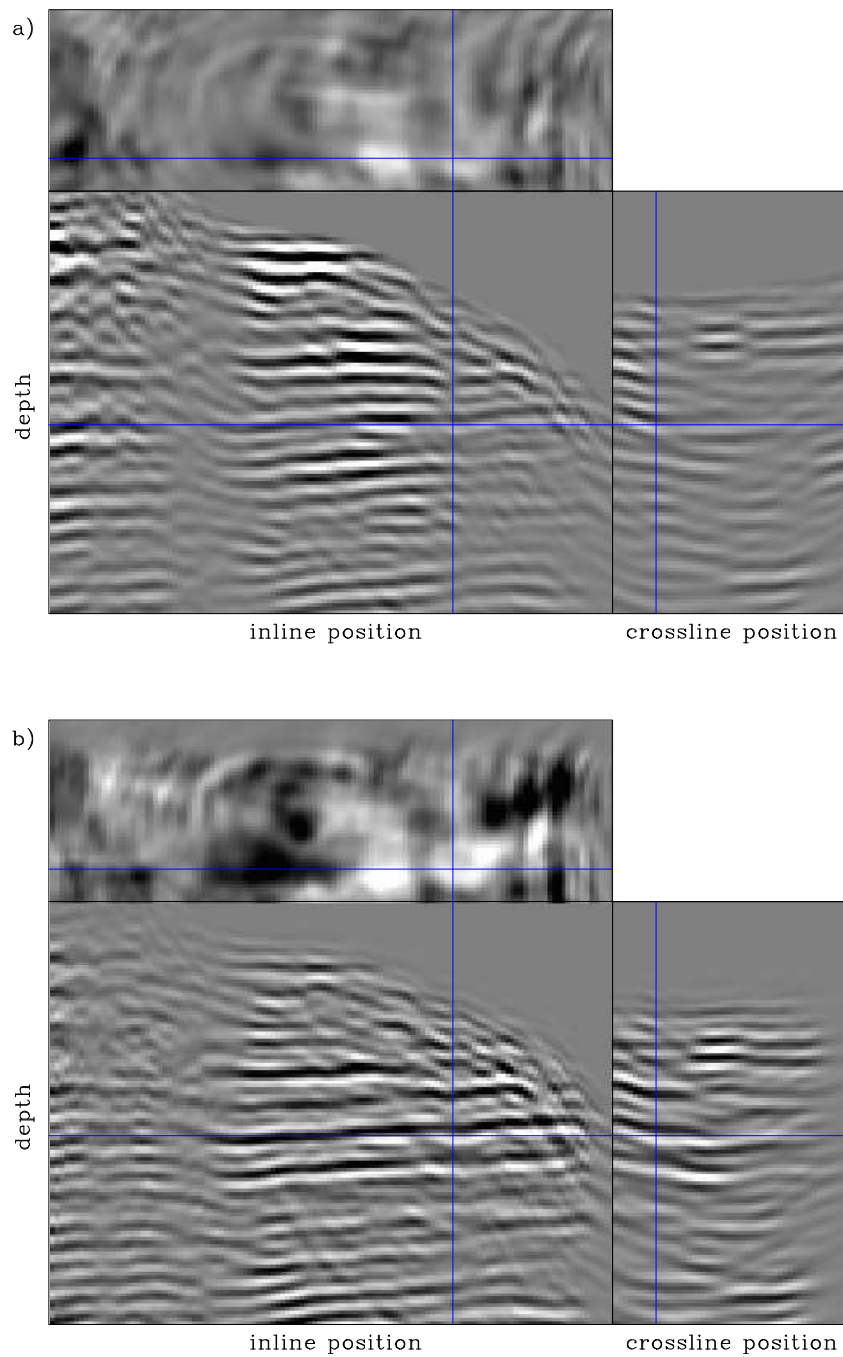


Figure 5.5: Zero subsurface-offset image of the 3-D Gulf of Mexico data: a) 3-D shot profile migration, and b) 3-D inversion in the poststack-image domain with 2-D PSFs. Notice the improved balance and resolution in the inversion image.

Field-data/. bpgom-inv-xz1

1, $na_z = 30$) are shown in Figures 5.4b and 5.5b; its benefits are evident compared to the migrations in Figures 5.4a, and 5.5a. The choice of the regularization parameter $\varepsilon = 0.1$ decreases the residuals and stabilizes the inversion.

Overall, the inversion with the 2-D PSF has more balanced amplitudes than does the migration, allowing continuation of the reflector inside the shadow zones. It also reduces some of the migration smiles, specially in the inline direction. The reflectors gain vertical and horizontal resolution, making them more interpretable. Improving the coherence of the events in the inline direction also improves the coherence in the crossline direction. However, no resolution is gained in this dimension, since the spread in the crossline is not included in the Hessian matrix.

Inversion with 3-D Point Spread Functions (a_x, a_y, a_z)

Figure 5.3 shows that the PSFs are 3-D, with larger spread in the crossline than in the inline direction. As a consequence, the migration result lacks resolution in the crossline dimension (Figures 5.4a and 5.5a), and the inversion with 2-D PSFs does not improve resolution in this direction (Figures 5.4b and 5.5b). Inversion has the potential to increase the crossline resolution if the 3-D PSFs are used.

To illustrate the previous idea, I used the image with 72 point scatterers (Figure 5.3). In this example, as in the 32-point-scatterer model shown in chapter 4, the operator used to create the input image is the same as that used in the inversion. Figure 5.6 shows the comparison between the inversion with the 2-D PSF, where the number of off-diagonal terms in the three directions is $(na_x = 15, na_y = 1, na_z = 30)$ (Figure 5.6a), and the inversion with the 3-D PSF, where the number of off-diagonal terms in the three directions is $(na_x = 15, na_y = 21, na_z = 30)$ (Figure 5.6b). The inversion with the 2-D PSF reduces the spread in the inline and depth directions but not in the crossline direction, whereas the inversion with the 3-D PSF reduces the spread in all the directions.

This improvement in the image is not without cost; adding the PSF in the crossline dimension increases the Hessian matrix size significantly. Moreover, the increased size

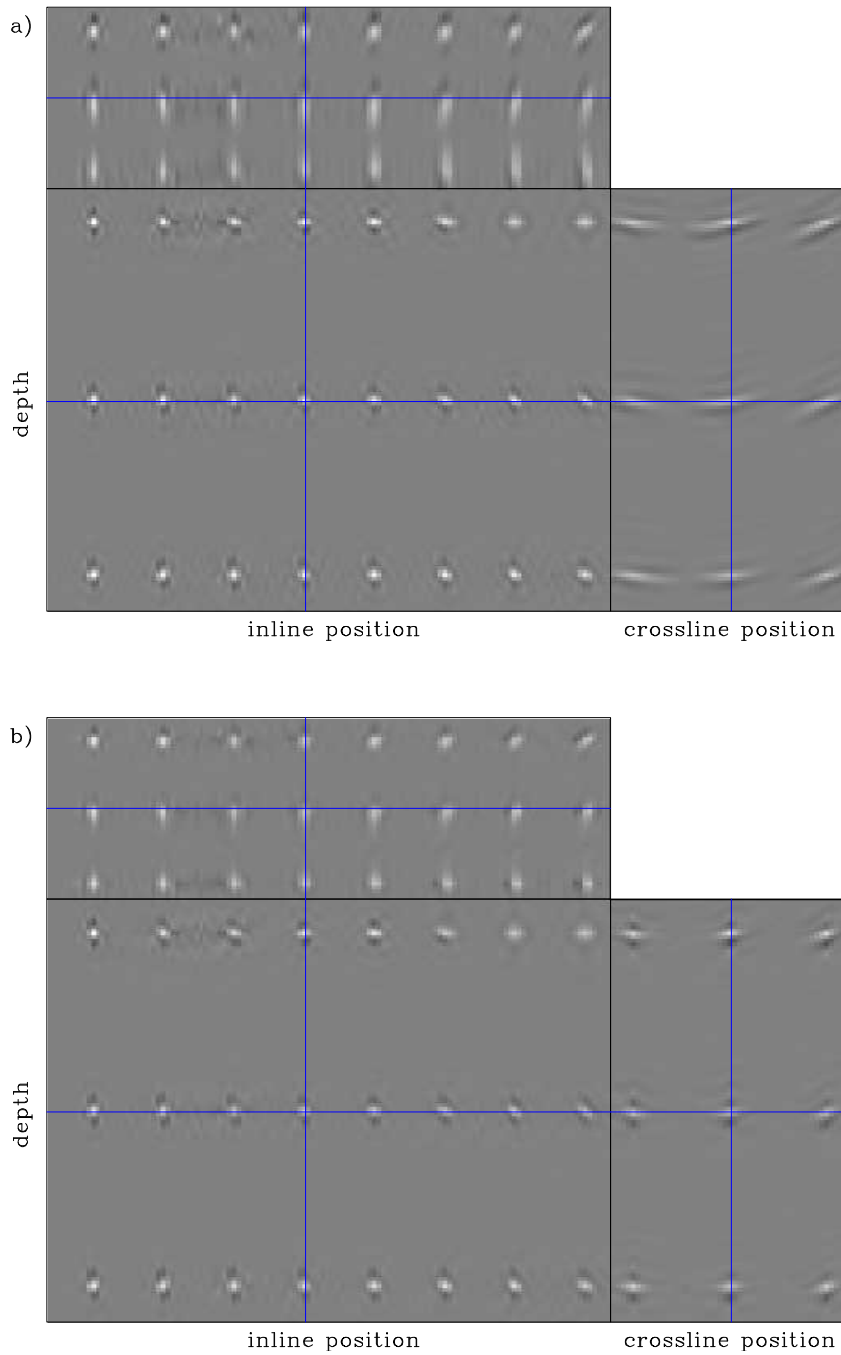


Figure 5.6: 3-D inversion in the poststack-image domain of the image in Figure 5.3a, a) with the 2-D PSF ($na_x = 15, na_y = 1, na_z = 30$), and b) with the 3-D PSF ($na_x = 15, na_y = 21, na_z = 30$). Compare with the input image in Figure 5.3a.

Field-data/. bpgom-LtL-offdiag-invclamp

of the Hessian makes the inversion more susceptible to error (Press et al., 1992; Gill et al., 1981), specially when the approximations used to compute the Green functions and the migration do not fully match the way seismic waves propagate through the earth, as they never do. Figure 5.7 shows a comparison of the inversion with the 2-D versus the 3-D PSF, where the right-hand-side vector is the migrated image at zero subsurface offset (Figures 5.4). Note in Figure 5.7b how adding the crossline spread creates instabilities in the inversion result.

INVERSION WITH REGULARIZATION IN THE PRESTACK IMAGE DOMAIN

When imaging under complex salt structures, it is useful to compute image gathers in the subsurface offset or the reflection and azimuth angle. Depending on the geometry of the salt the angle gathers can have illumination gaps; a good regularization of the wave-equation inversion can be to extend the image from well-illuminated to poorly illuminated angles (chapter 2 and chapter 4). I demonstrated the validity of this approach in chapter 4 in 2-D, by using the Sigsbee2B model. In this section, I apply it to the inversion of the 3-D Gulf of Mexico data. I limit the subsurface offset to the inline direction, and the angle to the reflection angle due to limited computational resources. The methodology presented here can be generalized to crossline subsurface offset and azimuth angle.

To solve the inversion problem with a model space that contains the subsurface-offset, I had to make two approximations, mainly due to computational constrains. The first is to assume the diagonal of the Hessian to be constant in the subsurface-offset dimension at each (x, y, z) point. This approximation is reasonable, since in the Sigsbee model (Figure 3.19) we saw that the Hessian varies smoothly in the subsurface-offset dimension (side panel). The second is to compute the Hessian matrix with no off-diagonal terms in the subsurface-offset dimension. This approximation assumes there is not spread in the subsurface offset dimension at each (x, y, z) point, which can be too strong of an assumption especially in the shadow zones (Figure 3.20).

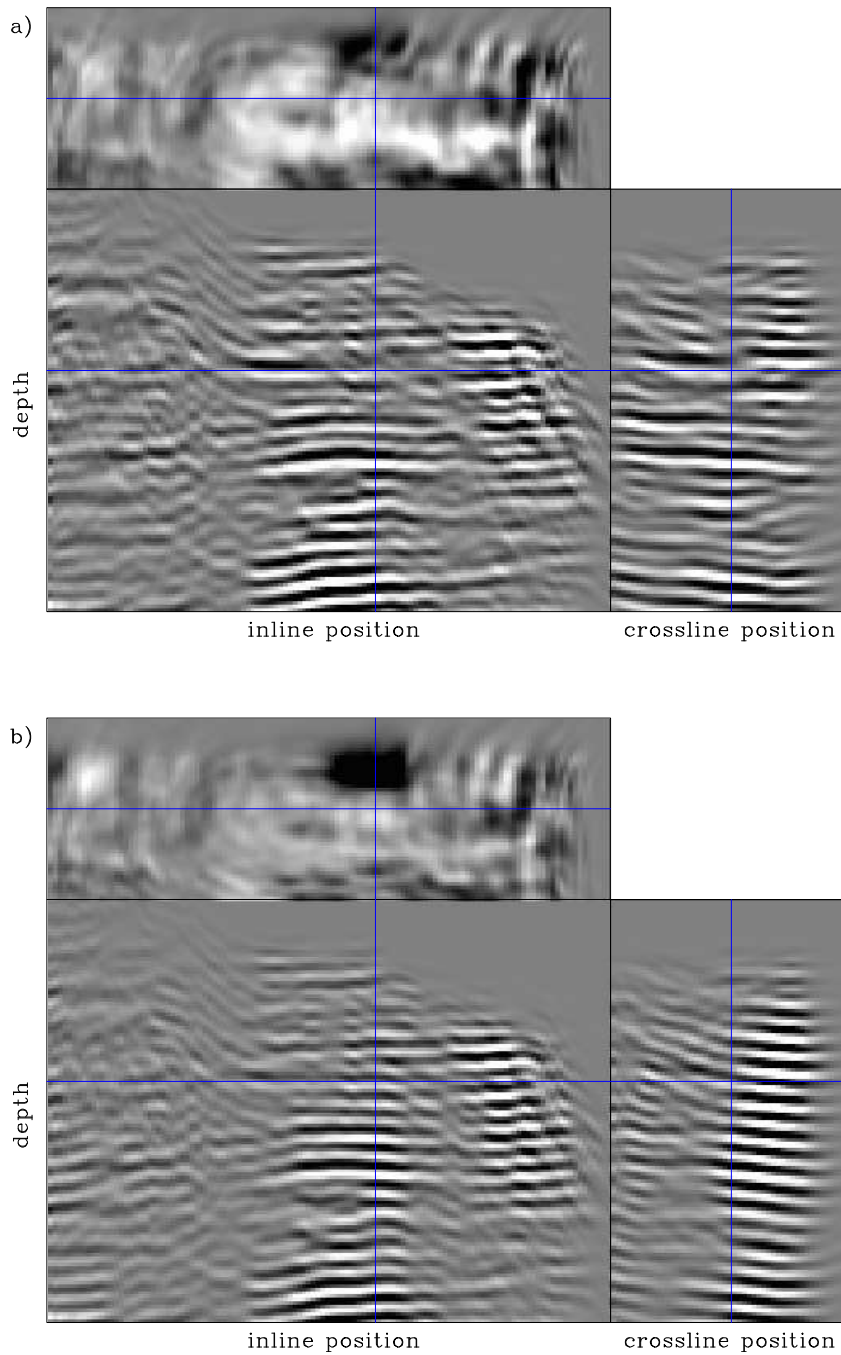


Figure 5.7: Zero subsurface-offset image of the 3-D Gulf of Mexico data: a) 3-D inversion in the poststack-image domain with the 2-D PSFs, b) 3-D inversion in the poststack-image domain with the 3-D PSFs. Notice the instability of the inversion when the 3-D PSFs are used. `Field-data/. bpgom-inv-xyz`

Since the number of computed elements of the Hessian matrix is directly related to the cost of the method, the impact of these or other possible approximations should be the object of future research.

The expansion in the dimensionality of the model space increases the cost of the inversion by a order of magnitude. In the next numerical experiments the Hessian matrix contains only the 2-D PSF ($na_x = 15, na_y = 1, na_z = 30$), and the model space is 4-D, with the extra dimension being the subsurface offset.

Figure 5.8 shows two different offset gathers (side panel) corresponding to a crossline position in the 4-D migration cube. Note how the energy is not focus at zero subsurface offset, meaning that the angle coverage is limited. The corresponding images after an offset-to-angle transformation by slant stack (Sava and Fomel, 2003) are shown in Figure 5.9. Notice the narrow range and the irregularity of the angle illumination, especially in the angle gather corresponding to the shadow zone (Figure 5.9b).

Figure 5.10 shows the image obtained by solving the linear system in equation 2.16 in the subsurface-offset domain, with differential semblance as the regularization operator and $\varepsilon = 0.5$ (equation 2.19). The front panel (to the left) shows the zero subsurface offset, and the side panel (to the right) shows a subsurface-offset gather. Compared to the result in Figure 5.8, notice how the amplitudes have been balanced everywhere, and the increase in vertical and lateral resolution. Also, time the reflectors have been continued into the shadow zone. As expected from the regularization with the differential semblance operator, the image is also more concentrated around zero subsurface-offset.

Figure 5.11 shows the inverted images in Figure 5.10 after an offset-to-angle transformation. Comparing this result with the migration (Figure 5.9), we see that the inversion plus regularization equalizes the amplitudes in the angle gathers, filling the illumination gaps in the shadow zone.

The last two figures, Figures 5.12 and 5.13, show the comparison of the angle-stack

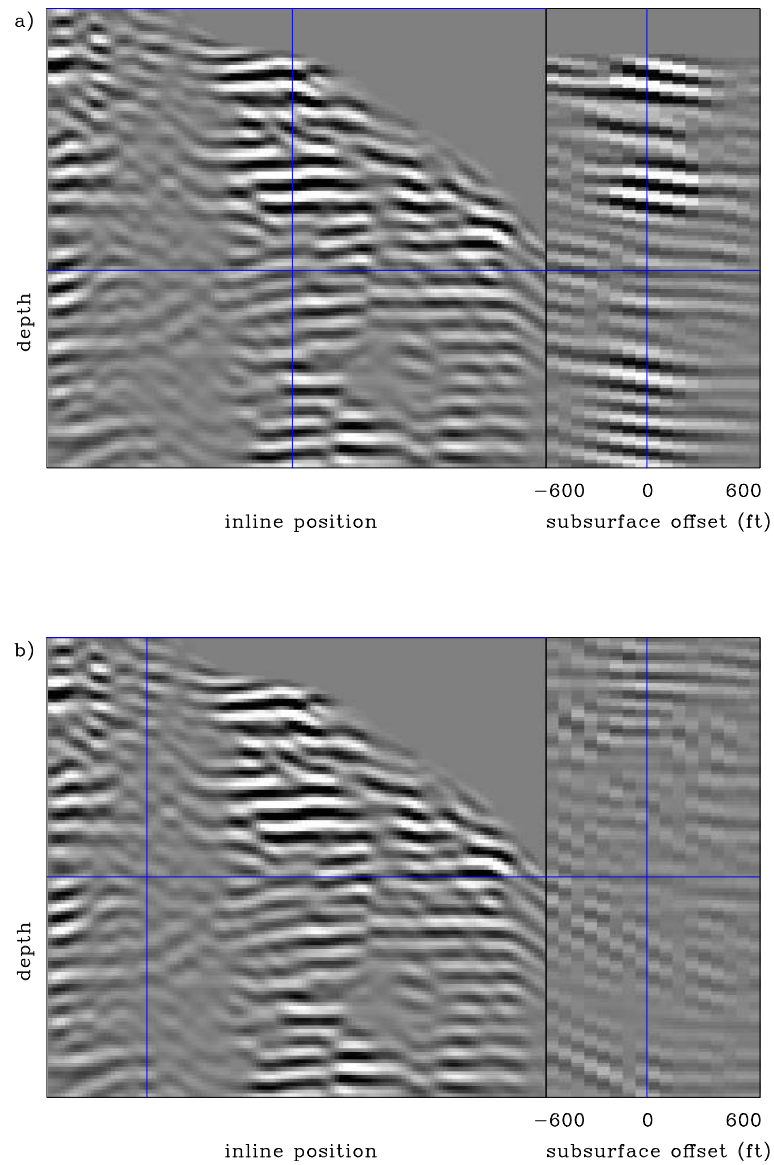


Figure 5.8: Migrated image in the subsurface-offset domain. The figure shows two different offset gathers (side panel) corresponding to a crossline position of the 3-D migration. `Field-data/. bpgom-mig-off`

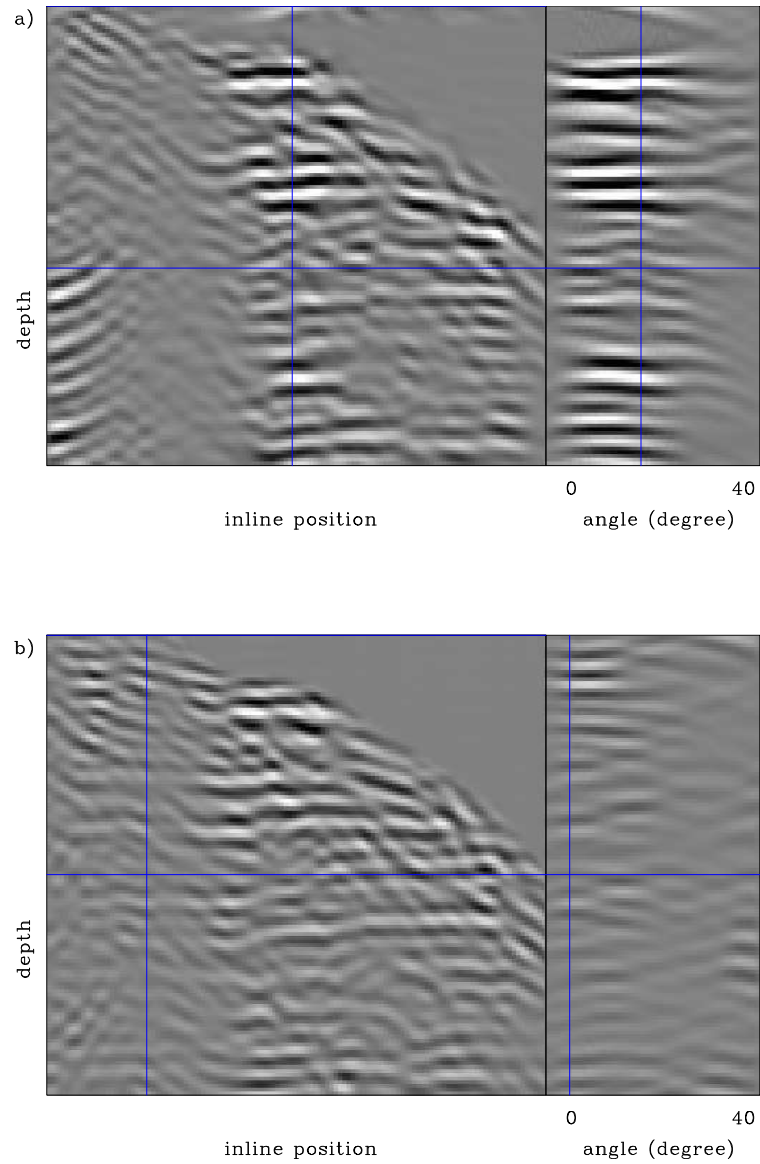


Figure 5.9: Migrated image in the reflection-angle domain after offset-to-angle transformation. The figure shows two different reflection-angle gathers (side panel), and the corresponding angle sections (front panel), at the same crossline position of the 3-D migration as in Figure 5.8. `Field-data/. bpgom-mig-ang`

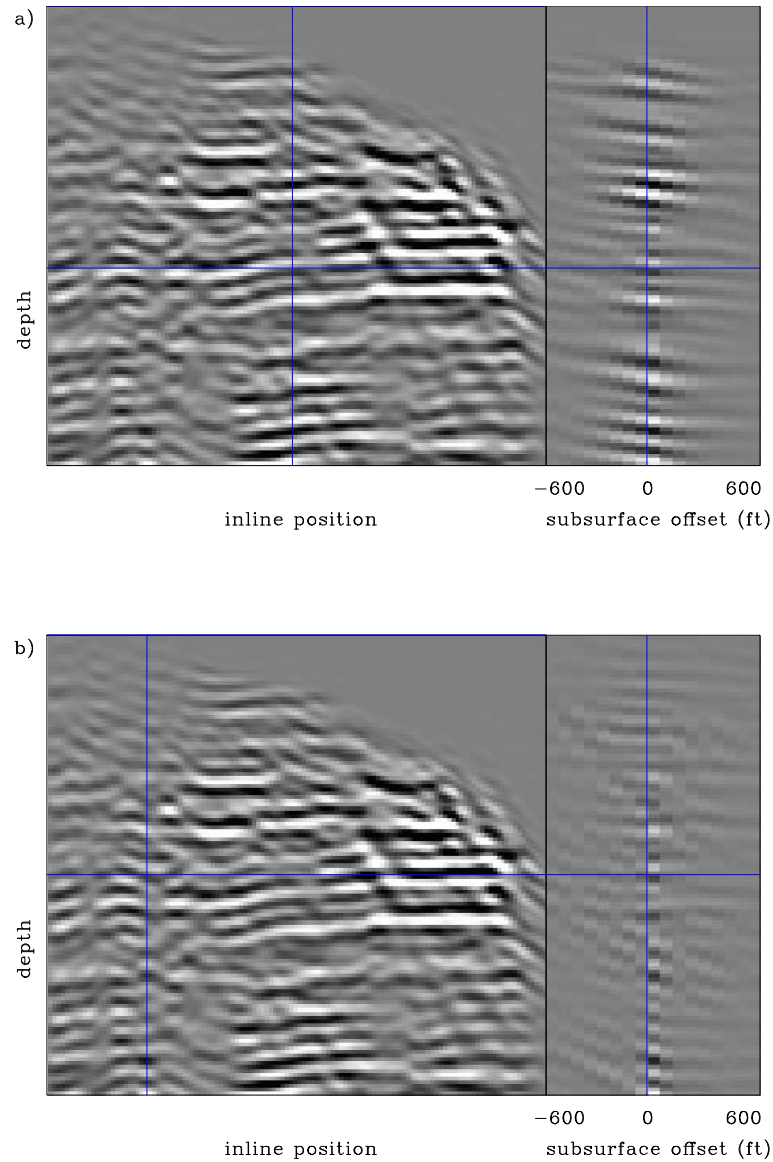


Figure 5.10: Inverted image in the subsurface-offset domain with the differential semblance as the regularization operator and $\varepsilon = 0.5$. Compare with Figure 5.8, and notice that the amplitudes have been balanced; the image is also more concentrated around zero subsurface offset. `Field-data/. bpgom-inv-off`

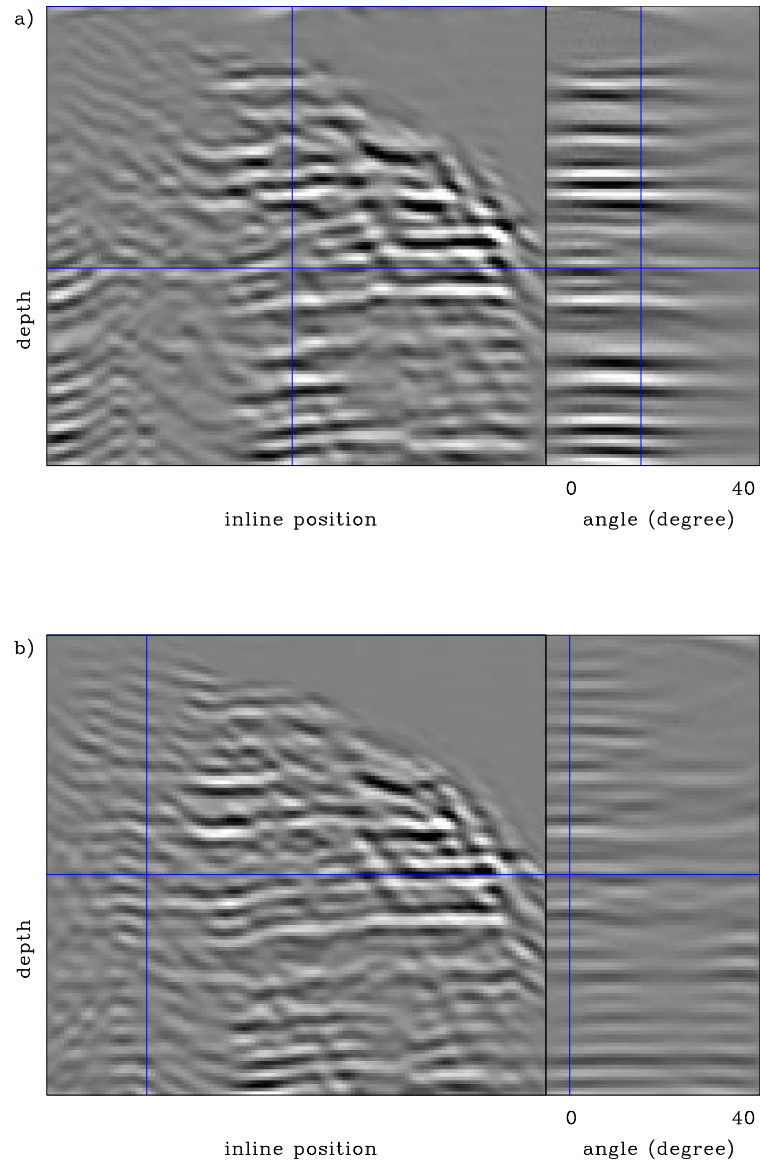


Figure 5.11: Inverted image in the subsurface-offset domain, after an offset-to-angle transformation. Compared to the migration in Figure 5.9, note how the inversion plus regularization equalizes the amplitudes in the angle gathers.

Field-data/. bpgom-inv-ang

of the migration with the angle-stack of the inversion for three different regularization parameters. Whereas they couldn't be done in the migration results, some of the reflectors can be traced almost entirely through the shadow zones in the inversion results. As the regularization parameter ε increases, some of the noise is reduced, but the effectiveness of the inversion is also reduced. The changes in the quality of the inverted image with the regularization parameter suggests that a variable regularization parameter should improve the regularized inversion results. A variable regularization usually requires interpretation, which makes the result model-dependent.

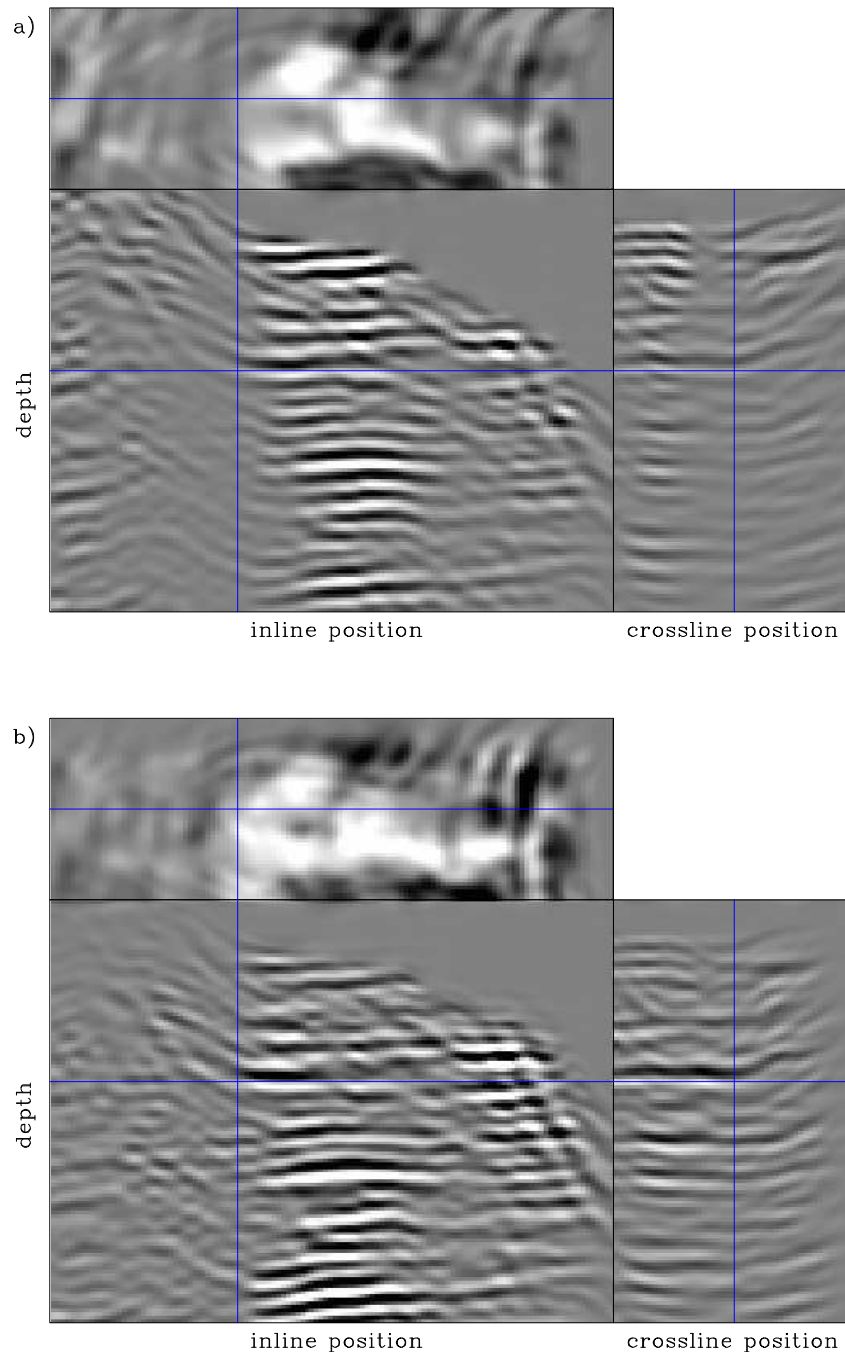


Figure 5.12: Comparison of the angle-stack of a) the migration, with b) the inversion in the subsurface-offset domain, after an offset-to-angle transformation with regularization parameter $\varepsilon = 0.5$. `Field-data/. bpgom-inv-stack`

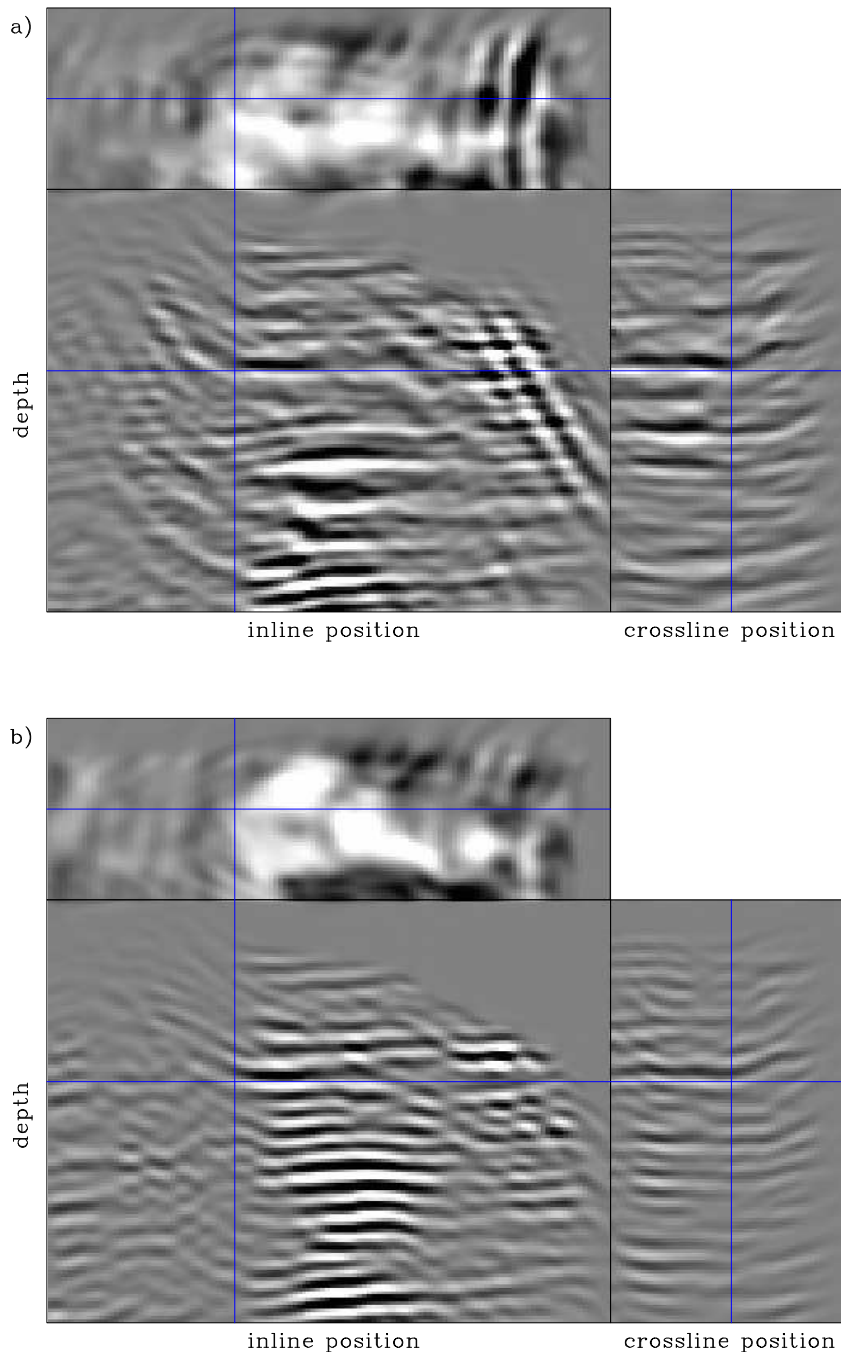


Figure 5.13: Comparison of the angle-stack of the inversion in the subsurface-offset domain, after an offset-to-angle transformation with regularization parameter a) $\varepsilon = 0.01$, and b) $\varepsilon = 10$ `Field-data/. bpgom-inv-stack1`

Chapter 6

Conclusions

Imaging under salt bodies challenges the technology used in modern hydrocarbon exploration. The shape and strong velocity contrast between the salt and the surrounding sediments, create irregularities in the seismic energy that “illuminates” sub-salt targets. This thesis tackles the irregular illumination problem with least-squares wave-equation inversion that makes use of a physically-inspired regularization.

My main contribution is the development of a methodology to explicitly compute the least-squares Hessian matrix and solve the regularized wave-equation inversion in image space.

The rows of the least-squares Hessian matrix are the point spread functions (PSFs) of the imaging system. For seismic imaging, they are non-stationary as a consequence of the complexity of the velocity model and the acquisition geometry. This is shown in chapter 3 by using the Sigsbee2B synthetic model, and later in chapter 5 with a 3-D example using a field data set from the Gulf of Mexico.

The key to making the method practical is the optimization of the algorithm used to compute the Hessian matrix. I show in chapter 3 the steps to achieve computational savings of five orders of magnitude or more compared to direct implementation, by considering the sparsity and structure of the Hessian matrix, the acquisition geometry, and the frequency sampling. Computing the Hessian requires no further compromises

about the complexity of the velocity model or the acquisition geometry, which is important to obtain a good inversion result in complex areas.

The Hessian computation and the wave-equation inversion can be posed in a target-oriented fashion. This allows to spend the computational efforts at the reservoir level, where the accurate imaging of the reflectors is more important. The target-oriented approach is possible because the modeling/migration operators can be written in terms of Green's functions from the surface to a subsurface-target, and vice versa (chapter 2). Posing the methodology in a target-oriented fashion is critical for 3-D applications since otherwise the size of the Green's functions and the Hessian matrix would make the method impractical. In chapter 5, I show how the method works for a subsalt target using a 3-D field data set from the Gulf of Mexico.

The last two chapters (4 and 5) are mainly devoted to analyzing and illustrating the properties of wave-equation inversion. In chapter 4, I use the Sigsbee2B synthetic to illustrate the practical aspects required to make the inversion work, especially when the Hessian matrix is ill-conditioned. I conclude that the differential semblance in the subsurface-offset domain, although it is more expensive, can improve the continuity of the reflectors into the shadow zones with a higher signal-to-noise ratio than can regularization in the poststack image-domain (zero subsurface offset). This does not mean that the regularization in the poststack image-domain cannot be an economical alternative for 3-D data, as is shown with field data in chapter 5.

Another point made in chapter 5 is that the dimensionality of the PSFs (rows of the Hessian matrix) can influence the spatial resolution of the image after inversion. I show, using a synthetic with 72-point-scatterers, the increase of resolution in the crossline direction when 3-D PSFs are used instead of 2-D PSFs. Unfortunately, the inversion of the migrated image of the field data becomes unstable when 3-D PSFs are used. The lack of crossline coverage is an important part of the problem. One way to improve this result is to include more data in the crossline direction for the migration, and compute the corresponding Green's functions to the target. This makes the numerical experiment more expensive, but it can be solved with more computational resources.

The inversion becomes unstable when noise in the image does not fit the model. In chapter 4 I show that salt-related multiples not taken into account while computing the Green's functions can obscure the weak signal that exists inside the shadow zones. In appendix B I give a solution that reduces the multiples before inversion. This can be dangerous since the signal can be degraded during noise removal, but it proved to be a good solution for the inversion of Sigsbee2B data.

Appendix A

Angle-domain Hessian

Biondi and Tisserant (2004) define an image-space transformation from subsurface offset to reflection angle and azimuth angle as

$$\mathbf{m}(\mathbf{x}, \Theta) = \mathbf{S}_{\mathbf{h} \rightarrow \Theta} \mathbf{m}(\mathbf{x}, \mathbf{h}), \quad (\text{A.1})$$

where $\Theta = (\theta, \alpha)$, with γ the reflection angle and θ the azimuth angle, respectively, and $\mathbf{S}_{\mathbf{h} \rightarrow \Theta}$ is the adjoint of the angle-to-offset transformation operator (slant stack).

Substituting the prestack migration image (subsurface-offset-domain) in equation 2.11 into equation A.1, we obtain the expression for the prestack migration image in the angle-domain,

$$\begin{aligned} \mathbf{m}(\mathbf{x}, \Theta) &= \mathbf{S}_{\mathbf{h} \rightarrow \Theta} \mathbf{L}' \mathbf{d}(\mathbf{x}_s, \mathbf{x}_r; \omega) \\ &= \mathbf{S}_{\mathbf{h} \rightarrow \Theta} \sum_{\omega} \sum_{\mathbf{x}_s} \sum_{\mathbf{x}_r} \mathbf{G}'(\mathbf{x} + \mathbf{h}, \mathbf{x}_s; \omega) \mathbf{G}'(\mathbf{x} - \mathbf{h}, \mathbf{x}_r; \omega) \mathbf{d}(\mathbf{x}_s, \mathbf{x}_r; \omega) \end{aligned} \quad (\text{A.2})$$

The synthetic data can be modeled (as the adjoint of equation A.2) by the chain of linear operator \mathbf{L} and the angle-to-offset transformation operator acting on the

model,

$$\begin{aligned} \mathbf{d}(\mathbf{x}_s, \mathbf{x}_r; \omega) &= \mathbf{L}\mathbf{S}_{\Theta \rightarrow \mathbf{h}}\mathbf{m}(\mathbf{x}, \Theta) \\ &= \sum_{\mathbf{x}} \sum_{\mathbf{h}} \mathbf{G}(\mathbf{x} - \mathbf{h}, \mathbf{x}_r; \omega) \mathbf{G}(\mathbf{x} + \mathbf{h}, \mathbf{x}_s; \omega) \mathbf{S}_{\Theta \rightarrow \mathbf{h}}\mathbf{m}(\mathbf{x}, \Theta), \end{aligned} \quad (\text{A.3})$$

The quadratic cost function is

$$\begin{aligned} S(\mathbf{m}) &= \frac{1}{2} \sum_{\omega} \sum_{\mathbf{x}_s} \sum_{\mathbf{x}_r} \|\mathbf{d} - \mathbf{d}_{obs}\|^2 \\ &= \frac{1}{2} \sum_{\omega} \sum_{\mathbf{x}_s} \sum_{\mathbf{x}_r} [\mathbf{d}(\mathbf{x}_s, \mathbf{x}_r; \omega) - \mathbf{d}_{obs}]' [\mathbf{d}(\mathbf{x}_s, \mathbf{x}_r; \omega) - \mathbf{d}_{obs}], \end{aligned} \quad (\text{A.4})$$

while its first derivative with respect to the model parameters $\mathbf{m}(\mathbf{x}, \Theta)$ is

$$\begin{aligned} \frac{\partial S(\mathbf{m})}{\partial \mathbf{m}(\mathbf{x}, \Theta)} &= \frac{1}{2} \sum_{\omega} \sum_{\mathbf{x}_s} \sum_{\mathbf{x}_r} \{ \mathbf{S}_{\mathbf{h} \rightarrow \Theta} \mathbf{G}'(\mathbf{x} - \mathbf{h}, \mathbf{x}_r; \omega) \mathbf{G}'(\mathbf{x} + \mathbf{h}, \mathbf{x}_s; \omega) [\mathbf{d}(\mathbf{x}_s, \mathbf{x}_r; \omega) - \mathbf{d}_{obs}] \\ &\quad + [\mathbf{d}(\mathbf{x}_s, \mathbf{x}_r; \omega) - \mathbf{d}_{obs}]' \mathbf{G}(\mathbf{x} - \mathbf{h}, \mathbf{x}_r; \omega) \mathbf{G}(\mathbf{x} + \mathbf{h}, \mathbf{x}_s; \omega) \mathbf{S}_{\Theta \rightarrow \mathbf{h}} \} \end{aligned} \quad (\text{A.5})$$

and its second derivative with respect to the model parameters $\mathbf{m}(\mathbf{x}, \Theta)$ and $\mathbf{m}(\mathbf{x}', \Theta')$ is the angle-domain Hessian

$$\begin{aligned} \mathbf{H}(\mathbf{x}, \Theta; \mathbf{x}', \Theta') &= \frac{\partial^2 S(\mathbf{m})}{\partial \mathbf{m}(\mathbf{x}, \Theta) \partial \mathbf{m}(\mathbf{x}', \Theta')} \\ &= \sum_{\omega} \sum_{\mathbf{x}_s} \sum_{\mathbf{x}_r} \mathbf{S}_{\mathbf{h} \rightarrow \Theta} \mathbf{G}'(\mathbf{x} + \mathbf{h}, \mathbf{x}_s; \omega) \mathbf{G}(\mathbf{x}' + \mathbf{h}', \mathbf{x}_s; \omega) \\ &\quad \times \mathbf{G}'(\mathbf{x} - \mathbf{h}, \mathbf{x}_r; \omega) \mathbf{G}(\mathbf{x}' - \mathbf{h}', \mathbf{x}_r; \omega) \mathbf{S}_{\Theta' \rightarrow \mathbf{h}'} \\ &= \mathbf{S}_{\mathbf{h} \rightarrow \Theta} \sum_{\omega} \sum_{\mathbf{x}_s} \sum_{\mathbf{x}_r} \mathbf{G}'(\mathbf{x} + \mathbf{h}, \mathbf{x}_s; \omega) \mathbf{G}(\mathbf{x}' + \mathbf{h}', \mathbf{x}_s; \omega) \\ &\quad \times \mathbf{G}'(\mathbf{x} - \mathbf{h}, \mathbf{x}_r; \omega) \mathbf{G}(\mathbf{x}' - \mathbf{h}', \mathbf{x}_r; \omega) \mathbf{S}_{\Theta' \rightarrow \mathbf{h}'} \\ &= \mathbf{S}_{\mathbf{h} \rightarrow \Theta} \mathbf{H}(\mathbf{x}, \mathbf{h}; \mathbf{x}', \mathbf{h}') \mathbf{S}_{\Theta' \rightarrow \mathbf{h}'}. \end{aligned} \quad (\text{A.6})$$

Chain of operators versus angle Hessian computation

Equation A.6 expresses the angle-domain Hessian as a chain of the offset-to-angle operator and the subsurface offset Hessian matrix. This implies that to implement the angle-domain wave-equation inversion using a conjugate gradient algorithm there is no need to explicitly compute the angle Hessian matrix. A possible drawback, however, is that, for each iteration, the offset-to-angle transformation needs to be performed.

A different strategy might be to explicitly compute the angle-domain Hessian matrix. This can be done by a simple manipulation the terms in equation A.6. Using the fact that $\mathbf{H}(\mathbf{x}, \mathbf{h}; \mathbf{x}', \mathbf{h}')$ is symmetric, we have

$$\mathbf{H}(\mathbf{x}, \Theta; \mathbf{x}', \Theta') = \mathbf{S}_{\mathbf{h} \rightarrow \Theta} \mathbf{H}(\mathbf{x}, \mathbf{h}; \mathbf{x}', \mathbf{h}') \mathbf{S}_{\Theta' \rightarrow \mathbf{h}'} \quad (\text{A.7})$$

$$= \mathbf{S}_{\mathbf{h} \rightarrow \Theta} (\mathbf{S}_{\mathbf{h}' \rightarrow \Theta'} \mathbf{H}(\mathbf{x}, \mathbf{h}; \mathbf{x}', \mathbf{h}'))'. \quad (\text{A.8})$$

In practice, equation A.8 takes the subsurface offset Hessian matrix and applies an offset-to-angle transformation, then transposes the resulting matrix and reapplies the same offset-to-angle transformation. This explicit angle Hessian matrix computation could be an expensive operation. Whereas it has the advantage of needing to be performed only once before starting the inversion process.

Appendix B

Salt-related multiple removal

Traditional data-space demultiple schemes dealing with either periodicity or differential moveout become ineffective in subsalt settings because the complex ray path makes periodicity harder to predict. Subsalt reflections usually appear only in the near offsets, making radon-type demultiple schemes ineffective. Sava and Guitton (2005) and Alvarez et al. (2007) demonstrated that primaries and multiples have different behavior in image space (subsurface-offset or reflection-angle), and that multiples can be adaptively subtracted from the migration in the image domain without significantly affecting the primaries.

Figure B.1 shows the migration in the reflection-angle domain. The front face corresponds to the image at 0° reflection angle, and the side face corresponds to the reflection-angle gather at a position inside the shadow zone ($x = 36800$ ft). Notice how multiples and primaries are well separated in the angle gather, where the multiples have a frowning shape and the primaries are flat. Figure B.2 shows the migration result in the same area but in the subsurface-offset domain. The front face corresponds to the image at zero subsurface offset, and the side face corresponds to the subsurface-offset gather at a position inside the shadow zone ($x = 36800$ ft). Since the primaries are illuminated at few reflection angles, their signature in the subsurface offset domain is an slanted line.

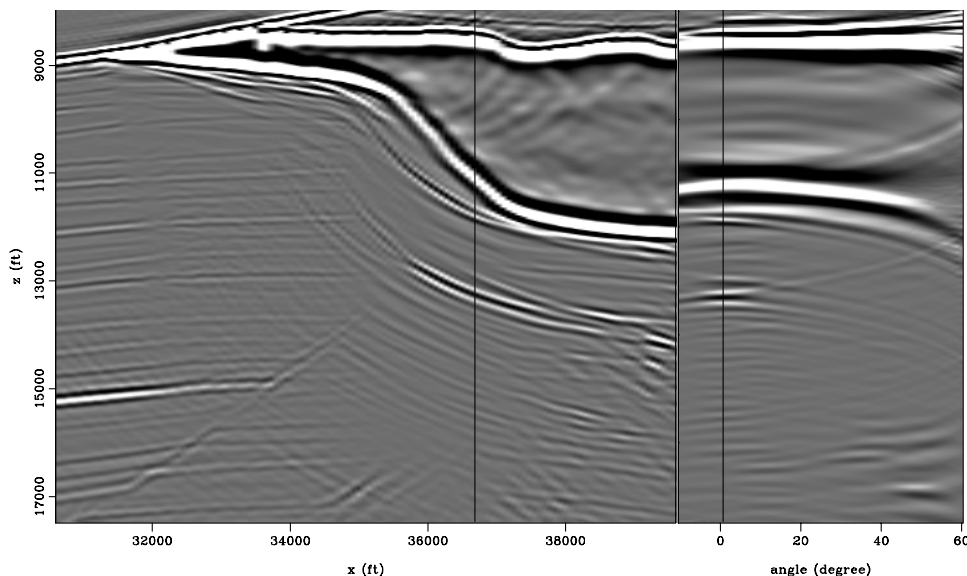


Figure B.1: Sigsbee shot-profile migration (reflection angle) using cross-correlation imaging condition. The front face corresponds to the image at 0° reflection angle, and the side face corresponds to the reflection-angle gather at $x = 36800$ ft position.

AppendixB/. migang1

The internal multiples are also illuminated at a very narrow range of angles. The bouncing at the dipping salt bottom makes the reflection angle of internal multiples decrease. Consequently, they appear as almost horizontal events in the subsurface offset gathers. However, in the x - z plane they show dips following the base of salt. These different dip patterns were used to attenuate the multiple amplitudes before inversion using a $k_x - k_h$ filter. As I show in chapter 5, this behavior of the multiples and primaries can also be found in field datasets.

I used a three-stage pre-processing strategy to attenuate the multiple energy. It included discriminating the multiple energy in the $k_x - k_h$ plane (to generate a model of the multiples); performing amplitude and phase correction of the discriminated multiples in a least-square sense; and subtracting them from the original data.

The discrimination of the multiple energy relies on the differences in dip patterns as described previously: multiples show up in the $k_x - k_h$ plane at low k_h and high

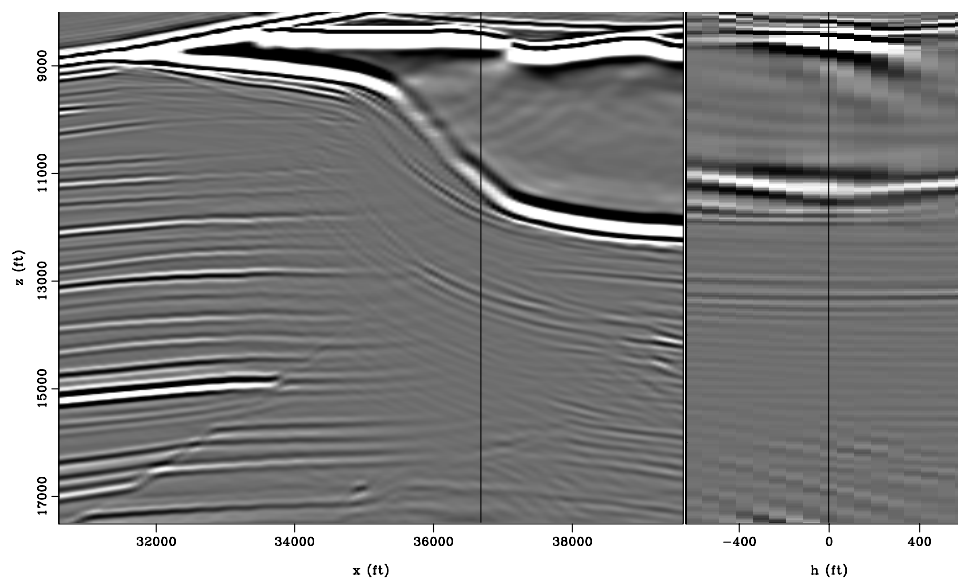


Figure B.2: Sigsbee shot-profile migration (subsurface-offset) using cross-correlation imaging condition. The front face corresponds to the image at zero subsurface-offset, and the side face corresponds to the subsurface-offset gather at $x = 36800$ ft. `AppendixB/. migoff1`

k_x , and primaries at high k_h and low k_x . Therefore, to build a model of the multiples I bandpassed the migration at every depth step. Figure B.3 shows a depth slice at $z = 14150$ ft of the migration in the $k_x - k_h$ plane, and Figure B.4 shows the result of bandpassing Figure B.3. The model for the multiples (Figure B.5) is obtained after subtraction of the filtered result (Figure B.4) from the migration (Figure B.3).

The impact on the primaries of the multiple-attenuation process can be ameliorated if the amplitude and phase of the obtained multiples are adjusted to minimize their differences from the original data in a least-squares sense. After this adjustment, I used an adaptive subtraction scheme that simultaneously adaptively matched the primaries and multiples with non-stationary filters computed in small patches (Alvarez et al., 2007).

After filtering, the multiples had been largely attenuated, making the migration image more suitable for inversion. Figure B.6 shows the filtered migration in the

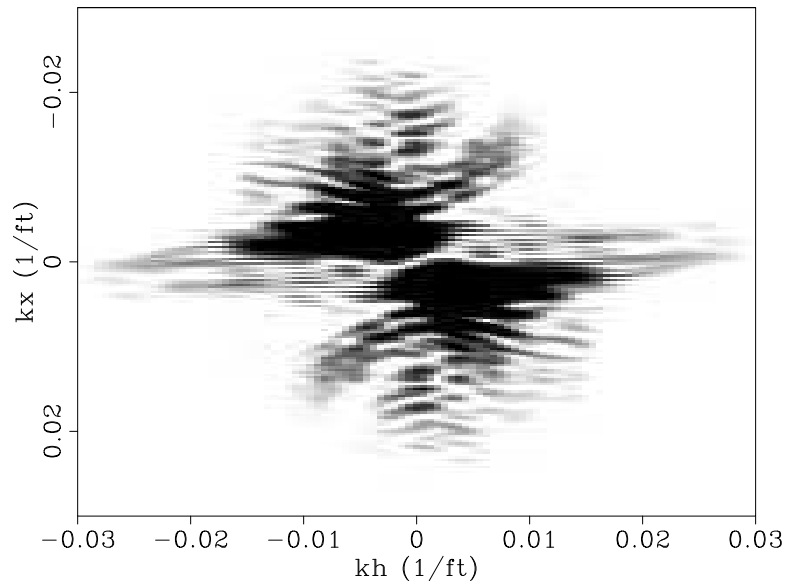


Figure B.3: Depth slice at $z = 14150$ ft of the migration in the $k_x - k_h$ plane. AppendixB/. not-filtered

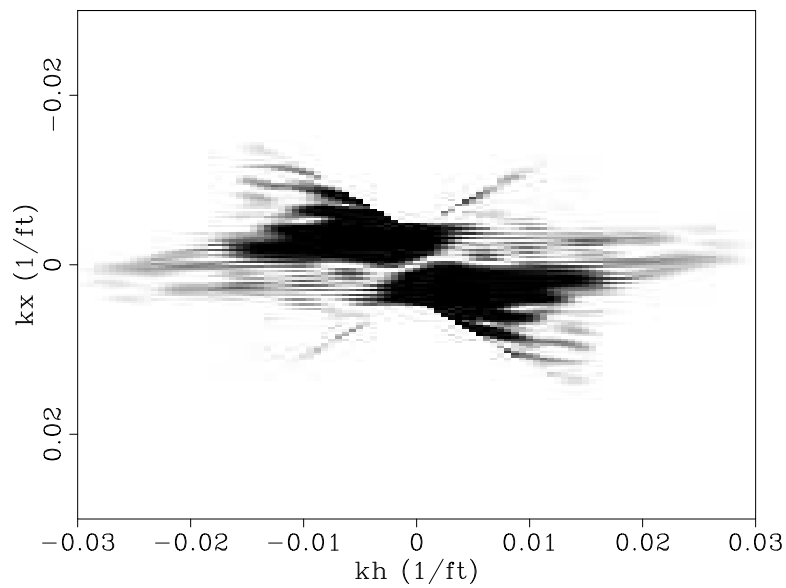


Figure B.4: Primaries after bandpassing the migration (Figure B.3) in the $k_x - k_h$ plane. AppendixB/. filtered

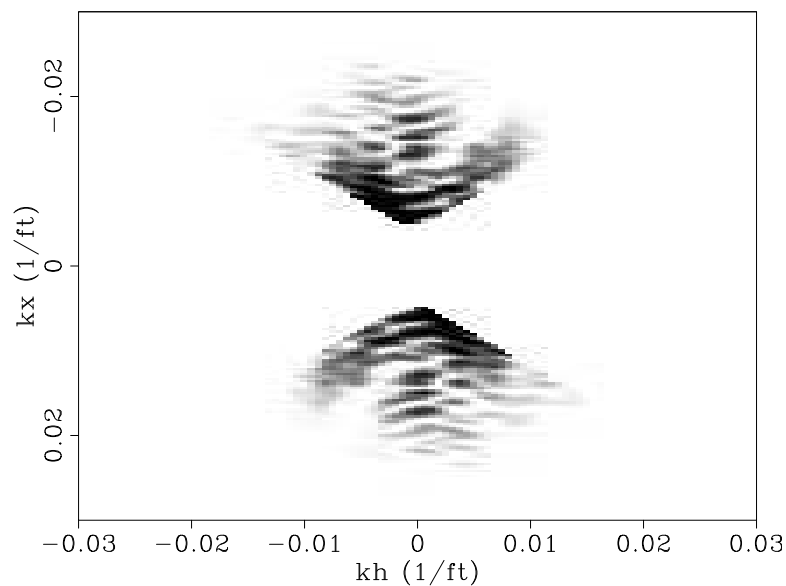


Figure B.5: The model for the multiples in the $k_x - k_h$ plane, obtained after subtraction of the filtered result (Figure B.4) from the migration (Figure B.3).
 AppendixB/. diff-filtered

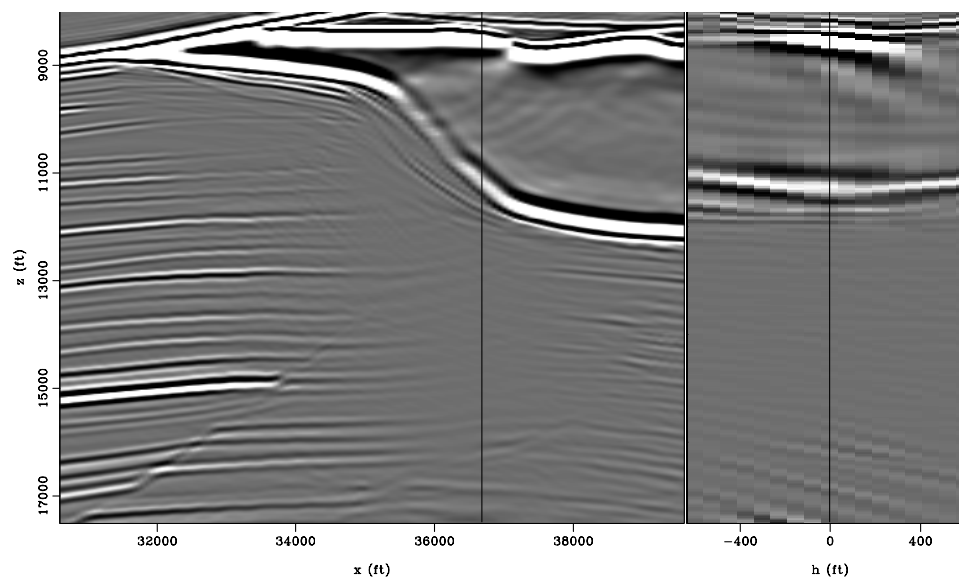


Figure B.6: Sigsbee shot-profile migration (subsurface-offset) using cross-correlation imaging condition. The front face corresponds to the image at zero subsurface-offset, and the side face corresponds to the subsurface-offset gather at $x = 36800$ ft.
 AppendixB/. migoff1-filt

subsurface-offset domain. As in Figure B.2 the front face corresponds to the image at zero subsurface offset, and the side face corresponds to the subsurface-offset gather at a position inside the shadow zone ($x = 36800$ ft). This result is corroborated in the angle domain (Figure B.7). The front face corresponds to the image at 0° reflection angle, and the side face corresponds to the reflection-angle gather at a position inside the shadow zone ($x = 36800$ ft).

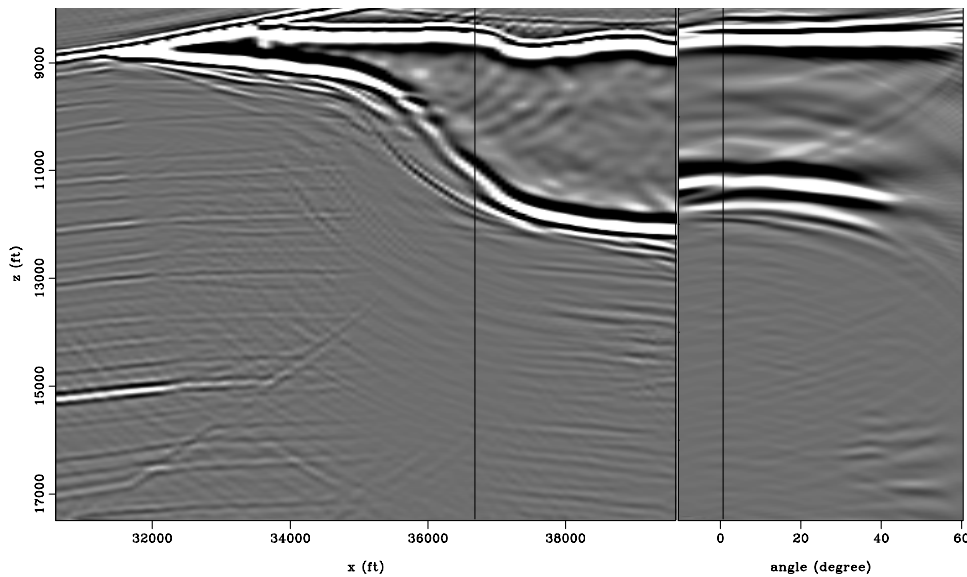


Figure B.7: Sigsbee shot-profile migration (reflection angle) using cross-correlation imaging condition. The front face corresponds to the image at 0° reflection angle, and the side face corresponds to the reflection-angle gather at $x = 36800$ ft.

AppendixB/. migang1-filt

Bibliography

- Alvarez, G., B. Biondi, and A. Guitton, 2007, Attenuation of specular and diffracted 2d multiples in image space: *Geophysics*, **72**, V97–V109.
- Berkhout, A. J., 1984, *Handbook of geophysical exploration: Seismic resolution*: Geophysical Press Limited.
- Biondi, B., S. Fomel, and N. Chemingui, 1998, Azimuth moveout for 3-d prestack imaging: *Geophysics*, **63**, 574–588.
- Biondi, B. L. and T. Tisserant, 2004, 3d angle-domain common-image gathers for migration velocity analysis: *Geophysical Prospecting*, **52**, 575–591.
- Chavent, G. and R. E. Plessix, 1999, An optimal true-amplitude least-squares prestack depth-migration operator: *Geophysics*, **64**, 508–515.
- Claerbout, J. F., 1985, *Imaging the Earth's Interior*: Stanford Exploration Project.
- , 1992, *Earth soundings analysis, processing versus inversion*: Blackwell Scientific Publications.
- , 2001, *Basic earth imaging*: Stanford Exploration Project.
- Clapp, M. L., 2005, *Imaging under salt: illumination compensation by regularized inversion*: PhD thesis, Stanford University.
- Clapp, R. G., B. L. Biondi, and J. F. Claerbout, 2004, Incorporating geologic information into reflection tomography: *Geophysics*, **69**, 533–546.
- de Bruin, C. G. M., C. P. A. Wapenaar, and A. J. Berkhout, 1990, Angle-dependent reflectivity by means of prestack migration: *Geophysics*, **55**, 1223–1234.
- Duquet, B. and K. J. Marfurt, 1999, Filtering coherent noise during prestack depth migration: *Geophysics*, **64**, 1054–1066.
- Fox, J., 1987, Seismic interpretation in salt-controlled basins: *The Leading Edge*, **6**,

11–11.

- Gelius, L.-J., I. Lecomte, and H. Tabti, 2002, Analysis of the resolution function in seismic prestack depth imaging: *Geophysical Prospecting*, **50**, 505–515.
- Gill, P. E., W. Murray, and M. H. Wright, 1981, *Practical optimization*: Academic Press Inc.
- Guitton, A., 2004, Amplitude and kinematic corrections of migrated images for nonunitary imaging operators: *Geophysics*, **69**, 1017–1024.
- Hanke, M., 1995, *Conjugate gradient type methods for ill-posed problems*: Longman Scientific & Technical.
- Howard, M. S. and N. Moldoveanu, 2006, Marine survey design for rich-azimuth seismic using surface streamers: 76rd Ann. Internat. Mtg., Expanded Abstracts, 2915–2919, Soc. of Expl. Geophys.
- Hu, J., G. T. Schuster, and P. Valasek, 2001, Poststack migration deconvolution: *Geophysics*, **66**, 939–952.
- Keggin, J., T. Manning, W. Rietveld, C. Page, E. Fromyr, and R. Borselen, 2006, Key aspects of multi-azimuth acquisition and processing: 76rd Ann. Internat. Mtg., Expanded Abstracts, 2886–2890, Soc. of Expl. Geophys.
- Kuhl, H. and M. D. Sacchi, 2003, Least-squares wave-equation migration for AVP/AVA inversion: *Geophysics*, **68**, 262–273.
- Leveille, J., K. Larner, and J. Higginbotham, 2005, A problem workshop: *The Leading Edge*, **24**, 1126–1132.
- Michell, S., E. Shoshitaishvili, D. Chergotis, J. Sharp, and J. Etgen, 2006, Wide azimuth streamer imaging of mad dog: Have we solved the subsalt imaging problem?: 76rd Ann. Internat. Mtg., Expanded Abstracts, 2905–2909, Soc. of Expl. Geophys.
- Mora, P., 1987, Nonlinear two-dimensional elastic inversion of multioffset seismic data: *Geophysics*, **52**, 1211–1228.
- Mulder, W. A. and R.-E. Plessix, 2004, How to choose a subset of frequencies in frequency-domain finite-difference migration: *Geophysical Journal International*, **158**, 801–812.
- Nemeth, T., C. Wu, and G. T. Schuster, 1999, Least-squares migration of incomplete reflection data: *Geophysics*, **64**, 208–221.

- Paffenholz, J., B. McLain, J. Zaske, and P. J. Keliher, 2002, Subsalt multiple attenuation and imaging: Observations from the sigsbee2b synthetic dataset: SEG Technical Program Expanded Abstracts, **21**, 2122–2125.
- Plessix, R.-E. and W. A. Mulder, 2004, Frequency-domain finite-difference amplitude-preserving migration: Geophysical Journal International, **157**, 975–987.
- Pratt, R. G. and M. H. Worthington, 1988, The application of diffraction tomography to cross-hole seismic data: Geophysics, **53**, 1284–1294.
- Press, W. H., S. A. Teukolsky, W. T. Vetterling, and B. P. Flannery, 1992, Numerical recipes in fortran 77: The art of scientific computing, second ed.: Cambridge University Press.
- Prucha, M. and B. Biondi, 2002, Subsalt event regularization with steering filters: 72th Ann. Internat. Meeting, Expanded Abstracts, 922–925, Soc. Expl. Geophysics.
- Prucha, M. L., B. L. Biondi, and W. W. Symes, 1999, Angle-domain common image gathers by wave-equation migration: SEG Technical Program Expanded Abstracts, **18**, 824–827.
- Richter, C. F., 1941, Elementary Seismology: Freeman.
- Rickett, J. E., 2003, Illumination-based normalization for wave-equation depth migration: Geophysics, **68**, 1371–1379.
- Rickett, J. E. and P. C. Sava, 2000, Offset and angle-domain common image-point gathers for shot-profile migration: Geophysics, **67**, 883–889.
- Ronen, S. and C. L. Liner, 2000, Least-squares DMO and migration: Geophysics, **65**, 1364–1371.
- Sava, P., 2006, Subsalt exploration and development: Imaging, interpretation, and drilling—what have we learned? 2006 seg/eage summer research workshop: The Leading Edge, **25**, 1370–1376.
- Sava, P., B. Biondi, and S. Fomel, 2001, Amplitude-preserved common image gathers by wave-equation migration: SEG Technical Program Expanded Abstracts, **20**, 296–299.
- Sava, P. and S. Fomel, 2003, Angle-domain common-image gathers by wavefield continuation methods: Geophysics, **68**, 1065–1074.
- Sava, P. and A. Guitton, 2005, Multiple attenuation in the image space: Geophysics,

70, V10–V20.

- Sayers, C. and D. Herron, 2007, Introduction to this special section: Subsalt exploration: The Leading Edge, **26**, 1404–1405.
- Shen, P., W. Symes, and C. C. Stolk, 2003, Differential semblance velocity analysis by wave-equation migration: 73st Annual International Meeting, SEG, Expanded Abstracts, Expanded Abstracts, 2132–2135.
- Shuey, R. T., 1985, A simplification of the Zoeppritz-equations: Geophysics, **50**, 609–614.
- Sirgue, L. and R. G. Pratt, 2004, Efficient waveform inversion and imaging: A strategy for selecting temporal frequencies: Geophysics, **69**, 231–248.
- Stolk, C. C. and W. W. Symes, 2002, Theory of differential semblance velocity analysis by wave equation migration: TRIP Annual Report.
- Tarantola, A., 1987, Inverse problem theory: Methods for data fitting and model parameter estimation: Elsevier Science Publication Company, Inc.
- Tikhonov, A. N. and V. Y. Arsenin, 1977, Solution of ill-posed problems: John Wiley and Sons.
- Winbow, G., T. Clee, and M. Rainwater, 2007, Multipath imaging into common-reflection-angle volumes at a gom site: The Leading Edge, **26**, 1430–1433.
- Yilmaz, O., 1987, Seismic data processing: Investigations in Geophysics No. 2.
- Zhang, Y., G. Zhang, and N. Bleistein, 2005, Theory of true-amplitude one-way wave equations and true-amplitude common-shot migration: Geophysics, **70**, E1–E10.